

TECHNISCHE UNIVERSITÄT MÜNCHEN

Lehrstuhl für Biochemie
der Technischen Universität München

Characterisation and optimisation of 20S proteasome inhibitors

Nerea Gallastegui de la Rosa

Vollständiger Abdruck der von der Fakultät für Chemie der Technischen
Universität München zur Erlangung des akademischen Grades eines

Doktors der Naturwissenschaften (Dr. rer. nat.)

genehmigten Dissertation.

Vorsitzender: Univ.-Prof. Dr. A. Itzen

Prüfer der Dissertation: 1. Univ.-Prof. Dr. M. Groll
2. Univ.-Prof. Dr. St. Sieber

Die Dissertation wurde am 25.04.2012 bei der Technischen Universität
München eingereicht und durch die Fakultät für Chemie am 12.07.2012 angenommen.

List of Publications

- N. Gallastegui**, and M. Groll, Analysing properties of proteasome inhibitors using kinetic and x-ray crystallographic studies. *Methods Mol Biol* 832 (2012) 373-90.
- N. Gallastegui**, P. Beck, M. Arciniega, R. Huber, S. Hillebrand, and M. Groll, Hydroxyureas as noncovalent proteasome inhibitors. *Angew Chem Int Ed Engl* 51 (2012) 247-9.
- M.A. Grawert, **N. Gallastegui**, M. Stein, B. Schmidt, P.M. Kloetzel, R. Huber, and M. Groll, Elucidation of the alpha-keto-aldehyde binding mechanism: a lead structure motif for proteasome inhibition. *Angew Chem Int Ed Engl* 50 (2011) 542-4.
- M. Groll, **N. Gallastegui**, X. Marechal, V. Le Ravalec, N. Basse, N. Richy, E. Genin, R. Huber, L. Moroder, J. Vidal, and M. Reboud-Ravaux, 20S proteasome inhibition: designing noncovalent linear peptide mimics of the natural product TMC-95A. *ChemMedChem* 5 (2010) 1701-5.
- N. Gallastegui**, and M. Groll, The 26S proteasome: assembly and function of a destructive machine. *Trends Biochem Sci* 35 (2010) 634-42.
- N. Gallastegui**, and M. Groll, How ATPases unravel a mystery. *Structure* 17 (2009) 1279-81.

Table of Contents

1	Summary.....	1
	Zusammenfassung.....	3
2	Introduction.....	5
2.1	The Ubiquitin-Proteasome Pathway	5
2.1.1	Pathway mechanism	5
2.1.2	The biological and physiological role of this pathway and its related diseases	7
2.2	The 26S and 20S proteasome.....	8
2.2.1	Structure of 26S proteasome: RP and CP	8
2.2.2	Function and mechanism of the 20S proteasome.....	10
2.3	The biological implication of the 20S Proteasome inhibition	12
2.3.1	Targeting the 20S proteasome	12
2.4	20S Proteasome inhibitors advantages and disadvantages.....	15
2.4.1	Peptide aldehydes.....	17
2.4.2	Boronates.....	18
2.4.3	Vinyl sulfones	19
2.4.4	Epoxyketones	20
2.4.5	β -Lactones.....	21
2.4.6	Non-covalent inhibitors-TMC95A and derivatives	23
3	Objectives	27
4	Materials and Methods	29
4.1	Materials and Chemicals	29
4.1.1	Chemicals	29
4.1.2	Materials	30
4.1.3	Buffers and solutions	31
4.1.4	Instruments.....	33
4.2	Methods	35
4.2.1	Native 20S Proteasome purification	35
4.2.2	<i>S.cerevisiae</i> cell lysis	35
4.2.3	Protein Purification	35
4.2.4	Polyacrylamide gel electrophoresis	37
4.2.5	20S Proteasome kinetic characterisation	38

4.2.6	Point measurement	39
4.2.7	IC ₅₀ measurements and K _i values.....	39
4.2.8	K _M values	40
4.2.9	Reversibility test.....	40
4.2.10	20S Proteasome crystallisation.....	40
4.2.11	Data collection	41
4.2.12	Data processing.....	41
4.2.13	Ligand building and Graphic representations.....	41
4.2.14	In-vivo HeLa cell experiments.....	42
4.2.15	5-Lipoxygenase inhibitor characterisation	44
5	Results and Discussion	45
5.1	Structural characterisation of decarboxylated peptides as 20S proteasome inhibitors	45
5.1.1	Initial characterisation and optimisation of side chains.....	45
5.1.2	Bivalent and Monovalent inhibitors	57
5.1.3	Cell accessibility assays	62
5.2	Identification and Modification of a novel 20S proteasome inhibitor: the hydroxyureas	65
5.2.1	Identification and optimisation of the Hydroxyureas as 20S proteasome inhibitors	65
5.2.2	Differences between Human and Yeast 20S proteasome inhibition	80
5.2.3	Cell accessibility assays	82
5.2.4	Hydroxyurea compounds and 5-lipoxygenase	84
5.2.5	Structural characterisation of site specific epoxyketone and vinyl sulfone based inhibitors for the 20S proteasome	86
5.2.6	CT-like active site specific epoxyketone based inhibitors	86
5.2.7	T-like active site specific vinyl sulfone based inhibitors	95
6	Conclusion	105
7	References.....	107
	List of Figures	i
	List of Tables	iii
	Abbreviations.....	v
	Acknowledgements.....	vii
	Declaration.....	xi

1 Summary

Proteasome inhibition has been used extensively both as marketed drugs against multiple myeloma and as valuable tool for cell biologist to fully dissect the proteasome role in protein degradation and antigen presentation. However, the toxic side effects of these compounds and their unspecific binding to the different subunits of the 20S proteasome limit their potential in disease treatment and their use as research tools. In this work we demonstrate that structural elucidation of inhibitors in complex with the 20S proteasome is a technique that is vital for drug design, specifically against such a large and complicated degradation machine as the 20S proteasome. The conclusions derived from crystallographic data are carefully complemented with *in-vitro* and *in-vivo* data in order to study and characterise different types of 20S proteasome inhibitors, ranging from novel binding mode inhibitors to complete subunit specific inhibitors.

Hereby, we report for the first time a set of linear-peptides, without any functional reactive head group, derived from the natural product TMC-95A. The 20S proteasome complex crystal structure demonstrated that the binding of these inhibitors was due to the side chains and the correct positioning of the peptide backbone and not due to a functional reactive group. The subsequent optimised compound '**2b**' presented herein, a highly Chymotrypsin-like specific inhibitor that has been shown to cross the cell membrane and alter the NF- κ B pathway. Other inhibitor strategies such as bivalent binding were undertaken in this work and appropriate inhibitors using an aliphatic carbon chain linker with intermediate peptide bonds, and **2b** inhibitor as a head group, were analysed. However, a decrease in activity was observed for the bivalent inhibitors and, the *in-vivo* results indicated no alteration of the NF- κ B pathway.

In this research has also identified a new class of proteasome inhibitor that is characterized by a novel mode of ligand binding and proteasome inhibition; the hydroxyureas. The hydroxyureas represent the smallest, reversible, non-covalently bound and Chymotrypsin-like active site specific inhibitors observed to date for the 20S proteasome that do not contain any functional reactive head group. Hereby, a lead compound was discovered through the

screening of a chemical library. The crystal structure of this lead compound proved to bind in a unique manner occupying pockets that so far have been unexplored, the S1 and S3 *sub*-pockets. Combining structural research, molecular modelling, chemical synthesis and kinetic experiments we could optimise from a poor high micromolar to an optimal nanomolar range inhibitor. This work proves the strength of the combination of these techniques. Furthermore, due to the unique properties of this set of inhibitors, the lead inhibitor **HU10** could be considered both as a drug like compound and a future fragment for drug design.

Additionally, irreversible peptide inhibitors, having an epoxyketone or vinyl sulfone functional reactive group, were also characterised. The interactions of peptide side chains and positioning of an ureido structural element in the Chymotrypsin- and Trypsin-like active site were described. The results obtained from this set of inhibitors can therefore be combined with modelling techniques leading to alternative more favourable moieties in this position. Therefore, in combination these results provide an overview of 20S proteasome inhibition and deliver new insights into this highly challenging and scientifically demanding research field.

Zusammenfassung

Die Inhibition des Proteasoms spielt in verschiedenen Bereichen eine große Rolle. Zum einen in Form von Medikamenten gegen multiples Myelom, zum anderen als wertvolles Werkzeug für Zellbiologen, um die Rolle des Proteasoms im Proteinabbau und der Antigenpräsentation zu analysieren. Schwere Nebenwirkungen dieser Substanzen und unspezifisches Binden an die verschiedenen Untereinheiten des 20S Proteasoms begrenzen jedoch das Potenzial in der Behandlung von Krankheiten und als Forschungswerkzeuge. In dieser Arbeit zeigen wir, dass die Strukturaufklärung von Inhibitoren in Komplex mit dem 20S Proteasom eine wichtige Technik im Medikamentendesign ist, vor allem gegen eine so große und komplexe Proteinabbau-Maschinerie wie das 20S Proteasom. Die Schlüsse, die aus kristallographischen Daten gezogen wurden, werden durch *in vitro* und *in vivo* Daten ergänzt, um verschiedene Arten von 20S Proteasom-Inhibitoren zu untersuchen und zu charakterisieren, beginnend bei Inhibitoren mit neuartigen Bindungsweisen, bis hin zu Inhibitoren, die vollständig spezifisch für eine Untereinheit sind.

Erstmals zeigen wir eine Gruppe linearer Peptide ohne funktionale Kopfgruppe, abgeleitet vom Naturstoff TMC-95A. Die Kristallstruktur des 20S-Proteasom-Komplexes zeigte, dass die Bindung dieser Inhibitoren aufgrund der Seitenketten und der korrekten Positionierung des Peptidrückgrats stattfand, und nicht durch eine reaktive Gruppe. Die daraufhin optimierte Substanz **2b**, weist eine hohe Spezifität für die chymotryptische Untereinheit auf und ist in der Lage die Zellmembran zu passieren und den NF- κ B-Signalweg zu beeinflussen. Andere Inhibitionsstrategien, wie bivalente Bindung, wurden in dieser Arbeit untersucht. Entsprechende Inhibitoren mit einer aliphatischen Kohlenstoffketten-Verknüpfung mit zwischengeschalteten Peptidbindungen und dem **2b** Inhibitor als Kopfgruppe wurden analysiert. Es wurde jedoch eine reduzierte Aktivität der bivalenten Inhibitoren beobachtet und die *in vivo* Experimente weisen auf keine Beeinflussung des NF- κ B-Signalwegs hin.

Während dieser Forschungsarbeit wurde eine neue Klasse von Proteasominhibitoren identifiziert, die durch eine neuartige Weise der Ligandenbindung und Proteasominhibition

charakterisiert ist: die Hydroxy-Harnstoffe. Hydroxy-Harnstoffe repräsentieren die kleinsten reversiblen, nicht-kovalent gebundenen und chymotryptischen-Untereinheit spezifischen Inhibitoren des 20S-Proteasoms, die bisher entdeckt wurden und keine reaktive Kopfgruppe tragen. Eine Leitstruktur wurde mittels Screening einer chemischen Bibliothek gefunden. Die Kristallstruktur dieser Leitsubstanz zeigte, dass diese in einer einzigartigen Weise bindet und Taschen besetzt, die bisher nicht genutzt wurden: die S1 und S3 Taschen. Durch Kombination von Strukturforschung, molekularer Modellierung, chemischer Synthese und kinetischen Experimenten konnten wir die Substanz von einem schlechten mikromolaren zu einem optimalen nanomolaren Inhibitor optimieren. Diese Arbeit zeigt die Stärke der Kombination dieser Techniken auf. Weiterhin kann der Leit-Inhibitor **HU10** durch die einzigartigen Eigenschaften dieser Inhibitorengruppe sowohl als Medikamenten-Kandidat, als auch als Fragment für die zukünftige Medikamentenentwicklung gesehen werden.

Zusätzlich wurden auch irreversible Peptid-Inhibitoren mit reaktiver Epoxiketon- oder Vinylsulfon-Gruppe charakterisiert. Die Interaktionen von Peptid-Seitenketten und die Positionierung eines Ureido Strukturelements im chymotryptischen und tryptischen aktiven Zentrum wurden beschrieben. Die Daten, die von dieser Inhibitorengruppe erhalten wurde, können mit Hilfe von Modellierung zu alternativen und günstigeren Resten in dieser Position führen. Die Summe dieser Ergebnisse bereitet einen Überblick über 20S Proteasominhibition und liefert neue Erkenntnisse in dieses herausfordernde und wissenschaftlich anspruchsvolle Forschungsfeld.

2 Introduction

2.1 The Ubiquitin-Proteasome Pathway

2.1.1 Pathway mechanism

The Ubiquitin Proteasome system (UPS) is the main non-lysosomal protein degradation pathway in the cell (Hershko & Ciechanover, 1998) and it is responsible for 90% of all proteins cleaved. Its pivotal role in protein degradation marks this pathway as highly important for protein homeostasis, and consequently the UPS has to be rigorously controlled during the distinct life-cycles in the cell. In the UPS all redundant or misfolded proteins are postrationally modified for degradation through the addition of a 76-residue protein which is highly conserved through all eukaryotes, the Ubiquitin (Ub).

Once the initial Ub is attached to the protein of interest, polyubiquitylation of the substrate occurs through the sequential transfer of additional Ub molecules, forming ubiquitin chains which are then recognised by the 26S proteasome, the main degradation machine in the UPS. Polyubiquitination of substrates occurs through a cascade of reactions involving a series of enzymes: i) activation of Ub-C-terminus, in an ATP dependent manner by the Ub-activator enzyme E1, ii) transfer of the activated Ub to the protein of interest by the Ub-conjugating enzymes E2 and iii) coupling to surface-exposed lysine residues of these protein by Ub-ligase enzymes E3. Transfer and coupling of the Ub is performed through the formation of an isopeptide bond with the carboxylic acid of the terminal glycine from the Ubiquitin's di-glycine and the surface-exposed lysine residue of the protein of interest motif, (**Fig. 1**) (Pickart, 2001).

Ubiquitin conjugation is a reversible process mediated by an additional set of proteases, the DUBs (deubiquitinating enzymes). These enzymes specifically cleave the isopeptide bond at the C-terminus of Ub and its conjugated protein when the protein of interest is erroneously ubiquitinated or once it has been degraded. However, once the substrate has been conjugated with a minimum of 4Ub, this ubiquitin chain is recognised by the 26S proteasome that

recognises, translocates and cleaves the protein of interest to a peptide length of 7-19 amino acids. These peptide chains are either additionally cleaved by peptidases or used by the cell in different cellular functions, such as that of antigen presentation (**Fig. 1**).

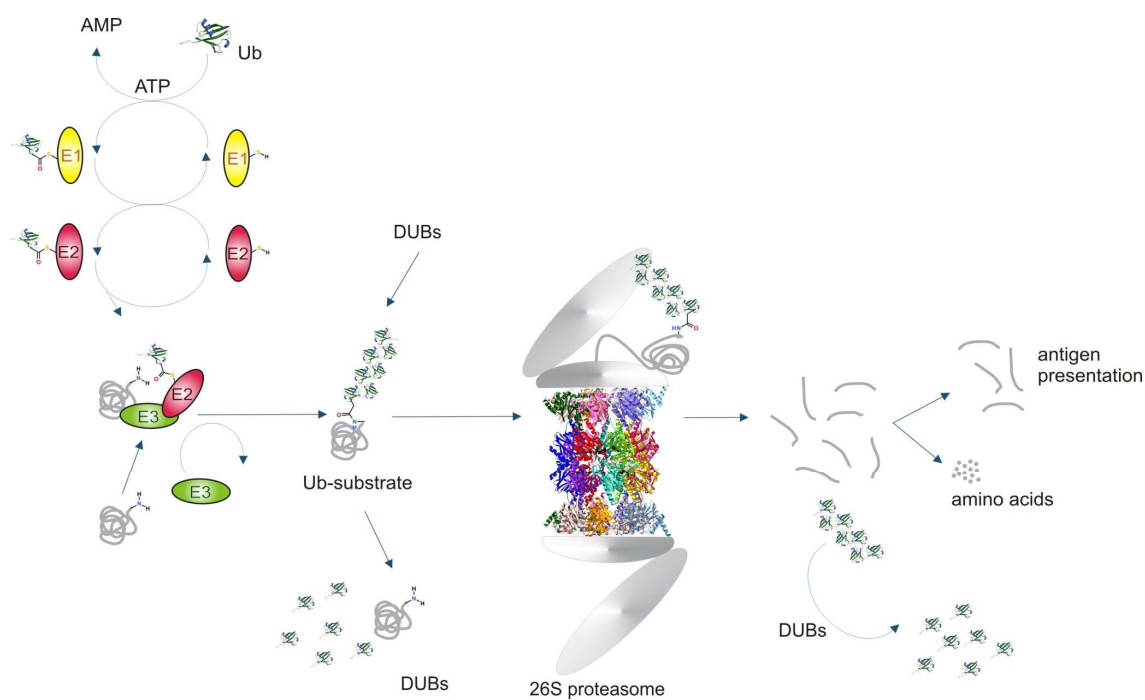


Fig. 1: The main degradation pathway in eukaryotic cells, the UPS

Degradation of proteins of interest are tagged by a polyubiquitin chain before presented to the 26S proteasome. In order to do so, the Ub are activated in an ATP dependant manner and attached to the protein of interest through a cascade of enzymes E1-E3. Once the polyubiquitin chain is attached, the proteins are recognised, unfolded and translocated in the 26S proteasome. These proteins are hereby cleaved in to peptides which can subsequently be used for different functions in the cell or cleaved by other proteases into amino acids. Additionally, the DUB enzymes ensure that this process is irreversible through the cleavage of unwanted polyubiquitin chains.

2.1.2 The biological and physiological role of this pathway and its related diseases

Since the discovery of the UPS in the 1990's, significant progress has been made in understanding the structure, function and important regulatory roles of ubiquitin network. This biological pathway has been demonstrated to play crucial roles in various cellular activities such as cell cycle regulation, DNA damage repair, signal transduction, membrane trafficking, neural development, and transcription. Due to the importance of this pathway, in all the biological functions previously described, the alterations of UPS in various human diseases have been of great interest to the scientific community. It is, thus far, well accepted that changes in the proteolytic function of the UPS lead to deregulation of cellular function and consequently disease development, such as cancer, kidney disease, cardiomyopathies, ageing, and nervous system diseases like that of Alzheimer's and Parkinson's disease. To date, there is only one U.S. Food and drug administration (FDA) approved drug inhibiting the proteasome core particle in the UPS, Velcade[®], a molecule developed by Millennium Pharmaceuticals, (Richardson & Mitsiades, 2005). This drug, used for the treatment of Multiple myeloma (MM), proved that the UPS is a medically targetable pathway and its importance, not only in MM, but also in other cancers. It soon became noticeable that cellular functions regulated by ubiquitin are often deregulated in human cancers (Burger & Seth, 2004) along with the reported genetic alterations, abnormal expression or dysfunction of various ubiquitin components. It is therefore not surprising that there is a huge interest in targeting various components involved in the ubiquitin pathway such as E3 ubiquitin ligases, E1 ubiquitin activator, DUBs and the 26S proteasome with the aim of producing drugs against many diseases, especially anti-cancer drugs.

Targeting the UPS, though, has proven not to be as easy a task as initially expected. With a large number of proteins involved that includes more than 500 E3, 50 E2 and 100 DUB enzymes, an E1 and the 26S proteasome there are approximately 650 possible drugable targets in this pathway. However, Ub ligases do not possess a small active site, as they mostly interact through protein-protein interactions, thus this makes targeting these enzymes with small molecules a big challenge. The understanding of E2 enzymes is still poor and additional studies are needed in both DUBs and E1 in order to establish potential future anti-cancer drugs.

Nevertheless, a recently developed E1 inhibitor, PYR 41 (4[4-(5-nitro-furan-2-ylmethylene)-3,5-dioxo-pyrazolidin-1-yl]-benzoic acid ethyl ester) (Yang et al., 2007) has proven to have high potential as a chemotherapeutic agent. Ligases such as Mdm2, an oncogenic E3 ligase, that are widely overexpressed in many tumours and usually complexes with p53 have created an open research field of great interest (Bond et al., 2004; Ostrowska, 2008). Furthermore, even though E2 enzymes have, so far, not been exploited as a drugable target, its involvement in cancer has become apparent. An example is that of E2-EPF ubiquitin-conjugating enzyme, which has been shown to be over expressed in the majority of breast cancers and to enhance the clinical effectiveness of anticancer Type II topoisomerases –directed drugs (Tedesco et al., 2007). Nonetheless, of all the plausible targets in the UPS, it became evident that the 26S proteasome is a promising enzyme to target (Mitsiades, Mitsiades, Hideshima, Richardson, & Anderson, 2005). Its rigid internal core structure and clearly defined active sites opened a new area of research which has been flourishing since the 1990's and has led to the worldwide prescribed drug, bortezomib, (marketed as Velcade[®]) which was valued, in the BCC Research Report List, at approximately \$1000 million in 2009.

2.2 The 26S and 20S proteasome

2.2.1 Structure of 26S proteasome: RP and CP

The 26S proteasome is a sophisticated multicatalytical complex which can be divided into two main structures: the 20S proteasome core particle (CP), where protein degradation occurs, and the 19S regulatory complex (RP), which recognizes and unfolds Ub-tagged substrates. The 19S regulatory particle is a multi-subunit complex that can be subdivided into two main structures: the base and the lid. The base complex is composed of six different AAA-type ATPase subunits (ATPases associated with a variety of cellular activities), known as RPT1-6, as well as three non-ATPase subunits known as RPN1-2 and RPN13 (Regulatory Particle Non-ATPase proteins). On the other hand, the lid complex consists only of nine subunits (RPN3, RPN5-9, RPN11-12 and RPN15). These two complexes are connected to each other by the linker subunit RPN10; however, the spatial organization of each 19S subunit, as well as their defined

roles in the 26S holocomplex, is currently not well understood. In contrast, due to its rigid architecture, the crystal structures of both, prokaryotic and the eukaryotic CP could be solved to atomic resolution (Bochtler, Ditzel, Groll, & Huber, 1997; Groll et al., 1997; Löwe et al., 1995). The structure of the CP showed that this multi-subunit complex can be compared to a non-specific shredder with a cylindrical barrel-shaped architecture composed of four stacked heptameric rings, each comprising α - and β -type subunits arranged in an $\alpha\beta\beta\alpha$ -stoichiometry. Simpler organisms such as archaeobacteria have CPs with 14 identical α -subunits and 14 identical β -subunits, whereas more complex organisms such as eukaryotes have seven different α - and β -subunits that form an $\alpha_{1-7}\beta_{1-7}\beta_{1-7}\alpha_{1-7}$ arrangement (**Fig. 2**) (Groll et al., 1997; Huber et al., 2012; Unno et al., 2002). Surprisingly structure comparison of α and β subunits revealed that all CP subunits adopt a similar fold even though they possess different primary sequences: a four-layer structure in which two sheets of antiparallel β strands are sandwiched between two layers of α helices.

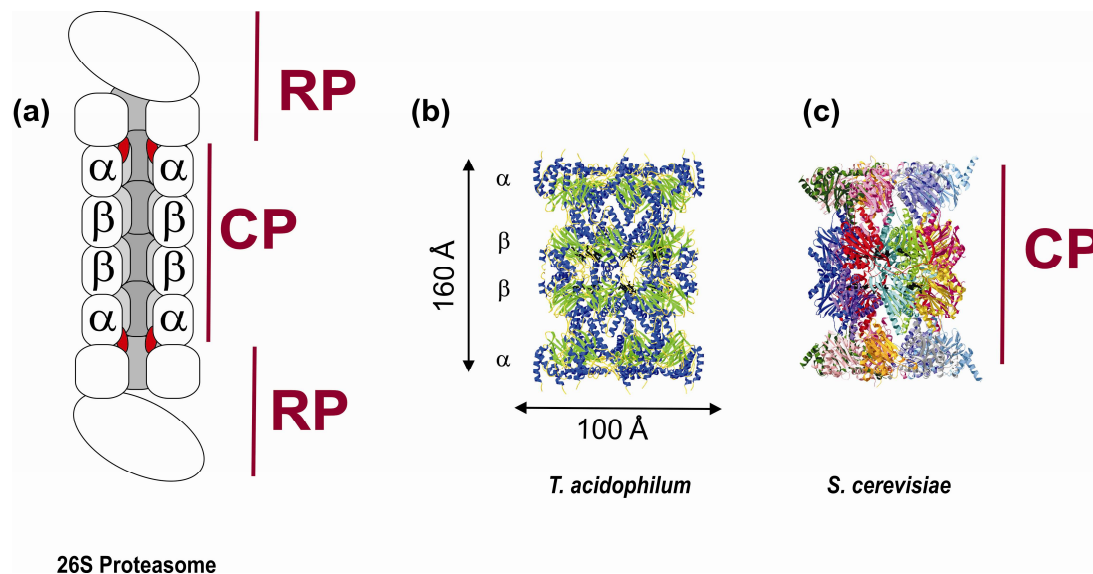


Fig. 2: Structure of proteasome

(a) Cartoon representing the core and regulatory structure of the 26S proteasome (b) Structure of 20S proteasome from *T. acidophilum* (Löwe et al., 1995) and (c) *S. cerevisiae* (Gallastegui & Groll, 2010; Groll et al., 1997).

Therefore, it can be suggested that the proteasomes has originated from an ancestral gene and through evolution got further fine-tuned and adjusted to meet the multifaceted demands of higher organisms as described below.

2.2.2 Function and mechanism of the 20S proteasome

Peptide bonds are hydrolysed by the N-terminal threonine residue, Thr1, which is embedded in the β subunits of the CP. The crystal structure of the yeast 20S proteasome and the characterisation of various mutants allowed the elucidation of the proteolytic mechanism: i) the Thr1O^y adds to the carbonyl group of the peptide bond in the substrate forming an acyl ester intermediate and ii) the Thr1N atom acts as a proton acceptor aiding in the cleavage of the intermediate. During catalysis a nucleophilic water molecule (NUK) is located in close proximity to Thr1 acting as a proton shuttle between ThrO^y and ThrN and involving itself in the cleavage of the acyl-ester intermediate (Groll et al., 1997; Groll et al., 1999). Next to the active site different specificity pockets, referred to as non-primed S1, S2, S3...Sn and primed S1', S2', S3'... Sn' sites, depending on their location to the hydrolysable peptide bond. However, it must be mentioned that compared to other proteases the CP lacks an S2 specificity pocket. Ligand side chains upon binding adapt to the proteasomal specificity pockets referred to as P1, P2, P3...Pn and P1', P2', P3'...Pn', accordingly (**Fig. 3**) (Groll et al., 1997).

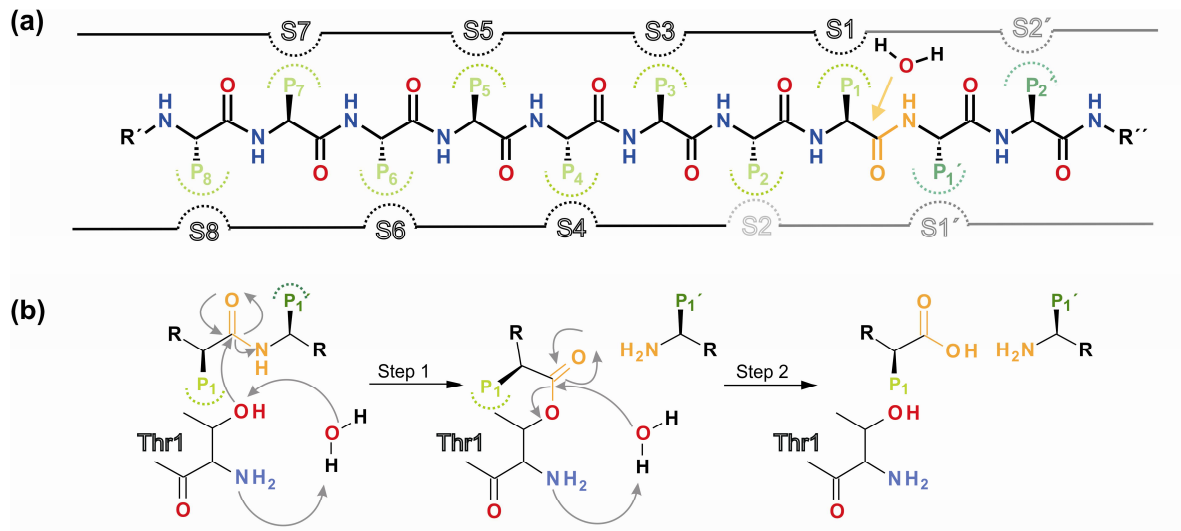


Fig. 3: Cleavage mechanism of the CP

(a) Schematic representation of non-primed substrate binding pockets S1, S2, S3...Sn (coloured black except for S2 (grey) due to its lack of presence in constitutive CPs) and primed S1', S2', S3'...Sn' sites, depending on their location to the peptide bond. Ligand side chains with the proteasomal specificity pockets, are referred to as P1, P2, P3...Pn and P1', P2', P3'...Pn', accordingly. **(b)** Cleavage mechanism by Thr1 in the active β subunits of the 20S proteasome (Groll et al., 2010).

Interestingly, whereas most prokaryotic organisms possess only one type of β -subunit (thus providing 14 equivalent catalytic sites per CP), eukaryotic CP only have three of the seven different β subunits which are proteolytically active. Therefore, the eukaryotic CP possess a more specific product cleavage pattern formed by the network between the inactive and the active β -type subunits which give shape to three unique substrate binding channels. Hydrolysis of chromophoric substrates defined these three distinct cleavage preferences as Caspase- (C), Trypsin- (T) and Chymotrypsin- (CT) like activities (whereby the active Thr1 is located in β 1, β 2 and β 5 respectively). Mutational and structural analysis revealed that the cleavage preference is determined primarily by the S1 pocket and that residue 45 plays also a crucial role (Huber et al., 2012). Hereby, this residue changes from an arg in β 1, gly in β 2 and a Met in β 5 giving rise to the more acidic, basic and hydrophobic nature of these three pockets respectively (Groll, Bochtler, Brandstetter, Clausen, & Huber, 2005). Furthermore, the constraints of residue 45 give rise to either more spacious or constricted S1 pockets that lead to either a more branched-

chain amino acid (BrAAP) or a small neutral amino acid (SNAAP) substrate preference. Surprisingly, unlike the P1 side chains of substrates and inhibitors which bind to the T- and C-like active site, binding to the CT-like activity can induce a uniform concerted structural rearrangement of the protein residues in order to adapt to the different substrate requirements. This high degree of proteasomal substrate binding channel plasticity is only found in $\beta 5$ and may result in unexpected results in designed drug function. Furthermore, higher up organisms such as mammals possess additional isoforms of the 20S proteasome which differ structurally in their active sites. These CPs are named immuno-, constitutive and thymo- proteasomes and carry out specific functions in the cell. This subject is beyond the scope of this work and can be found in the following articles (Huber et al., 2012; Murata et al., 2007; Unno et al., 2002).

2.3 The biological implication of the 20S Proteasome inhibition

2.3.1 Targeting the 20S proteasome

The crystal structure of the 20S proteasome from *T. acidophilum* complexed with the aldehyde acetyl-Leu-Leu-norleucinal (calpain inhibitor I), in combination with mutation studies revealed that the N-terminal Thr of the β -subunits serve as proteolytic active centres (Löwe et al., 1995; Seemüller et al., 1995). This same inhibitor also revealed the different specificity pockets in the eukaryotic proteasome (Escherich et al., 1997). Proteasome inhibitors have been used extensively both as tools to investigate regulation of the ubiquitin-proteasomal system and as template structures for design of fine-tuned proteasome inhibitors with perspectives for possible drug development (Vinitsky, Cardozo, Sepp-Lorenzino, Michaud, & Orłowski, 1994; Vinitsky, Michaud, Powers, & Orłowski, 1992). These inhibitors have aided in the discovery of many of the biochemical effects of proteasome blockage in different types of cancers. Although these effects are not yet fully understood, they do show desired cellular responses, such as the increase in apoptosis and decrease in proliferation of different cancer cell lines. The *in-vivo* experiments and clinical trials of the boronic acid inhibitor, bortezomib, initially demonstrated

that proteasome inhibition triggers these cellular responses through the alteration of the NF- κ B pathway. This transcription factor, which is over expressed in several tumours, also regulates the expression of genes involved in cell apoptosis and proliferation. Although it is normally dormant and bound in the cytosol to I κ B α , when I κ B α is phosphorylated, it can be consequently recognised by the UPS. I κ B α is subsequently ubiquitinated and degraded by the 26S proteasome, liberating NF- κ B and allowing it to translocate into the nucleus. Whereby, NF- κ B up-regulates cell proliferation and angiogenesis, as well as additionally protecting the cell from apoptosis. It was subsequently demonstrated that several proteins involved in apoptosis and cellular proliferation are significantly affected in proteasome inhibition, such as cyclin-dependent kinase inhibitors (p21 and p27), the tumour suppressor p53 and proapoptotic proteins (Bid and Bax). Additionally, c-Jun-NH₂ terminal kinase which promote cell death in response to stress are also affected being up regulated in proteasome inhibition, hereby promoting apoptosis (**Fig. 4**) (Boccardo, Morgan, & Cavenagh, 2005).

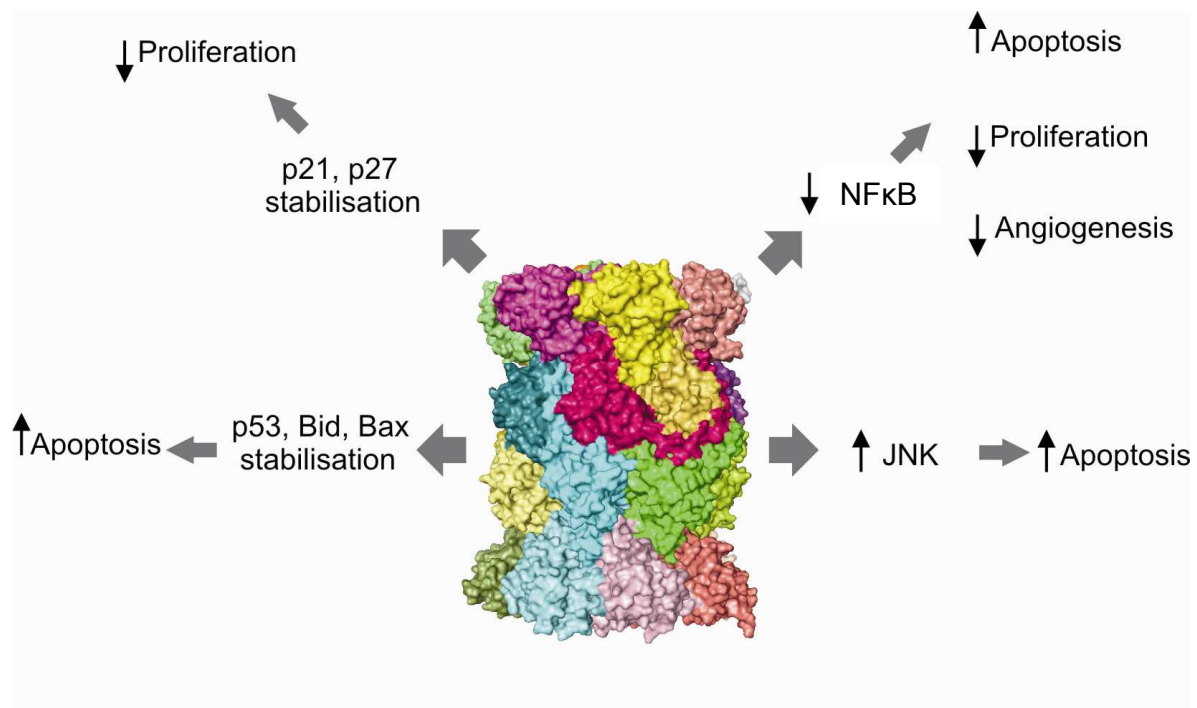
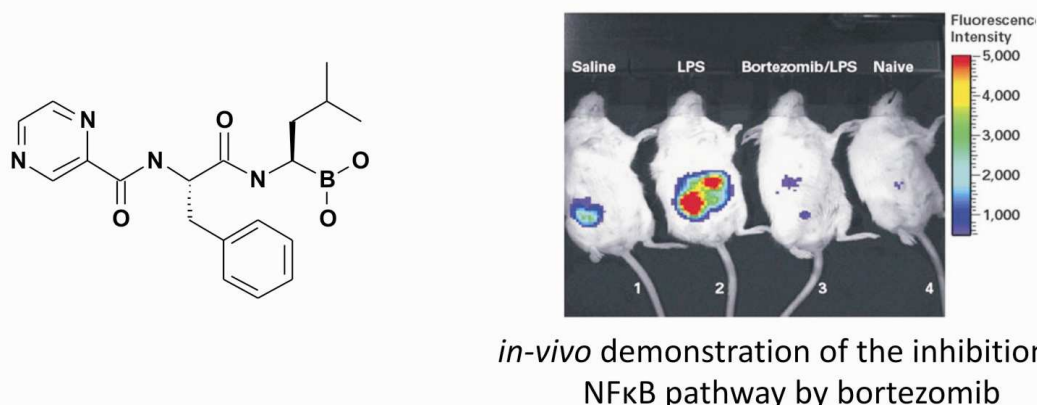


Fig. 4: CP inhibition

Effect of 20S proteasome inhibition by boronic acid inhibitors in different cellular pathways resulting in apoptosis, angiogenesis, and proliferation of cancer cells.

Proteasome inhibitors such as boronic acid peptides block this pathway, however, the specific NF- κ B inhibitor, PS-1145 only partially alters proliferation of tumour cells thus indicating that other pathways are additionally affected by proteasomal inhibition (**Fig. 4**) (Nemeth et al., 2004; Richardson & Mitsiades, 2005).

Since the first proteasome inhibitors were discovered many different varieties of natural and synthetic chemical compounds have been identified with most of them possessing different proteasomal proteolytic activities and binding modes to Thr1. However, from this pool of inhibitors only bortezomib has been approved for marketing. Bortezomib has demonstrated *in-vivo* activity in both cell lines and in patient tumour cells representing haematological malignancies (Wiberg et al., 2009). Additionally, preclinical cancer murine models showed a promising anti-tumour activity *in-vivo* and further xenograft model of multiple myeloma showed a significant inhibition of tumour growth and an increase in overall survival as well as a decrease in tumour angiogenesis (**Fig. 5**) (Boccardo et al., 2005).



in-vivo demonstration of the inhibition of NF κ B pathway by bortezomib

Fig. 5: Bortezomib

Chemical structure of Bortezomib (Velcade[®]) and a xenograft biophotonic image revealing the suppression of NF κ B pathway activity after bortezomib treatment. Mice 1, 2, and 3 on the left were implanted with the 293 NF κ B luciferase reporter cell xenografts. Mouse 1 received an intraperitoneal (IP) injection of saline. Mouse 2 received an IP injection of lipopolysaccharide (LPS) to activate the NF κ B pathway. In mouse 3, 1.0 mg/kg of bortezomib was injected intravenously before the IP LPS injection (Xenogen, Alameda, CA performed the image taken from medscape.com).

These promising results led to an initial approval of bortezomib for patients with relapsed and refractory myeloma, whereby 28 % of the patients achieved a complete, near complete or partial response and 35 % had some response, an initial result which subsequently led to phase clinical trial I, II and III and eventually to its FDA approval (Orlowski, 2004). Nevertheless, despite the clinical success of this inhibitor, toxic effects such as painful neuropathy have been noted and resistance to this drug remains a clinically significant problem (Ruschak, Slassi, Kay, & Schimmer, 2011). These side effects have highlighted the need of not only secondary generation CP inhibitors but also for the discovery of inhibitors with new structures and mechanism of action (Chen, Frezza, Schmitt, Kanwar, & Dou, 2011).

2.4 20S Proteasome inhibitors advantages and disadvantages

Since the structure and the biological significance of the 20S proteasome was elucidated there are numerous different inhibitors described in the literature, many of which have been optimised and analysed using X-ray crystallography. Hereby, we will briefly describe a few important compounds with different modes of binding and effectivity against the CP, factors which, as their name suggest, have given rise to the nomenclature used in their classification (Borissenko & Groll, 2007) (**Fig. 6**).

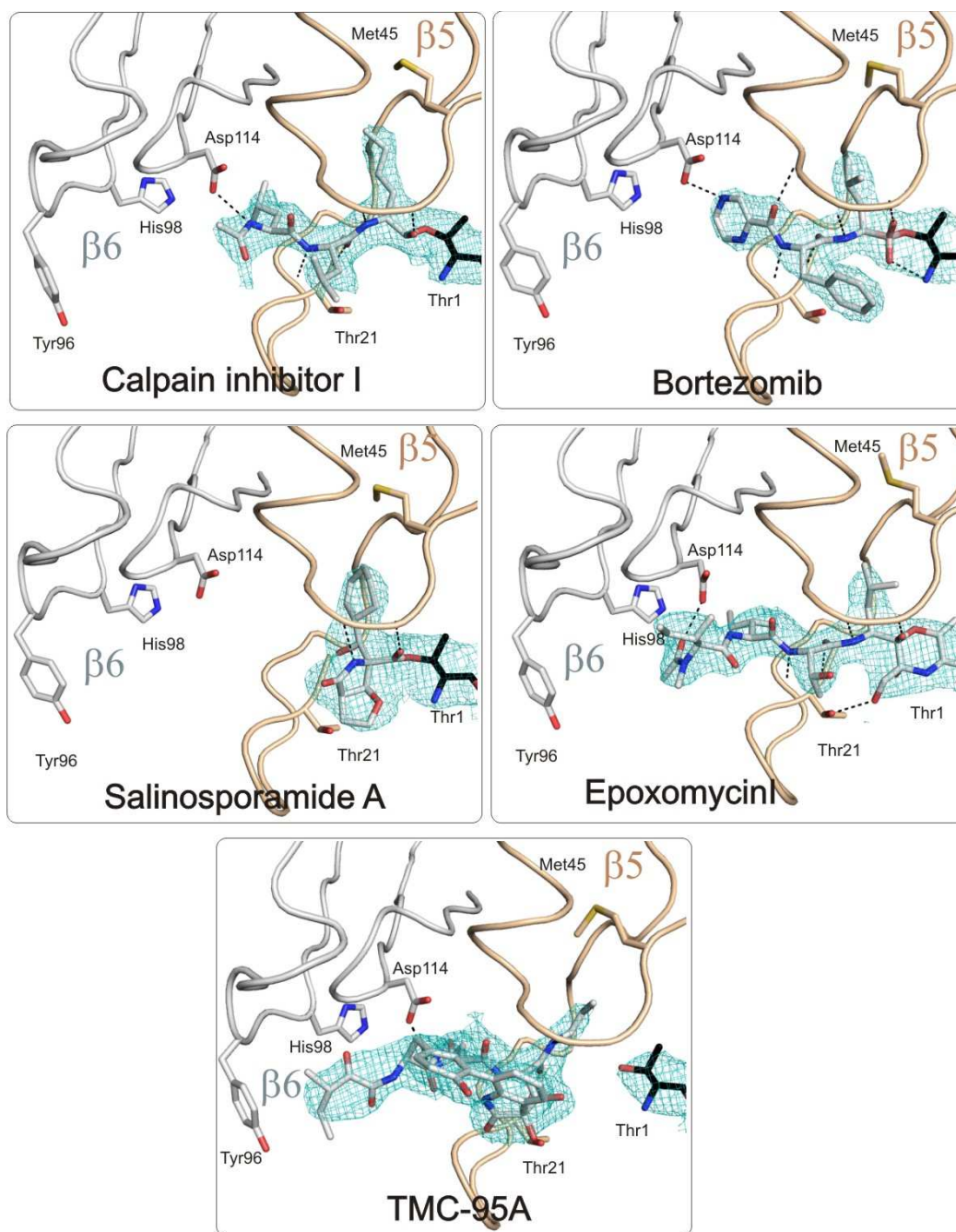


Fig. 6: Crystal structures of 5 different inhibitors in complex with the CT-like active site

Complexed crystal structure of the different types of inhibitors to the CP. The CT- active site is formed by both $\beta 5$ and $\beta 6$ subunit hereby shown in cartoon form and depicted in light brown and grey colour respectively. The different inhibitors are shown in stick form and coloured in grey with their original electron density map. Important side chains in this active site such as Met45, Asp114, His98, Tyr96, Thr21 and Thr1 are additionally shown in stick form. Hydrogen bonding is represented by dotted black lines.

The following inhibitors will be described in detail: 1) peptide aldehyde, which were the first CP inhibitors to be discovered 2) peptide boronates which have, as previously mentioned, already entered the market 3) peptide vinyl sulfones and Epoxyketones, which turned out to be valuable tools in cell biology 4) β -lactones, which follow a minimalised chemical structure and high inhibitory profile and 5) TMC-95A and its derivatives, which represent the first reversible and non-covalent CP inhibitor (**Fig. 6**).

2.4.1 Peptide aldehydes

Calpain inhibitor I and II (CAL I) were the first synthetic inhibitors which demonstrated 20S proteasome inhibition. These peptide aldehydes were originally used in the inhibition of calpains, a type of cysteine proteases which are involved in intracellular Ca^{2+} signalling pathways (Vinitsky et al., 1994). The complex structure of these inhibitors with the *T. acidophilum* and the *S. cerevisia* proteasome aided in the elucidation of the proteasomal inhibition mechanism with the discovery of the Thr active amino acid and the different subunit specificity pockets. It also proved that the aldehyde group reacts with the Thr1 forming a hemiacetal bond upon binding while the peptide adopts the secondary structure of an antiparallel β -sheet due to hydrogen bonds formed with the backbone amino acids of the different active sites (Groll et al., 1997). As shown in **Fig. 6**, CAL I has a norleucine and a leucine side chain protruding into the S1 and the S3 pockets respectively. Kinetic studies with fluorogenic 7-amino-4-methylcoumarin (AMC)-peptides revealed a much higher affinity for the CT-like active site, even though this inhibitor is bound to all active sites of the 20S proteasome in the crystal structure, an artefact caused by the high concentrations used for the inhibitor during in crystal soaking.

Generally, aldehyde inhibitors enter the cell rapidly but due to their highly reactive head group they lack proteasome specificity as they react with serine and cysteine proteases. However, over time many peptide aldehydes have been synthesised, analysed and improved. Surprisingly the simple tripeptide Z-leu-leu-leu-aldehyde, also known by the name MG132 turned out to be more specific for the CP (Tsubuki, Saito, Tomioka, Ito, & Kawashima, 1996).

MG132, when bound to the Thr1 has a leu side chain protruding into the S1 pocket which is much more appropriate for the CT-like active site. These minor changes led to a much more specific proteasome aldehyde which requires a 10-fold higher concentration for calpain's inhibition. Due to these characteristics and its early discovery, MG132 is currently the primary choice for *in-vivo* experiments that require proteasome inhibition.

2.4.2 Boronates

Peptide boronates differ significantly from their aldehyde analogues: they dissociate more slowly from the proteasome, they are more stable and they inhibit cysteine proteases to a much poorer extent due to the weak interaction between sulphur and boron atoms. The peptide boronic acids also possess an increase in potency over their aldehyde counterparts, as it can be observed by the MG132 boronate analogue, Z-leu-leu-leu-boronate (MG262), that exhibits a K_i value of 4 nM. These type of inhibitors quickly became of interest (from the clinical point of view) due to, not only these characteristics but also its low molecular weight, ease of synthesis, and its water-solubility (Adams et al., 1998).

The most notorious boronic acid, bortezomib, is a dipeptide boronic acid with a Pyz-Phe-Leuboro structure (**Fig. 5**). This inhibitor was shown to preferentially target the CT-like active site, however it also inhibits T- and C-like active sites to a much lesser extent (Adams et al., 1999). The crystal structure of this inhibitor complex with the 20S proteasome showed a clear defined electron density in all active sites (Groll, Berkers, Ploegh, & Ovaa, 2006) and the binding mode was shown to be quite similar in all three active sites. Whereby, the peptide residues adopt, as previously described, an antiparallel β -sheet conformation and the boron atom covalently interacts with the ThrO^V. This boronic acid core ensures higher specificity for the CP compared to cysteine proteases, as boron atoms have a higher affinity towards hard oxygen nucleophiles in contrast to soft sulphur nucleophiles (**Fig. 6**). Furthermore, the tetrahedral boronate adduct, formed upon binding, is further stabilized by a second acidic boronate hydroxyl moiety, which hydrogen-bridges the N-terminal threonine amine atom and adds to the CP selectivity (Groll, Berkers et al., 2006). However, it is actually the inhibitor side chains, P1 and

P3, interactions with the active site that gives rise to its active site specificity (**Fig. 6**) (Groll, Berkers *et al.*, 2006). It was clearly observed that, in the CT-like active site, the leucine side chain in bortezomib engages in a multitude of hydrophobic interactions with the S1-pocket which highly stabilise this inhibitor. However, for this to occur, the Met45 undergoes a structural rearrangement, similar to that upon CALI binding, that enlarges the S1-pocket of the CT-like active site and adequately accommodates this P1 side chain. The structural data of bortezomib in complex with the T- and C-like active sites of this CP provides an explanation to the lower affinity observed towards these active sites. In T-like active site the unstructured S1 pocket allows space for the motion and flexibility of P1 leucine side chain, permitting no hydrophobic interactions to be formed. The S1 pocket of C-like active site is dominated by Arg45 making this site highly polar and consequently inadequate for the leu in the P1 site. Furthermore the P3 pyrazyl ring cannot be comfortably placed in either of these two sites, as they do not form positive interactions with the inhibitor and differ greatly from that of CT-like active site.

The high specificity of bortezomib against the CP and its pharmacokinetic characteristics has made this inhibitor the first proteasome inhibitor to reach the market. However, as mentioned previously, there are a series of draw backs to this inhibitor that make the discovery of inhibitors with new structures and mechanism of action pertinent.

2.4.3 Vinyl sulfones

Peptide vinyl sulfones, are described as CP inhibitors which (Bogyo *et al.*, 1997), contain a vinyl sulfone moiety as their war head. These compounds bind irreversibly to the Thr10^Y through a 1,4 -michael addition reaction between the double bond of the vinyl sulfone moiety and the active site residue. Although this inhibitors are less reactive than aldehydes and do not inhibit serine proteases they show high specificity for cysteine proteases (Palmer, Rasnick, Klaus, & Bromme, 1995). Selectivity of these inhibitors however depends on the peptide portion (Groll & Huber, 2004; Nazif & Bogyo, 2001). Furthermore, due to their easy synthesis

these classes of substances inhibitors have become a great asset for sensitive active site probes for mechanistic studies of proteasomes in different tissues and cells (Verdoes et al., 2006; Verdoes et al., 2010).

2.4.4 Epoxyketones

The first epoxyketone inhibitors for the 20S proteasome discovered were the natural inhibitors eponomycin from *Streptomyces hygroscopicus* and epoxomycin from an actinomycete strain. (Hanada et al., 1992; Oikawa et al., 1991; Sugawara et al., 1990). Enzymatic assays with epoxomycin revealed that this inhibitors primary affects the CT-like active site, however, inhibition of the T- and C-like active site does occur at about 100 and 1000 fold higher concentration (Borissenko & Groll, 2007; Groll, Kim, Kairies, Huber, & Crews, 2000; Kim, Myung, Sin, & Crews, 1999). The crystal structure of this natural product in complex with the yeast 20S proteasome revealed a new and unexpected mode of binding. Whilst the peptide backbone adopts the habitual antiparallel beta sheet with the proteins backbone, the epoxyketone head group forms a unique and previously unobserved six-membered morpholino ring system with the Thr10^Y and ThrN (**Fig. 6**) (Groll, Nazif, Huber, & Bogyo, 2002). This irreversible binding further confirmed by mass spectrometric analysis, is formed in a two-step process. The nucleophilic attack of the Thr10^Y forms a hemiacetal bond with the carbonyl carbon of the epoxyketone which then forms a morpholino adduct through an intramolecular secondary amine cyclisation upon epoxide ring opening. This N-morpholino adduct provides unique specificity of this inhibitors towards the CP as other proteases do not possess an amino-terminal nucleophile residue.

This inhibitor binding profile makes this class of compounds one of the most selective inhibitors thus far. Furthermore, recently a close analogue of epoxomycin, carfizomib, went into phase II clinical trials after showing that it specifically targets the CT-like active site leading to accumulation of ubiquitin protein conjugates and proteasome substrates (Kuhn et al., 2007). Additionally, it proved inhibition of myeloma cell proliferation through induction of programmed cell death and most importantly it showed increased efficacy compared to

bortezomib and was active against bortezomib-resistant MM cell lines and samples from patients with clinical bortezomib resistance (Khan & Stewart, 2011; Kuhn et al., 2007). The refined specificity and relative ease of synthesis of this type of inhibitors have made this headgroup a popular choice for synthetic inhibitors which have aided in the development of site specific inhibitors and activity-based probes as well as a promising future marketable drug (Kisselev, van der Linden, & Overkleeft, 2012; Verdoes et al., 2010).

2.4.5 β -Lactones

Another set of proteasome inhibitors are those possessing a β -lactone functional group. These inhibitors react with the ThrO^y in a covalent manner forming an acyl ester bond (Groll, Balskus, & Jacobsen, 2008; Groll et al., 1997). Omuralide was the first β -lactone proteasome inhibitor reported in literature. This *Streptomyces sp.* metabolite was shown *in-vivo* to bind mainly to the proteasomal subunit β 5 in a reversible manner consequently inhibiting the CT-like active site. (Dick et al., 1996). The crystal structure of omuralide proved its specificity only to the CT-like active site and showed clearly the covalently bound β -lactone inhibitor. The binding of this inhibitor occurs through the acylation of the free hydroxy group of the N-terminal Thr10^y to the carbonyl group in the β -lactone moiety subsequently opening the lactone ring. The complex structure additionally showed the NUK water, which normally hydrolysis the acyl ester intermediate and releases the peptide product, was completely distorted preventing the release of the inhibitor (Groll et al., 1997; Groll, Huber, & Potts, 2006). Hereby, it is the hydroxyl group generated after the cleavage of the β -lactone that occupies this position preventing inhibitor release. Following binding to the Thr1, omuralide accommodates itself in order to form a large number of hydrogen bonds and stabilising hydrophobic interactions with the S1 pocket that additionally stabilise this inhibitor further and explain its subunit specificity.

After a decade, two additional natural products from *Streptomyces sp.* proved to exhibit antitumour activity, the Belactosin A and C (Armstrong & Scutt, 2004; Asai, Hasegawa, Ochiai, Yamashita, & Mizukami, 2000). These specific β 5 natural products, containing a β -lactone reactive group, were derivatised into two stronger proteasome inhibitors, the homobelactosin

A and C (**Fig. 7**). The crystal structure of homobelactosin C in complex with the 20S proteasome revealed an identical binding to ThrO^y, as for that of omuralide, as well as gave an explanation for its subunit selectivity. The positioning of the 3-aminocarbonyl side chain showed to accommodate perfectly to the S1-pocket in β 5, however it proved to be too sterically demanding for either β 1 or β 2 (Groll, Larionov, Huber, & de Meijere, 2006). The binding mode of homobelactosine C provided evidence for the first time structural insight into the proteasome's primed site. This information opened a window into unexplored pockets of β 5 active site and serves as a useful template in the design on proteasome inhibitors.

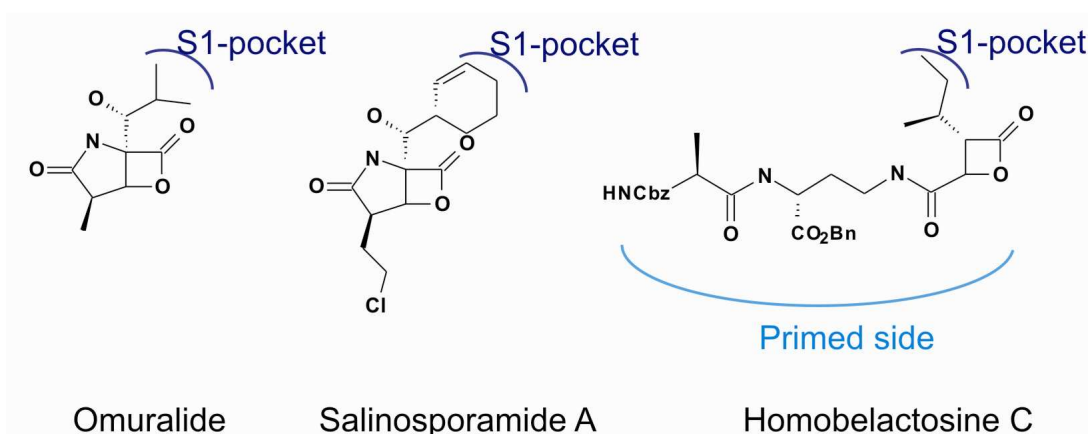


Fig. 7: Chemical structure of β -lactones

Chemical structure of omuralide, salinosporamide A and homobelactosine C. Side chains which protrude into the S1 pocket are highlighted in dark blue. Shown in light blue is part of the ligand structure that protrudes into the primed side.

The natural product salinosporamide A, was discovered during the fermentation of *Salinispora tropica*, a actinomycete found in marine sediments in the Bahamas (**Fig. 6**). Surprisingly this inhibitor possesses a similar chemical structure to omuralide with two unique characteristics, a cyclohexene ring in place of the isopropyl group and a chloroethyl group instead of the methyl group. These changes significantly enhanced its potency *in-vitro* and *in-vivo* and also altered the inhibitor's substrate specificity as Salinosporamide A binds to all active sites in the CP. Structural data of this inhibitor complexed with the CP showed that the binding

mode of this ligand to the ThrO^Y is identical to that of the omuralide. However, the chloroethyl side chain of Salinosporamide A forms a cyclic tetrahydrofuran with the C3-O group, upon lactone ring opening (Groll, Huber et al., 2006). Salinosporamide A has been proven to act against multiple myeloma cells that are resistant to other anti-proteasome cancer drugs such as bortezomib, as well as, showing a high efficacy in animal models of not only multiple myeloma, but also, colon, pancreatic and lung cancers (Chauhan, Hideshima, & Anderson, 2006). These advantages lead to the initiation of clinical trials for Salinosporamide A in 2006 by Nereus pharmaceutical, clinical trials that are still in process evaluating this inhibitor as a single drug and in combination with other therapeutic agents.

2.4.6 Non-covalent inhibitors-TMC95A and derivatives

All previously described inhibitors possess a reactive head group that covalently binds to the active residue ThrO^Y. However, this characteristic can be related to high reactivity and therefore cytotoxicity, as well as, give rise to undesired side effects. TMC-95A and its diastereomers B, C and D were the first non-covalent proteasome inhibitors known before this thesis was initiated. Inhibition tests of TMC-95A against a series of enzymes including m-calpain, cathepsin L, Trypsin and the 20S proteasome resulted in only selective inhibition of the CP in the low nanomolar range, showing an IC₅₀ of 200, 60 and 5.4 nM in the C, T and CT-like activity respectively (Koguchi et al., 2000; Kohno et al., 2000). Furthermore, these inhibitors which consist of modified amino acid residues forming a heterocyclic ring system are not related to any other proteasome inhibitor previously described (**Fig. 7**). The crystal structure of the 20S proteasome complexed to TMC-95A showed the inhibitor bound to all active sites in a non-covalent manner and proved the none existent of the interaction between ThrO^Y and TMC95-A (**Fig. 6**) (Groll, Koguchi, Huber, & Kohno, 2001). As most proteasome inhibitors with a peptide backbone, including the aldehydes, epoxyketones, borontates and vinyl sulfones described above, TMC95A adopts an antiparallel β -sheet structure with the peptide backbone (**Fig. 6**). Interestingly, the potency of this inhibitor is caused by a plenitude of hydrogen bonds formed with the 20S proteasome, as well as, its rigid ring structure which prevents major

structural rearrangements of the ligand and the protein upon binding. Thus, TMC-95A is favoured over flexible ligands due to entropic reasons. Its different subunit inhibition profiles can be explained through the characteristics of the P1 and the P3 side chains formed by the (Z)-prop-1-enyl and the asparagines respectively. These side chains aid the tight binding and positioning of the inhibitor and produce specific interactions that explain the high affinity of TMC-95A to the CT-like active site. The total synthesis of TMC-95A inhibitor is, however, highly complex, but its structure has led to a new lead structure segment that has been used to design a set of endocyclic, fully synthetic, subunit specific non-covalent inhibitors, the Biphenyl-Ether-Based compounds (BIA) (Groll, Gotz, Kaiser, Weyher, & Moroder, 2006). These new set of proteasome inhibitors confirmed the importance of the ring strain characteristics as well as the side chain interactions with residues forming the distinct specificity pockets.

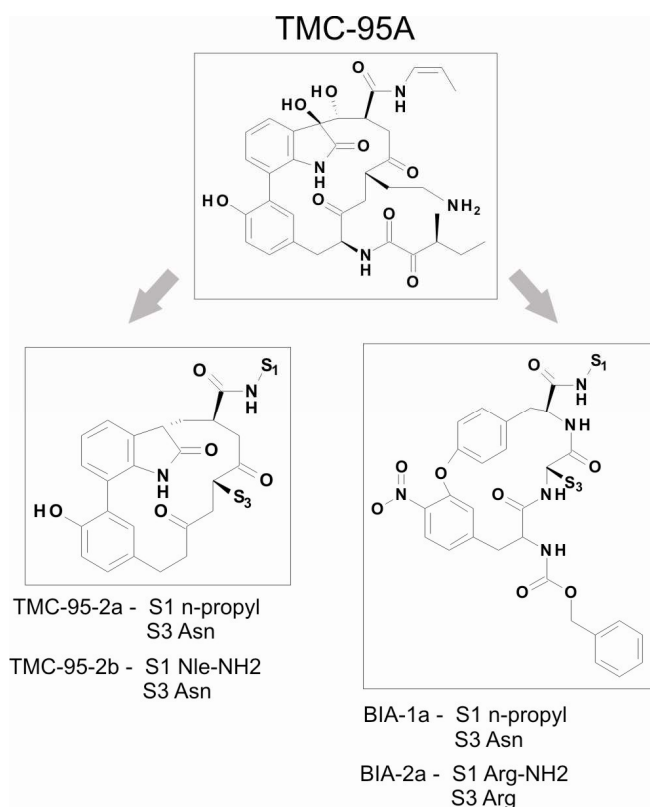


Fig. 8: Natural product TMC-95A

Chemical structure of TMC-95A and both derivatives: TMC-95-2a/b and BIA-1a/2a, the oxindole phenyl and biphenyl-ether based inhibitors.

Previous attempts to produce a synthetically more feasible structure involved the maintenance of the endocyclic oxindole phenyl clamp of the TMC-95A structure, however, even though a similar hydrogen bonding network was observed in these inhibitors a strong decrease in activity *in-vitro* was reported. In this TMC-95A derivatives, the P1 residue was replaced either by a a) n-propyl chain (**Fig. 8** TMC-95-2a) which is less favourable for S1 binding and b) a norleucine side chain (**Fig. 8** TMC-95-2b). As predicted the nLeu side chain in P1 caused a displacement of the Met45 of $\beta 5$ subunit, however unexpectedly the inhibitor backbone was shown to be shifted from its optimal binding position. This is in direct contrast to all previous findings; for example, CAL 1 binding causes a structural rearrangement of Met45 only due to the correct positioning of the peptide backbone. (Groll, Gotz *et al.*, 2006). Furthermore, in the case of the substitution of the oxindole phenyl clamp with a biphenyl-ether group, which has a chemically simpler structure, these inhibitors were shown to be more specific to the T-like active site.

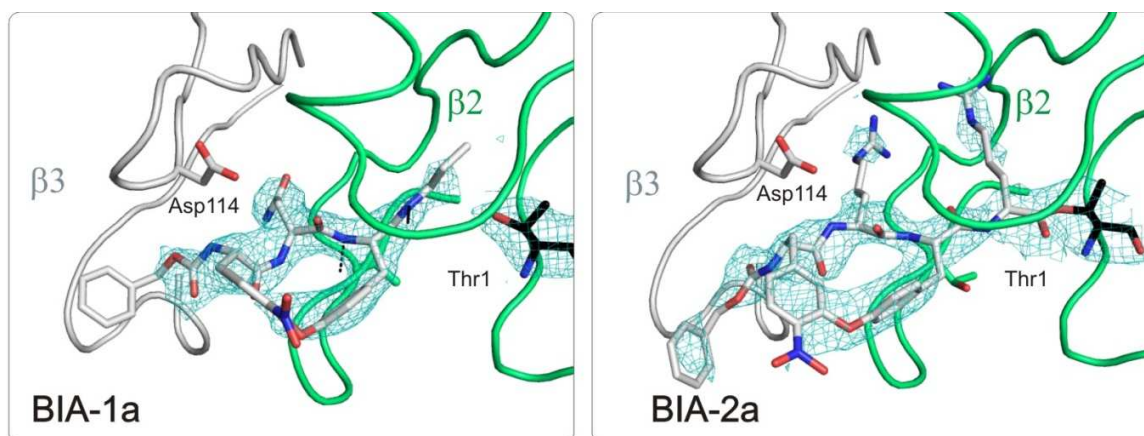


Fig. 9: 20S proteasome structure complexed to the biphenyl-ether based inhibitors BIA 1a and 2a

Complexed crystal structure of BIA-1a and BIA-2a to the CP was shown to complex uniquely to the T-like active site. The T-like active site is formed by both $\beta 2$ and $\beta 3$ subunit hereby shown in cartoon form and depicted in green and grey colour respectively. The different inhibitors are shown in stick form and coloured in grey with their original electron density map. Important side chains in this active site such as Asp114 and Thr1 are additionally shown in stick form. Hydrogen bonding is represented by dotted black lines.

However, the endocyclic biphenyl-ether clamp showed a decrease in potency compared to TMC-95A due to the lack of the oxo group in the P2 site which forms important hydrogen bonds for inhibitor stability. Modifications slightly improved protein binding but showed, in the crystal structure, the formation of a covalent ester bond between the inhibitor and the active residue in $\beta 2$ (**Fig. 9**) (Groll, Gotz et al., 2006)

As has been introduced in this section, proteasome inhibitors are not only used as actual marketed drugs (like in the case of bortezomib) but have also served and serve as a valuable tool for cell biologist who are still struggling to fully dissect the proteasome role in protein degradation and antigen presentation (Kisselev et al., 2012). Even though a number of selective proteasome inhibitors exist, the toxic side effects of these compounds strongly limit their medical applications (Borissenko & Groll, 2007). The need of new binding mode inhibitors with a highly specific subunit preference is therefore essential in order to expand the therapeutic potential of the 20S proteasome and our understanding into many biological pathways.

3 Objectives

The aim of this thesis was to characterise and optimise different types of reversible and irreversible proteasome inhibitors. In order to do so, different techniques were established at the Department of Biochemistry at the Technische Universität München, such as *in-vitro* enzymatic and *in-vivo* proteasome assays. Furthermore, complex structure elucidation of the 20S proteasome with different inhibitors was a major topic of these research projects. Hereby, X-ray crystallography was used to provide valuable information on their binding mode and their mechanistic properties. This technique proved to be invaluable in this work; led to a detailed understanding of the binding mechanism of these compounds and aided in their optimisation process. During the course of this thesis a series of reversible and irreversible inhibitors were characterised, leading to the identification of: i) a complete novel mode of action, ii) new types of CP inhibitors and iii) highly subunit specific proteasome inhibitors. Therefore, this thesis offers new insights into 20S proteasome inhibition and describes an overview into this challenging research topic. In particular, the results obtained in this work have additionally demonstrated the importance of the combination of crystallographic, *in-vitro* and *in-vivo* techniques in drug development, a fact that has been exploited throughout the different research projects hereby presented.

4 Materials and Methods

4.1 Materials and Chemicals

4.1.1 Chemicals

Chemicals	Source
1-Propanol	Merck, Germany
2-Mercaptoethanol, pure	Merck, Germany
2-methyl-2,4- pentanediol (MPD)	Merck, Germany
5-Bromo-4-chloro-3-indoylphosphate (BCIP)	Roth, Germany
Acetic acid (100 %, p.a.)	Roth, Germany
Acrylamide/ Bis-acrylamide (40%, 29:1)	Roth,, Germany
Bromophenol Blue S	Serva, Germany
Coomassie Brilliant Blue R-250	Serva, Germany
Ethanol (96 %)	Merck, Germany
Ethylenediaminetetraacetic acid (EDTA)	Merck, Germany
Hydrochloric acid	Merck, Germany
Isopropyl alcohol	Merck, Germany
Methanol	Merck, Germany
Protein marker	Applichem, Germany
Sodium chloride	Merck, Germany
Sodium dodecyl sulfate (SDS)	Roth, Germany
Sodium hydroxide	Merck, Germany
Sodium hydroxide	Merck, Germany
Tetramethylethylenediamine (TEMED)	Roth, Germany
Tris(hydroxymethyl)-aminomethane (Tris)	Merck, Germany
dichlorodihydrofluorescein diacetate (H2DCF)	Cayman, USA
botting grade powdered milk	Roth, Germany
Tween 20	Invitrogen, Germany

Substrates, enzymes and antibodies	
DNA-ase I	Invitrogen, Germany
Lipoxygenase	Cayman, USA
Suc-LLVY-AMC	Bachem, Germany
Z-LLR-AMC	Bachem, Germany
Z-LLE-AMC	Bachem, Germany
I κ B α	Invitrogen, Germany
GAPDH	Sigma-Aldrich, Germany
rabbit anti-mouse antibody	Invitrogen, Germany

4.1.2 Materials

4.1.2.1 Cell Culture Materials

Cell culture material	Source
Dulbecco's Modified Eagle Medium	Sigma-Aldrich, Germany
Fetal bovine Serum (FBS)	Invitrogen, Germany
X10 trypsin/EDTA	Invitrogen, Germany
X10 Phosphate buffer Saline	Invitrogen, Germany
protein extraction reagent (M-PER)	Thermofisher scientific, Germany
Interleukin-1	Invitrogen, Germany

4.1.2.2 Miscellaneous Material

Material	Source
Amicon® Ultra-15 Centrifugal Filter	Millipore, Germany
Whatman Filter Paper	GE Healthcare, Germany
polyvinylidene fluoride (PVDF)	Roth, Germany

4.1.2.3 Chromatographic and Spectrophotometric material

Material	Source
Phenyl Sepharose	GE healthcare, Germany
Hydroxyapetite	Biorad, Germany
Resource Q	GE healthcare, Germany
Superdex 200 HR 26/60	GE healthcare, Germany
Transparent 96 well plate	NUNC, Thermo scientific, Germany
White 96 well plate	NUNC, Thermo scientific, Germany

4.1.2.4 Western Blot material

Material	Source
ECL plus western blotting detection	GE healthcare, Germany
BioMax® Light Films	Kodak, Germany

4.1.3 Buffers and solutions

4.1.3.1 Bradford Reagent

0.1 g of Serva Blue G was dissolved in 10 ml of ethanol and 25 ml of H_3PO_4 and stirred thoroughly for 10 min. The volume of the mixture was adjusted to 250 ml with distilled water, and the solution was filtered and stored in a dark colored bottle at room temperature.

4.1.3.2 BSA solution

10 mg of bovine serum albumine (BSA) was dissolved in distilled water. The volume of the solution was adjusted to 10 ml with distilled water. This solution was used as a standard for protein determinations and stored at 4 °C.

4.1.3.3 Potassium phosphate buffer

For a 50 mM Potassium phosphate (KP) pH 7.5, prepare two solutions: a) 50 mM dipotassium-hydrogen-phosphate (K_2HPO_4) by dissolving 8.7 g in 1 L ultrapure water and b) 50 mM potassium-dihydrogen-phosphate (KH_2PO_4) by dissolving 6.8 g in 1 L ultrapure water. Both solutions were mixed until a pH of 7.5 is obtained.

4.1.3.4 SDS-Polyacrylamide gel electrophoresis (SDS-PAGE) and Western blot buffers

Coomassie blue staining	2.5 g Coomassie-Blue R-250 454 ml Methanol 92 ml Acetic acid
Destaining solution	250 ml Methanol 100 ml Acetic acid 650 ml H ₂ O
Stacking gel buffer	0.25 M Tris/HCl, pH 6.8 0.2 % (w/v) SDS
SDS-PAGE running buffer	192 mM Glycine 25 mM Tris/HCl, pH 8.3 0.1 % (w/v) SDS
SDS-PAGE sample buffer	60 mM Tris/HCl, pH 6.8 5 % (w/v) SDS 3% 2-Mercaptoethanol 30 % (v/v) Glycerol 0.02 % (w/v) Bromphenol Blue 10 % (w/v) Sucrose
Separating gel buffer	1.5 M Tris/HCl, pH 8.8 0.4 % (w/v) SDS
Transfer buffer	200 mL Methanol 800 mL SDS-PAGE running buffer
TBS	50mM Tris/HCl pH 7.2 8.7g NaCl
PBS	8 g NaCl 0. 2g KCl 1.44g Na ₂ HPO ₄ 0.24g of KH ₂ PO ₄ H ₂ O upto 1 L

4.1.4 Instruments

Centrifuge and Balances	
Analytical balance TE 124S	Sartorius, Germany
Precision balance BP 3100P	Sartorius, Germany
SIGMA 3-30K (rotors 12150-H and 12154-H)	SIGMA laboratory centrifuges
SIGMA 4K15 (rotor 11150 and 13350)	SIGMA laboratory centrifuges
SIGMA 6-16K (rotor 12500)	SIGMA laboratory centrifuges
SIGMA 8K (rotor 11805 and 13850)	SIGMA laboratory centrifuges
SIGMA1-14 (rotor 12094)	SIGMA laboratory centrifuges, Germany

Chromatography Platforms	
ÄKTaprime™ plus	GE Healthcare, Germany
ÄKTapurifier™	GE Healthcare

Crystallography	
CrystalCap HTTM for CryoLoop™	Hampton, United States of America
CrystalCap HTTM Vial	Hampton, United States of America
CrystalWand Magnetic™	Hampton, United States of America
Foam Dewars	Spearlab, United States of America
Magnetic caps, vials and pins	Molecular Dimensions, United Kindom
Micro Tool Box	Molecular Dimensions, United Kindom
Mounted CryoLoop™ H	Hampton, United States of America
Siliconized Glass Cover Slides	Hampton, United States of America
SuperClear Pregreased 24 Well Plate	Crystalgen, United States of America
Taylor-Wharton CX100/HC20 cryo tank	tec-lab, Germany
Vial Tongs/Clamp	Molecular Dimensions, United Kindom
Zoom stereo microscope	
SZX10/KL1500LCD	Olympus , Japan

Electrophoresis and Blotting	
Chamber and tray	Appligene, Germany
Electrophoresis Power Supply EPS 600	Pharmacia Biotech, Sweden
Fast Blot B44	Biometra, Germany
G:box for gel imaging	Syngene, United Kingdom
Mini PROTEAN® Tetra Cell	BioRad, United States of America
Optimax Typ TR developing mashine	MS laborgeräte, Germany

Spectrophotometers	
Cary Eclipse Fluorescence	Varian, Germany
Cary 50 UV-vis spectrophotometer	Varian, Germany
NanoPhotometer™ Pearl	Implen, Germany

Additional Equipment	
TS Series Bench top cell disruption system	Constant systems ltd., United Kingdom
inoLab® pH 720 pH-meter	WTW, Germany
Laboklav 25/195 SHP	Steriltechnik, Germany
MR Hei-Standard magnetic stirrer	Heidolph, Germany
SenTix® 81 pH-electrode	WTW, Germany
Techne Dri-Block DB 2A	Bibby Scientific, United Kingdom
Thermomixer comfort	Eppendorf, Germany
Vacuum pump	vacuubrand, Germany

Computer software	
Adobe Acrobat 9 Pro	Adobe, United States of America
Adobe Photoshop CS4	Adobe, United States of America
CCP4 Software Suite	www.ccp4.ac.uk
Chem draw	Cambridgesoft, United states of America
CNS	Yale university, United states of America
COOT	http://www.biop.ox.ac.uk/coot/
Core/DRAW Graphics Suite X3	Coreldraw corporation, Germany
EndNote	Thomson reuters, Germany
MAIN	http://bio.ijs.si/sbl
Microsoft Office 2007	Microsoft, United States of America
MolScript/Bobscript	www.avatar.se/molscript
PyMOL	www.pymol.org
Tripos® Sybyl	Tripos A certara™ company, United states of America
UNICORNTM control software	GE Healthcare, Germany
XDS Program Package	MPI, Germany
XPLO2D	Uppsala Software Factory, Sweden

4.2 Methods

4.2.1 *Native 20S Proteasome purification*

An extended explanation of most of these methods can be found in the following paper: *Analysing properties of proteasome inhibitors using kinetic and x-ray crystallographic studies.* (Gallastegui & Groll, 2012)

4.2.2 *S.cerevisiae cell lysis*

120 g of commercially available yeast blocks was dissolved in 150 ml of 50 mM Potassium phosphate buffer at pH 7.5. DNA-ase I was added and stirred for 5 min. The yeast cells were then lysed in a French press (2400 PSI). Cell debris was removed by centrifugation at 6x140 g for 30min. The supernatant was transferred to a 500 ml beaker and 30 % saturated ammonium sulphate was added, the lysate mixture was subsequently filtered to remove fatty acid and lipid contaminations.

4.2.3 *Protein Purification*

Native proteasome purification was performed by using four distinct columns; column 1-4 respectively.

4.2.3.1 *Column 1 (Phenyl Sepharose):*

The cell lysis was applied to a hand packed phenyl-sepharose column (column volume, 100 ml ϕ 4 cm, depth 10-15 cm) which had been equilibrated with 20 mM potassium phosphate buffer (KP), pH 7.5 containing 1 M Ammonium Sulphate (AS) (flow rate, 5 ml min⁻¹). Protein elution was performed using a linear gradient of 1 M - 0 M AS in four column volumes, whereby 20S yeast proteasome was eluted at approximately 0.8-0.5 M AS. Fractions collected are tested for proteasome-activity through a fluorogenic assay. Hereby, 30 μ l of each fraction is pipetted into a well of a 96 well plates. 1 μ L of 10 mM Y-substrate was added to each well and

incubated for 1 h at room temperature. Fluorescence (Ex 360 nm – Em 460 nm) was measured. The selected fractions are then pooled and applied to the following column.

4.2.3.2 Column 2 (Hydroxyapatite):

Fractions tested and collected in column 1 were applied to a hand packed hydroxyapatite column (column volume 6 ml volume, ϕ 3 cm, depth 2-3 cm) which had been equilibrated with 20 mM KP, pH 7.5. (flow rate, 4 ml min⁻¹). Protein elution was performed using a linear gradient of 20 mM - 500 mM KP in 20 column volumes, whereby 20S yeast proteasome was eluted at approximately 130 mM KP. Fractions collected were tested as described for column 1 and selected fractions were then pooled and applied to the following column. Sodium-dodecyl-sulfate polyacrylamide gel electrophoretic (SDS-page) analysis was performed with proteolytically active fractions for protein analysis as described in section 4.2.4: Polyacrylamide gel electrophoresis.

4.2.3.3 Column 3 (Resource Q):

Fractions tested and collected in column 2 were applied to a Resource Q column (column volume 6 ml volume, ϕ 1.6 cm, depth 3 cm) which had been equilibrated with 20 mM tris(hydroxymethyl)aminomethane (Tris-HCl), pH 7.5 (flow rate, 2 ml min⁻¹). Protein elution was performed using a linear gradient of 0 mM - 500 mM NaCl in 10 column volumes, whereby 20S yeast CP is eluted at approximately 500 mM NaCl. Fractions collected were tested as described for column 1 and 2 and selected fractions were then pooled and applied to the following column. SDS-page analysis was performed with proteolytically active fractions for protein analysis.

4.2.3.4 Column 4 (HiPrep™ 26/10 Desalting column):

Fractions tested and collected in column 3 were applied to a HiPrep™ 26/10 Desalting column (column volume 50 ml volume, ϕ 2.6 cm, depth 10 cm) which had been equilibrated with 20 mM tris(hydroxymethyl)aminomethane (Tris-HCl), pH 7.5 (flow rate, 2 ml min⁻¹). Fractions collected were tested as described for column 1-3 and selected fractions were then pooled, SDS-page analysis was performed with proteolytically active fractions for protein analysis.

4.2.4 Polyacrylamide gel electrophoresis

The purity of protein fractions was measured by discontinuous sodium dodecyl sulfate polyacrylamide gel electrophoresis (SDS-PAGE) according to the system of Lämmli (1970). The gel was prepared using the SDS-PAGE discontinuous buffer system with vertical slab gels (Table 1 and Table 2). The components of the separating gel solution were mixed together and then loaded onto the slab deposited between two glass plates on the gel caster. The top of the gel was overlaid with isopropanol. The polymerization of acrylamide was completed after 1 h. After removing the isopropanol, the stacking gel solution was prepared and loaded on top of the separating gel in the presence of 10 wells comb. The stacking gel completed its polymerization after 20 min. The slab gel was placed on a multiple gel chamber which was connected to a electrophoresis system. Protein samples were mixed with SDS-sample buffer and mixtures were heated at 95 °C for 5 min. Then the protein samples were loaded into the wells and a protein marker was used as molecular weight protein standards. The electrophoresis system was driven by a power supply with 25 mA per gel. After running for 45 min, the gel was carefully removed and stained in staining solution for 30 min, destained for 30 min.

Stock solution	Stacking gel	Separating gel (15 % Acrylamide)
Acrylamide/ bisacrylamide mix	0.5 ml	3.75 ml
Stacking gel buffer	2.5 ml	-
Separating gel buffer	-	2.5 ml
Water	2.0 ml	3.75 ml
10% (w/v) APS	50 μ l	50 μ l
TEMED	5 μ l	5 μ l

Table 1 Mixture for 12% SDS –PAGE electrophoresis

Stock solution	Stacking gel	Separating gel (12 % Acrylamide)
Acrylamide/ bisacrylamide mix	0.5 ml	3.0 ml
Stacking gel buffer	2.5 ml	-
Separating gel buffer	-	2.5 ml
Water	2.0 ml	4.5 ml
10% (w/v) APS	50 μ l	50 μ l
TEMED	5 μ l	5 μ l

Table 2 Mixture for 15% SDS –PAGE electrophoresis

4.2.5 20S Proteasome kinetic characterisation

The kinetic parameters of the three characteristic activities; CT-, T- and C-like activities, are known to depend significantly on the assay conditions and enzyme preparation (Dahlmann, Kopp, Kuehn, Reinauer, & Schwenen, 1986). These methods described show optimised conditions which were performed in the presence of chromophoric compounds.

4.2.6 Point measurement

End point measurements of all three activity assays were performed to acquire an initial tendency of inhibitor-binding. Different concentrations of yeast CP were utilised for each active site. The following concentrations were used: 0.01 mg/ml for CT- and C- and 0.075 mg/ml for T-like active sites. T-like activity rapidly decreases upon proteasome storage and therefore was measured only with fresh proteasome. The inhibition of enzyme activity was determined by monitoring the decrease in hydrolysis of the fluorogenic substrate Suc-LLVY-AMC for CT-, Z-LLR-AMC for T- and Z-LLE-AMC for C-like activity under the following buffer conditions: 20 mM Tris, pH 7.5, 0.01 % (w/v) SDS. Inhibitors at a final concentration of 200 μ M were incubated with yeast CP for 15 min prior to substrate addition with a final concentration of 250 μ M. Reaction was incubated at room temperature for 1h and fluorescence measured at $\lambda_{exc} = 360$, $\lambda_{em} = 460$ nm. The percentage of rest activity was calculated using a 0 mM Inhibitor reaction as 100 % initial activity. All inhibitors hereby analysed were dissolved in DMSO and stored at -20° C. Due to the decrease in activity of the CP with increase concentration of DMSO, same volume of DMSO was used in all fractions.

4.2.7 IC_{50} measurements and K_i values

For the half maximal inhibitory concentration (IC_{50}) measurements and K_i calculations the method from section 4.2.6 was performed with a series of different inhibitor concentrations. The different percentage of the remaining activities was then plotted against the log concentration of the respective inhibitor. The values were obtained by analysing the percentage of inhibition against the compound concentration and the experimental data were fitted according to the equation: % inhibition = $100 [I]_0 / (IC_{50} + [I]_0)$. K_i values were calculated for competitive agonists and antagonists using the Cheng-Prusoff equation.

4.2.8 K_M values

The 20S proteasome K_M values were determined with a time resolved fluorescence measurement $\lambda_{exc} = 360$, $\lambda_{em} = 460$ nm. Here, a minimum of 10 different substrate concentrations were recorded in a time resolved measurement and the velocity of the reaction was calculated through the initial 0-1 min time slope (V_0). Recorded data were presented in a linear fashion yielding a Lineweaver-Burk plot to obtain V_{max} and K_M .

4.2.9 Reversibility test

Reversibility tests were performed by 15 min preincubation of the 20S proteasome with 200 μ M concentration of the inhibitor of interest followed by addition of Suc-LLVY-AMC substrate at 250 μ M concentration. The time resolved fluorescence was monitored over time at $\lambda_{exc} = 360$, $\lambda_{em} = 460$ nm.

4.2.10 20S Proteasome crystallisation

CP was buffered in 20 mM Tris-HCl, pH 7.5. Hereby, the proteasome fractions received from HiPrep™ 26/10 desalting column were concentrated using an Amicon® Ultra-15 Centrifugal Filter Units, 100 KDa cut off : at 5000 rpm to a concentration of approximately 40 mg/mL. Yeast CP crystals were grown in hanging drops at 24°C according to the following protocol described in (Gallastegui & Groll, 2012). Drops contained 3 μ l of protein and 2 μ l of the reservoir solution, 30 mM of magnesium acetate, 100 mM of morpholino-ethane-sulphonic acid (MES) (pH 6.8) and 10 % of 2-methyl-2,4- pentanediol (MPD). Crystals appeared within one week and achieve a final size of about 100 x 100 x 500 μ m³. 5 μ l of reservoir was pipette on top of the desired crystal and 0.5 μ l of inhibitor (20 mM – 100 mM initial concentration) was added and allowed to incubate at 20 °C for a minimum of 24 h. Crystals were soaked in a cryoprotecting buffer (30 % MPD, 20 mM of magnesium acetate, 100 mM of MES pH 6.8) and frozen in a stream of liquid nitrogen gas at 90 K (Oxford Cryo Systems) and subsequently mounted for data collection.

4.2.11 Data collection

Proteasome crystals with a typical size of about 100 x 100 x 500 μm^3 were used for data collection. As a rule CP crystals display high anisotropy, whereby the resolution limit of measurable reflections is beyond 2.0 Å in the b^* direction but only about 2.8 Å perpendicular to b^* . Due to the dimensions of the unit cell (300 Å in the b -axis primitive lattice) synchrotron radiation was utilized in order to obtain adequate datasets at high resolution. Datasets were collected with $\lambda=1.0$ Å at the X06SA-beamline in Swiss Light Source (SLS)/Villingen/Switzerland or at the European Synchrotron Radiation Facility (ESRF)/Grenoble/France. Images of a 180° rotation were collected per data set with an Oscillation range of 0.5 °.

4.2.12 Data processing

X-ray intensities and data reduction were evaluated by using the XDS program package (Kabsch, 1993). The anisotropy of diffraction was corrected by an overall anisotropic temperature factor by comparing observed and calculated structure amplitudes using the program CNS (A. Brünger, 1992; AT. Brünger et al., 1998). Electron density was improved by averaging and back transforming the reflections 10 times over the two fold non-crystallographic symmetry axis using the program package MAIN (Turk, 1992). Conventional crystallographic rigid body, positional and temperature factor refinements were carried out with CNS using coordinates of the yeast CP structure as a starting model, PDB 1RYP (Groll et al., 1997) .

4.2.13 Ligand building and Graphic representations

Topology and parameter-files for the ligand were received by Powell-minimization of their respective pdb-files using the program sybyl (Homer, Swanson, Jilek, Hurst, & Clark, 2008) and SKETCHER in CCP4 pack (Ihlenfeldt, Bolton, & Bryant, 2009). Model building of the ligand into the experimental electron density was performed using COOT (Emsley, Lohkamp, Scott, & Cowtan, 2010). Subsequent Translation/Libration/Screw (TLS) vibrational motion refinement was performed using the program REFMAC5 in CCP4 pack or CNS (A. Brünger, 1992; AT.

Brünger et al., 1998; Vagin et al., 2004). Ramachandran plot analysis was executed using SFCHECK in CCP4 pack (Vaguine, Richelle, & Wodak, 1999). Final graphic representations of molecules were completed using the programs MOLSCRIPT (Kraulis & 1991), BOBSCRIPT (Esnouf, 1997) and PyMOL (DeLano, 2002).

4.2.14 In-vivo HeLa cell experiments

4.2.14.1 Cell culture

The HeLa cell lines were obtained from the group of Prof S. A. Sieber's group, Department of Organic Chemistry II, TU München, Garching, Germany. Cells were frozen for storage and cultured at 37 °C under 5 % CO₂ in glucose Dulbecco's Modified Eagle's Medium (DMEM) supplemented with 10 % foetal bovine serum (FBS) and x1 penicillin/streptomycin in 25 cm³. Cells were trypsinised once their confluence achieved 90 % at a ratio of 1:2 using 0.05 % trypsin/EDTA in phosphate buffered Saline (PBS) incubated at 37 °C for 5 min.

4.2.14.2 Cell preparation and in-vivo proteasome inhibition

Cells were trypsinised, divided equally into 24 well plate (VWR, Germany) and allowed to grow for 24 h. Medium (glucose DMEM supplemented with 10 % fetal calf serum and 1x penicillin/streptomycin) was removed and 500 µl fresh medium added. Two repetitions were performed for each inhibitor as well as a positive control, using MG132 and a blank with DMSO. 1 µl of inhibitor (between 20-100 mM initial concentration), DMSO or MG132 was added per well and allowed to incubate at 37 °C under 5 % CO₂ for 4-8 h depending on the inhibitor. 15 ng of Interleukin-1 alpha (IL-1 α) was added directly to the wells in order to induce NF- κ B activation and allowed to incubate for 20 min at 37 °C under 5 % CO₂ (Nemeth et al., 2004). Medium was subsequently removed and treated cells were washed twice with PBS and harvested by adding 70 µl of mammalian protein extraction reagent (M-PER) and scraped with the pipette tip. Cell debris was removed through centrifugation at 15000 rpm for 15 min and supernatant stored at -20 °C.

4.2.14.3 Protein quantification for HeLa cell lysis

Protein quantification was performed using the Bradford test. 200 μl of Bradford solution was pipetted in a transparent 96 well plate. 1 μl of the BSA solution (0.15 - 1 mg ml^{-1}) or the cell lysis supernatant was subsequently added and the absorption was measured with a UV-vis spectrophotometer at 595 nm . The amount of protein was estimated using BSA as standard protein at a concentration of 9 mg/ml .

4.2.14.4 Western blot for HeLa cell lysis

For the $\text{I}\kappa\beta\alpha$ degradation westernblot, the protein concentrations of cytosolic extracts was determined using the Bradford test as explained in section 4.2.14.3. Samples of 8 μg were separated in a 15 % SDS-gel and transferred to a polyvinylidene fluoride (PVDF) membrane for 1 h at 100 mA. PVDF membrane was previously activated through a 20 s exposure to 100 % methanol followed by incubation of 1 min with ultrapure water and 5 min with transfer buffer. Post protein transfer membrane was blocked with 5 % blocking grade powdered milk in Tris Buffer Saline (TBS) with 0.05 % Tween-20 for 1 h.

4.2.14.5 $\text{I}\kappa\beta\alpha$ westernblot

The membrane was probed at 4 $^{\circ}\text{C}$ with a mouse anti- $\text{I}\kappa\beta\alpha$ antibody diluted 1:4000 in a solution of 1 % blocking grade powdered milk in TBS with 0.05 % Tween-20 overnight. Excess of the antibody was removed through x 5 20min washes of the membrane with x 1 TBS with 0.05 % Tween-20 and incubated with a secondary horseradish peroxidase-conjugated rabbit anti-mouse antibody for 1 h at room temperature. Subsequently, x 5 20 min washes of the membrane were performed with TBS containing 0.05 % Tween-20, bands were detected using ECL plus western blotting detection system and visualized using BioMax[®] Light Films.

Correct protein loading and transfer efficiency was proven by using glyceraldehyde-3-phosphate dehydrogenase (GAPDH) as a standard.

4.2.14.6 GAPDH westernblot

The membrane containing the standard protein was subsequently probed at 4 °C with a mouse anti-GAPDH antibody diluted 1:40000 in a solution of 1 % blocking grade powdered milk (Roth) in TBS with 0.05 % Tween-20 overnight. Excess antibody binding was removed through x5 20min washes of the membrane with x 1 TBS with 0.05 % Tween-20 and incubated with a secondary horseradish peroxidase-conjugated rabbit anti-mouse antibody for 1 h at room temperature. The excess antibody was removed through x 5 20min washes of the membrane with x1 TBS with 0.05 % Tween-20 and developed as described above.

4.2.15 5-Lipoxygenase inhibitor characterisation

The 5-Lipoxygenase (5-LOX) inhibitor assay was performed, using a 96 well plate, according to the oxidation of the substrate dichlorodihydrofluorescein diacetate (H2DCFDA) to Xuorescent 2,7-dichloro-Xuorescein (DCF) product using lysate preparation of human 5-LOX (Pufahl et al., 2007).

Selected inhibitors at concentrations of 1 nM – 2 mM were incubated for 20 min at room temperature with a solution of 500 mU lysate preparation of human 5-LOX (Cayman, US) dissolved in a 50 mM Tris/HCl pH 7.5 solution containing 2 mM CaCl₂ and 2 mM of Ethylendiamin-tetraacetat (EDTA). A final concentration of 10 µM H2DCFDA was added and allowed to further incubate for 10 min at room temperature. Subsequently a final concentration of 3 mM arachidonic acid with 10 µM ATP was added to the reaction and incubated at room temperature for 2 h with shacking. The reaction is then stopped by additional equal amounts of acetonitrile (80 µL) and fluorescence is measured at $\lambda_{exc} = 500$, $\lambda_{em} = 520$ nm. All inhibitors hereby analysed were dissolved in DMSO, therefore the % rest activity was calculated using a DMSO standard as 100 % initial activity. The values were obtained by plotting the percent inhibition against inhibitor concentration and fitting the experimental data to equation: % inhibition = $100 [I]_0 / (IC_{50} + [I]_0)$.

5 Results and Discussion

5.1 Structural characterisation of decarboxylated peptides as 20S proteasome inhibitors

5.1.1 Initial characterisation and optimisation of side chains

Synthesis and chemical characterisation of the compounds described in this section were performed by Prof. Luis Moroder, Prof. Joëlle Vidal, at the Max-Planck-Institut für Biochemie and Université de Rennes respectively. *In-vitro* assays of compounds **2a-g** were carried out by Dr. Xavier Marechal and Prof. Michèle Reboud-Ravaux's at the Université Paris 6-UPMC and can be found in the following paper (Groll et al., 2010).

The aim of this study was to synthesis, characterise and optimise β 5-subunit specific linear TMC-95A constructs through the maintenance of the original TMC-95A scaffold (**Fig. 10**). The crystal structure of TMC-95A revealed that the tripeptide structure of TMC-95A, with a Tyr-Asn-oxidizedTrp amino acid sequence, binds into the S4, S3 and S2 proteasomal specificity pockets respectively (Groll et al., 2001). Additionally, it could be clearly observed that this tripeptide enthalpically favours the interaction with the β -subunit active sites, an effect that is mediated through H-bonds between the peptide backbone and the protein counterpart by formation of an antiparallel β -sheet.

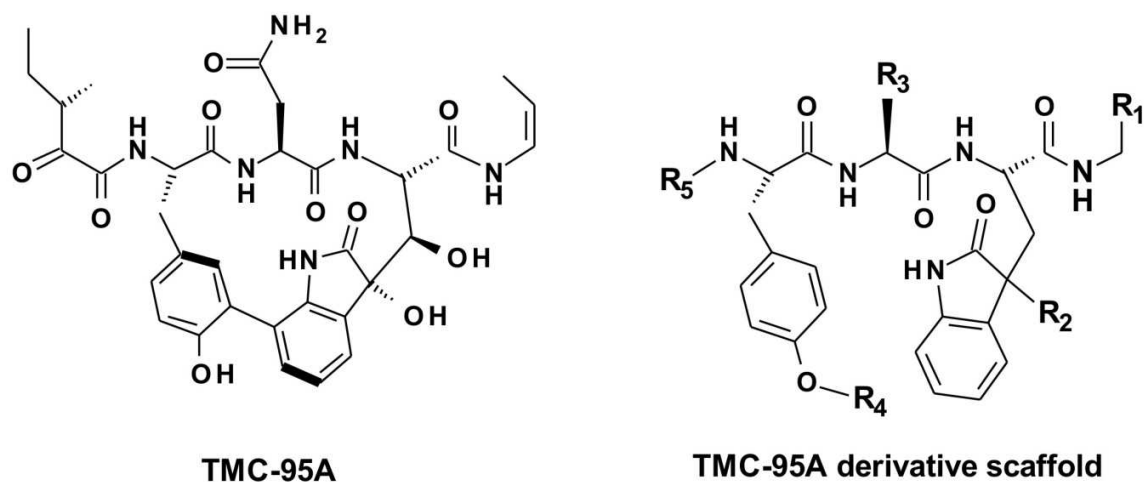


Fig. 10: Chemical structure of TMC-95A and the scaffold used for optimisation of TMC-95 derivative

The prior documented decrease in affinity through the removal of this tripeptide and the oxindole group found in P2 were taken into account and therefore this tripeptide structure and the oxindole group were maintained in this scaffold (Basse et al., 2007; Groll, Gotz et al., 2006). Additionally, for the ease of the chemical synthesis of these compounds the asparagine in P3 was substituted by an alanine residue. Our initial compound **2a**, bearing the scaffold described above and a phenyl group in R¹, a benzyl ring in R⁴ and a BOC protecting group in R⁵, was tested *in-vitro* yielding only 20 % inhibition at 100 μM. Nevertheless, these initial results were followed up by performing a structural evaluation of this inhibitor complexed with the 20S proteasome in order to characterise and further optimise the different specificity pocket interactions of the CT-like active site with the distinct ligand side chains. As summarised in the methods section, **2a** was soaked with yeast CP crystals for 48 h, and a full data set was collected and processed at 2.4 Å ($R_{\text{free}} = 0.231$) at PXI at the Paul Scherer Institute, Swiss Light Source, Villigen, Switzerland (**Table 3**).

Data collection and refinements of CP:2a					
<u>Crystal parameters</u>		<u>Data collection</u>		<u>Refinement (CNS)</u>	
Space group	P2 ₁	Beamline	X06SA, SLS	Resolution range (Å)	15-2.4
Cell constants (one molecule / AU ^a)	a=136.5 Å; b=301.1 Å; c=145.4 Å; β=113.6 °	Wavelength (Å)	1.0	No. refl. working set	393694
		Resolution range (Å) ^b	50-2.4 (2.5-2.4)	No. refl. test set	20529
		No. observations	1721731	No. non hydrogen	49572
		No. unique reflections ^c	415923	Solvent water	1337
		Completeness (%) ^b	99.5 (99.7)	Inhibitor (non hydrogen)	108
		R _{merge} (%) ^{b, d}	8.1 (51.7)	R _{work} /R _{free} (%) ^e	23.1 / 24.8
		I/s (I) ^b	11.1 (2.7)	rmsd bond (Å) / (°) ^f	0.007 / 1.3
				Ramachandran Plot (%) ^g	95.9/3.5/0.6

Table 3 Data collection and refinement statistics for yeast CP:2a

a. Asymmetric unit, b. values in parentheses the resolution range, completeness, R_{merge} and I/σ(I) correspond to the resolution shell, c. number of unique reflections; friedel pairs were treated as identical reflections, d. $R_{\text{merge}}(I) = \frac{\sum_{\text{hkl}} \sum_j |I(\text{hkl})_j - \langle I(\text{hkl}) \rangle|}{\sum_{\text{hkl}} I(\text{hkl})}$, where $I(\text{hkl})_j$ is the j th measurement of the intensity of reflection hkl and $\langle I(\text{hkl}) \rangle$ is the average intensity, e. is the $R = \frac{\sum_{\text{hkl}} | |F_{\text{obs}}| - |F_{\text{calc}}| |}{\sum_{\text{hkl}} |F_{\text{obs}}|}$, where R_{free} (A. Brünger, 1992; AT. Brünger et al., 1998) is calculated only with a randomly chosen 5 % of reflections which were not included in structure refinement. R_{work} is calculated for the remaining reflections, f. is the deviations from ideal bond lengths/angles and g. is the number of residues in the Ramachandran plot for favoured region / allowed region / outlier region.

The data set revealed a clear electron density of **2a** bound only to the CT-like active site. As a rule, upon peptide-bond hydrolysis, the products are released through repulsion between the active site nucleophilic Thr10^y and the newly generated carboxy-terminus of the cleavage fragments. Nevertheless, the crystal structure of the CP:2a-complex showed identical positioning of the tripeptide scaffold backbone, as previously observed in TMC-95A, whereby side chains of the tripeptide are bound to the S1, S3 and S4 proteasomal specificity pockets (**Fig. 11**).

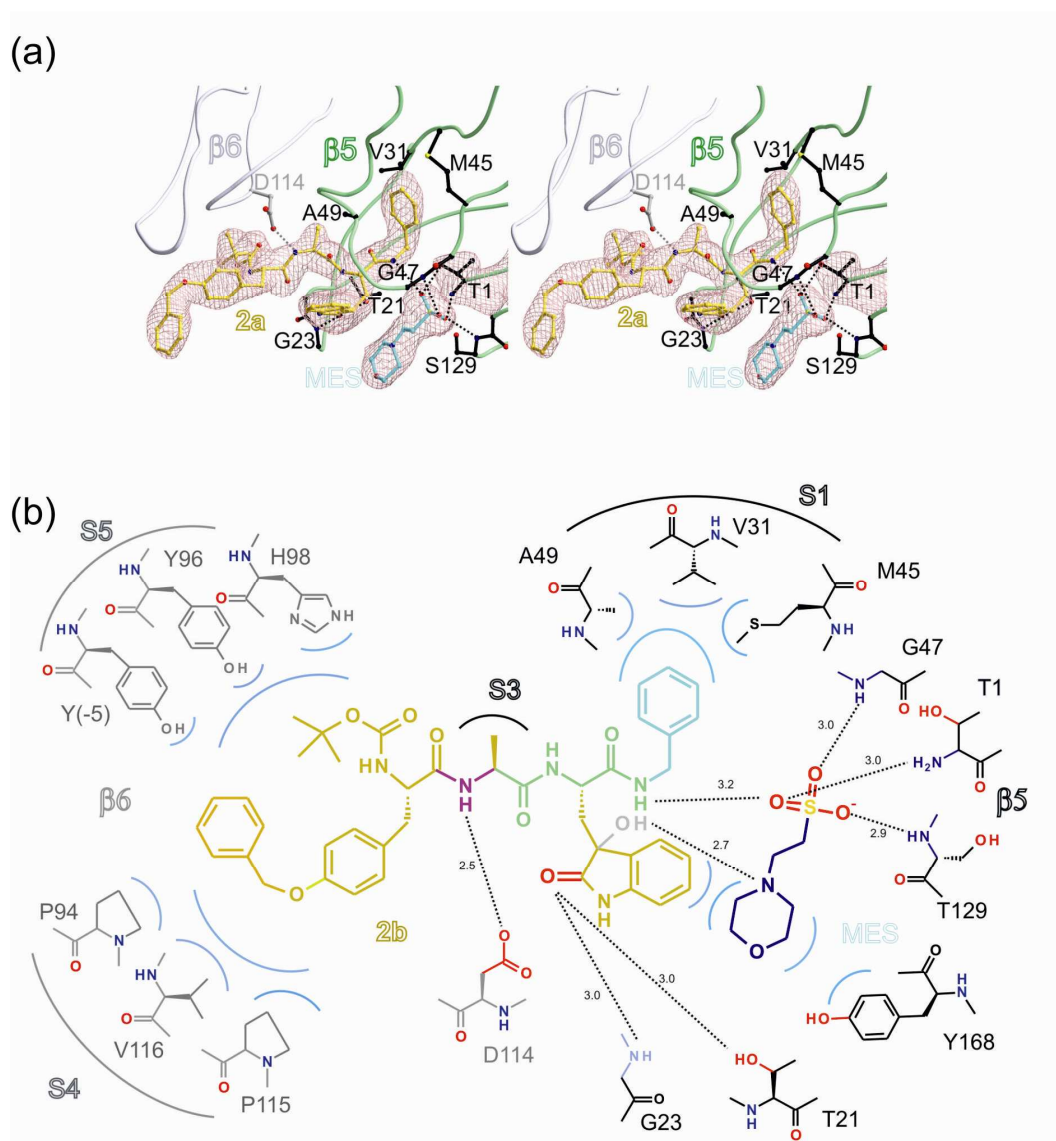


Fig. 11: Complexed structure of CP:2a

(a) Stereorepresentation of the complex structure CP:2a, main interactions between 2a, shown in yellow, and the different side chains of the CT-like active site illustrated in grey and black. 2a, here shows a clear defined omit map $2F_o - F_c$ as well as an additional N-morpholino-ethane sulfonic acid molecule (MES) from the crystallisation conditions, represented in dark blue. H-bonds are depicted in dotted lines and important amino acids are shown in black colour. (b) Schematic view of 2a/2b in complex with CT-like active site, Van-der-Waals interactions are shown by blue semicircles while H-bonds are depicted with black dotted lines (Groll et al., 2010).

The phenyl group in R¹, was found to protrude into the S1 pocket shaped by Met45, Val31 and Ala49, forming a plenitude of Van-der-Waals interactions with these amino acid residues. The S4 pocket, located in β 6, was occupied by the benzyl ring of R⁴ forming Van-der-Waals interactions with Tyr96, Tyr-5, Pro94, Pro115 and Val116. Additionally the Di-tert-butyl dicarbonate (BOC) group in R⁵ protrudes into the β 6 located the S5 pocket forming a series of Van-der-Waals interactions. (**Fig. 11**). Moreover, the crystal structure of the CP:**2a**-complex exhibited a defined electron density of solely the (*S*)-epimer which has the same relative configuration than that of TMC-95A (**Fig. 11**). Even though Nuclear magnetic resonance (NMR)-analysis revealed that **2a** is an equilibrated mixture of (*R*)- and (*S*)-epimers at the asymmetric carbon of the oxindole side chain (*via* keto-enol tautomerization). Inspired by the structure of TMC-95A, the hydrogen atom adjacent to the oxo-group was replaced with a hydroxyl-group in either (*R*)-(same relative configuration than in TMC-95A) or (*S*)-configuration, yielding the conformationally stable epimers **2b** and **2c** respectively. It must be mentioned that due to the Cahn–Ingold–Prelog (CIP)-rules, priorities of H and OH are hereby reversed, so although the relative spatial arrangement of the side chain and the oxindole ring are the same, the absolute configuration (*R*) or (*S*) are reversed.

In-vitro analysis of **2b** showed a five-fold decrease in IC₅₀ of 1.5 μ M compared to 6.8 μ M in **2c**. These promising results were followed up by a crystallographic analysis, whereby yeast CP:**2b** structure was determined to 2.5 Å ($R_{\text{free}} = 0.221$) and CP:**2c** at 2.5 Å ($R_{\text{free}} = 0.226$) (**Table 4**).

Data collection and refinements of CP:2b					
<u>Crystal parameters</u>		<u>Data collection</u>		<u>Refinement (CNS)</u>	
Space group	P2 ₁	Beamline	X06SA, SLS	Resolution range (Å)	15-2.5
Cell constants (one molecule / AU ^a)	a=135.4 Å; b=299.9 Å, c=144.3 Å; β=112.9 °	Wavelength (Å)	1.0	No. refl. working set	335786
		Resolution range (Å) ^b	50-2.5 (2.6-2.5) 1244919	No. refl. test set	17620
		No. observations	354718	No. non hydrogen	49572
		No. unique reflections ^c	97.3 (90.2)	Solvent water	1358
		Completeness (%) ^b	5.6 (43.4)	Inhibitor (non hydrogen)	110
		R _{merge} (%) ^{b, d}	17.1 (3.5)	R _{work} /R _{free} (%) ^e	22.1 / 24.3
		I/s (I) ^b	17.1 (3.5)	rmsd bond (Å) / (°) ^f	0.007 / 1.3
				Ramachandran Plot (%) ^g	95.1/4.3/0.6

Data collection and refinements of CP:2c					
<u>Crystal parameters</u>		<u>Data collection</u>		<u>Refinement (CNS)</u>	
Space group	P2 ₁	Beamline	X06SA, SLS	Resolution range (Å)	15-2.5
Cell constants (one molecule / AU ^a)	a=135.5 Å; b=301.0 Å, c=144.4 Å; β=112.9 °	Wavelength (Å)	1.0	No. refl. working set	268370
		Resolution range (Å) ^b	50-2.5 (2.6-2.5) 1255074	No. refl. test set	14154
		No. observations	359106	No. non hydrogen	49548
		No. unique reflections ^c	99.6 (99.7)	Solvent water	1334
		Completeness (%) ^b	8.5 (53.3)	Inhibitor (non hydrogen)	110
		R _{merge} (%) ^{b, d}	10.1 (2.3)	R _{work} /R _{free} (%) ^e	22.6 / 24.8
		I/s (I) ^b	10.1 (2.3)	rmsd bond (Å) / (°) ^f	0.007 / 1.3
				Ramachandran Plot (%) ^g	94.3/4.9/0.8

Table 4 Data collection and refinement statistics 2b and 2c.

Summary of the crystal parameters, data collection and refinements of the crystal data whereby a-g are described in Table 3.

The crystallographic data of **2b** and **2c** complexed at the CT-like active site displayed identical specificity and binding behaviour, except for the oxindole-side chain in P2, which is rotated by 90 degrees counter-clockwise in the (*S*)-epimer (**Fig. 12**). Even though, this introduced OH-group is well defined in the crystal structure of the CP:**2b** and CP:**2c**-complexes, it is solvent exposed, as the 20S proteasome does not possess a defined S2 specificity pocket. Thus, structurally both compounds only differ from each other in their H-bonding interaction of the P2-oxo-group with the electron donors of β 5-Gly23NH and β 5-Thr21OH, which are disrupted in the CP:**2c**-complex.

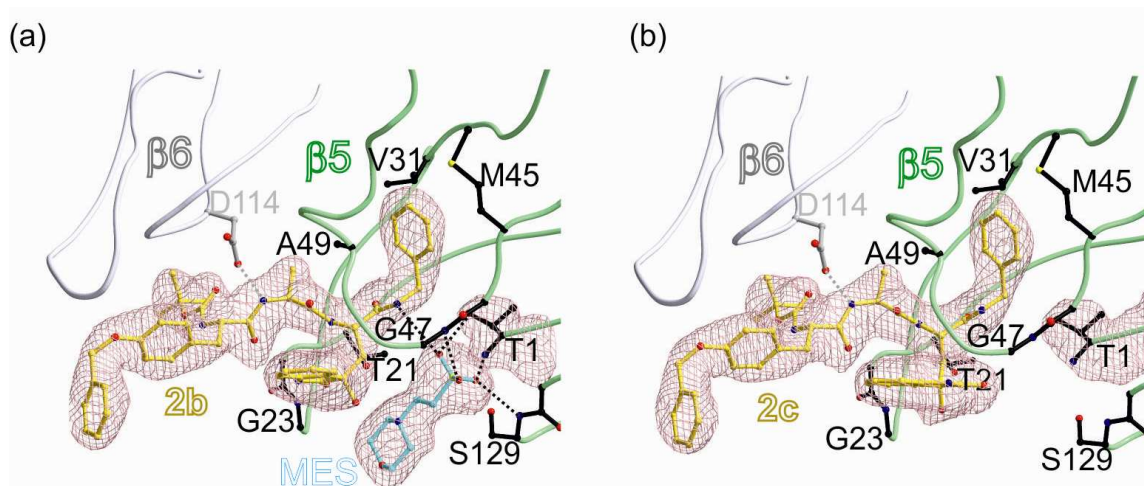


Fig. 12: Complex structure of CP with (a) 2b and (b) 2c

Compounds **2b** and **2c** were bound to the CT-like active site formed by β 5 and β 6, represented in a green and grey coloured cartoon loop respectively. Defined electron density of both the inhibitor **2b** and the MES molecule is shown on the left, whereas electron density is only observed for **2c** due to the position of the OH in the oxyindole moiety which prevents binding of the MES molecule. Important amino acids in this inhibitor binding are labelled and depicted in black. Hydrogen bonds are shown by dotted black lines

These data conclude that although **2a** is an equilibrated mixture of two epimers in solution, only the compound with the highest binding affinity was shown in the electron density as it is selected by the crystal in crystal soaking. Furthermore, it is not just the different epimers which are selected in the crystal structure but also the crystallized protein will preferably

interact with the ligand conformation that best complements the distinct substrate binding pockets. Therefore, the crystal structure of the complex will provide a snap-shot of the ligand conformation with the highest binding affinity for the catalytic site, regardless of the binding kinetics. This conformation was utilised as a template-binding and further improvement of the ligand binding affinity was performed through optimisation of the different side chains.

Derivatisations of the distinct side chains of **2b** to further characterize its inhibition profile were therefore undertaken. The substitution of the phenyl group in R¹ by a hydrogen group, compound **2f**, for the (*R*)-conformer and **2g** for the (*S*)-conformer, are accompanied by significant loss of inhibitory potency, a decrease by a factor of 35 and 70 respectively. The crystallographic data clearly revealed that the decrease in affinity is due to the loss of the interactions with the S1 pocket described above. The importance of the P1 residue and the S1 subunit pocket is a fact that has been also observed in the binding configuration of the β -lactones, with the small natural product Omuralide as the most prominent example (Corey & Li, 1999). This inhibitor represents the best example of the importance of the P1-site, since this compound lacks any peptide backbone, however it still possess a high affinity towards the 20S proteasome. Compound **2f** is a further example confirming the importance of the P1-site upon binding to the proteasome.

Interestingly, deprotection of the side chains in **2b** resulted in a significant decrease in proteasomal binding affinity. Removal of tyrosine in R⁴ (compound **2d**) led to a 6.5 fold increase in IC₅₀, a result which was followed up by a crystallographic analysis. (CP:**2d** yielded a data set at 2.6 Å ($R_{\text{free}} = 0.249$) (Table 5).

Data collection and refinements of CP:2d					
<u>Crystal parameters</u>		<u>Data collection</u>		<u>Refinement (CNS)</u>	
Space group	P2 ₁	Beamline	X06SA, SLS	Resolution range (Å)	15-2.6
Cell constants (one molecule / AU ^a)	a=135.4 Å; b=299. Å, c=144.3 Å; β=112.9 °	Wavelength (Å)	1.0	No. refl. working set	387543
		Resolution range (Å) ^b	50-2.6 (2.7-2.6) 1424004	No. refl. test set	20221
		No. observations	409423	No. non hydrogen	49548
		No. unique reflections ^c	99.5 (99.4)	Solvent water	1335
		Completeness (%) ^b	6.1 (62.7)	Inhibitor (non hydrogen)	96
		R _{merge} (%) ^{b, d}	15.0 (2.8)	R _{work} /R _{free} (%) ^e	24.9 / 26.4
		I/s (I) ^b	15.0 (2.8)	rmsd bond (Å) / (°) ^f	0.007 / 1.5
				Ramachandran Plot (%) ^g	95.3/4.0/0.7

Table 5 Data collection and refinement statistics 2d

Summary of the crystal parameters, data collection and refinements of the crystal data, whereby. a-g are as in **Table 3**.

The crystal structure of CP:**2d** complex did not show any alteration in the binding mode to the CT-like active site but still confirms that the R⁴ interactions with the 20S proteasome are of vital importance. This moiety exploits the large hydrophobic S4 pocket causing structural rearrangement of Tyr96 and further stabilising these compounds through a series of hydrophobic interactions with Tyr-5, Pro94, Pro115 and Val116 of the adjacent subunit.

Along with the protected tyrosine side chain in P4, the deprotection of the BOC group in R⁵, compound **2e** also illustrated an increase in its IC₅₀ by a factor of 6.3. Crystallographic analysis of CP:**2e** yielded a 2.7 Å data set with an R_{free} = 0.236 (**Table 6**) and illustrated a disruption of β6-His98 interaction with this protecting group's which caused a decreased affinity towards the 20S proteasome.

Data collection and refinements of CP:2e					
<u>Crystal parameters</u>		<u>Data collection</u>		<u>Refinement (CNS)</u>	
Space group	P2 ₁	Beamline	X06SA, SLS	Resolution range (Å)	15-2.7
Cell constants (one molecule / AU ^a)	a=135.5 Å; b=301.0 Å, c=144.4 Å; β=112.9 °	Wavelength (Å)	1.0	No. refl. working set	269106
		Resolution range (Å) ^b	50-2.7 (2.8-2.7) 1086242	No. refl. test set	14054
		No. observations	284237	No. non hydrogen	49572
		No. unique reflections ^c	99.1 (96.3)	Solvent water	1329
		Completeness (%) ^b	6.3 (44.4)	Inhibitor (non hydrogen)	96
		R _{merge} (%) ^{b, d}	17.0 (3.7)	R _{work} /R _{free} (%) ^e	23.6 / 26.2
		I/s (I) ^b	17.0 (3.7)	rmsd bond (Å) / (°) ^f	0.007 / 1.5
				Ramachandran Plot (%) ^g	94.3/4.9/0.8

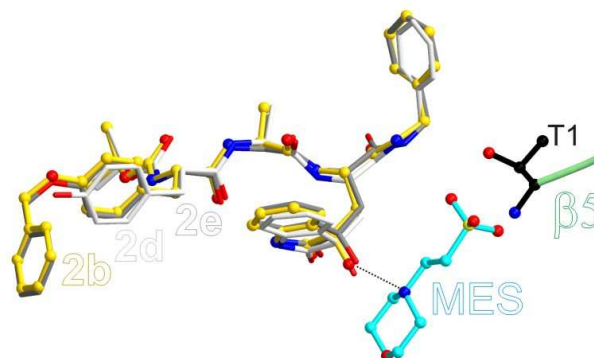
Table 6 Data collection and refinement statistics 2d

Summary of the crystal parameters, data collection and refinements of the crystal dat, whereby. a-g are described in **Table 3**.

Both R⁴ and R⁵ side chains located in S4-S5 provide this decarboxylated non-covalent natural product with additional interactions which highly stabilise these inhibitors in the CP and help with their lack of rigidity compared to TMC-95A (**Fig. 10**). Remarkably, all side chains were found to aid in the binding of this set of inhibitors. Side chains between R¹-R⁵ are highly optimised for their complementary binding to the CT like active site resulting in subunit specificity and supporting the enthalpically favoured antiparallel β-sheet formed by its peptide backbone interactions.

In addition to the initial characterisation, the electron density of most of these CP:peptide complexes uncovered the presence of an N-morpholino-ethane sulfonic acid molecule (MES), derived from the crystallisation buffer. This MES molecule was shown to further enthalpically stabilise the linear peptide through Van-der-Waals interactions and through the formation of a H-bonding network between active site residue Thr1 (**Fig. 13**).

(a)



(b)

Compound	R ¹	(C* R ² config.)	R ⁴	R ⁵	IC ₅₀ (μM)
2a	Ph	H (<i>S/R</i>)	Bn	Boc	20% at 100 μM
2b	Ph	OH (<i>R</i>)	Bn	Boc	1.5 ± 0.1
2c	Ph	OH (<i>S</i>)	Bn	Boc	6.8 ± 0.1
2d	Ph	OH (<i>R</i>)	H	Boc	9.7 ± 0.3
2e	Ph	OH (<i>R</i>)	Bn	H	9.4 ± 0.4
2f	H	OH (<i>R</i>)	Bn	Boc	52.6 ± 0.1
2g	H	OH (<i>S</i>)	Bn	Boc	~ 100
BIA					5.5 ^[a]

Fig. 13: TMC-95A derivatives

(a) Crystal structures of yeast CP in complex with compounds **2b**, **2d** and **2e** depicted in yellow, grey and white respectively. (b) Table listing the summary of all IC₅₀ performed.

This molecule aided in the binding of these set of linear compounds, as shown in the complexed crystal structure of CP:**2b**, whereby a H-bonding network is seen between the inhibitors, the MES molecule and β5-Gly47N. The Gly47 residue is the primary component in the proteasome's oxyanion hole; an area normally populated by the active residue of the ligand's functional groups of most covalently bound inhibitors. Interestingly, this MES-molecule was not observed in the crystal structure of the CP:TMC95-A-complex or the CP:**2c** complex. As illustrated in **Fig. 14** the CP:**2c** complex demonstrates the positioning of the OH in the oxyindole moiety which, due to its stereochemistry, is no longer forming a H-bond with the nitrogen of

the N-morpholino ring hereby disrupting the H-bonding network. In the case of the CP:TMC95-A-complex the situation is comparable as the rigid structure of this cyclic tripeptide prevents the adequate positioning of the OH group towards the oxyindole.

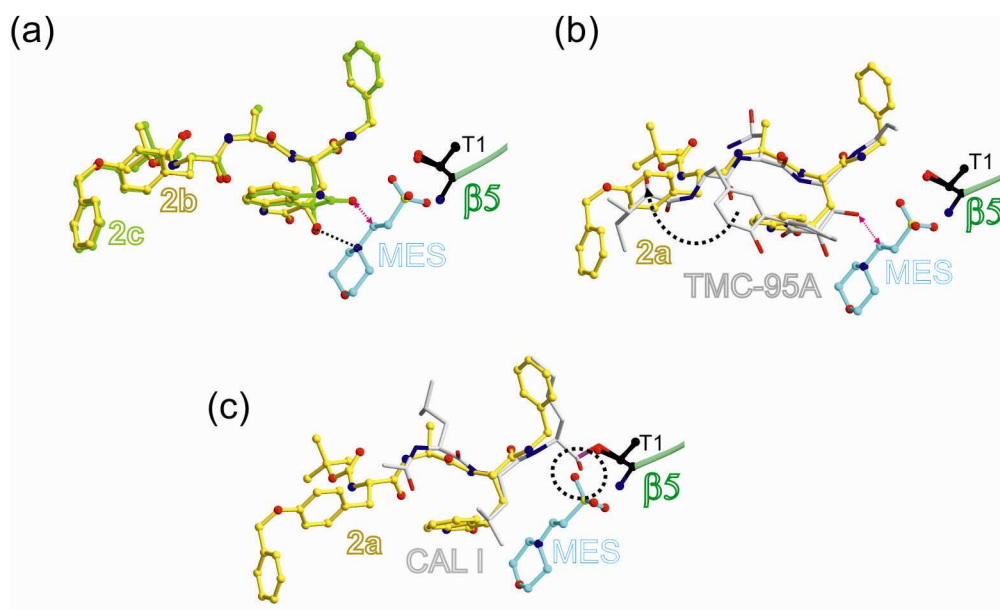


Fig. 14: MES molecule observed in CP:TMC-95A derivatives

Structural superposition of the crystal structures of (a) enantiomers **2b** and **2c** with the yeast CP, proving the importance of the OH orientation towards the oxyindole group (Fig. 10) (b) TMC-95A and **2a** in complex with yeast CP revealing the concerted movement of the side chain R² preventing the interactions necessary for the binding of the MES molecule into the oxyanion hole (c) the aldehyde peptide, Calpain inhibitor I, with **2a**. Hereby, Thr1 active residue of CT-like active site is shown in black and MES in blue. Compounds 2a-2c and TMC-95A are depicted in yellow, green and grey respectively.

Subsequent *in-vitro* assays were performed using 50 mM MES in order to further determine whether this is a synergistic effect between the MES molecule and the respective decarboxylated peptide. However, MES did not show any effect on the IC₅₀ values of these linear TMC-95A-analogues. Nevertheless the synergistic interactions observed between MES and the linear compounds can be taken into account for further optimisation of these non-covalent binding ligands. Thus, a covalent linkage of the decarboxylated peptides, forming with

MES a network of hydrogen bonds with the nucleophilic Thr1 and the oxyanion hole, might suggest a novel strategy for proteasomal drug development. Therefore, a fragment based evolutionary approach could be undertaken to increase the conformational complementarity of CP and ligands, leading to the development of new rationally designed proteasomal inhibitors.

5.1.2 Bivalent and Monovalent inhibitors

The crystal structure of the eukaryotic 20S proteasome revealed an interesting catalytic activity and a unique topology in this multicatalytical degradation machinery. The C2 symmetry of its structure and its defined layout, as well as defined distances between the different active sites, have been characteristics that were quickly exploited in the design of proteasome inhibitors. Whereby, the production of bi- and multi-valent ligands were synthesised to make use of these characteristics. As illustrated in **Fig. 15** the spacing between the two Thr1 in $\beta 5$'s are of 49 Å, a distance that is approximately equivalent to the length of a peptide backbone of 15 amino acids (Groll et al., 1997; Loidl, Groll, Musiol, Huber, & Moroder, 1999). Previous bivalent inhibitors have been synthesised using; i) aldehyde head groups, as they have been highly characterised, and ii) polyethylene glycol (PEG) as spacers, due to their advantageous characteristics such as flexibility, linearity, solubility in aqueous solutions and protease resistance (Loidl et al., 1999). This set of inhibitors have been synthesised both as homobivalent and heterobivalent compounds and they have proven to have a significantly reduced IC₅₀ value compared to their monovalent counterparts (Borissenko & Groll, 2007).

The bivalent strategy was attempted with the monomeric inhibitor **2b**, whereby different chain lengths were tested *in-vitro* and *in-vivo*. Co-crystallisation of these inhibitors with yeast CP was performed to undertake a structural analysis of these inhibitors.

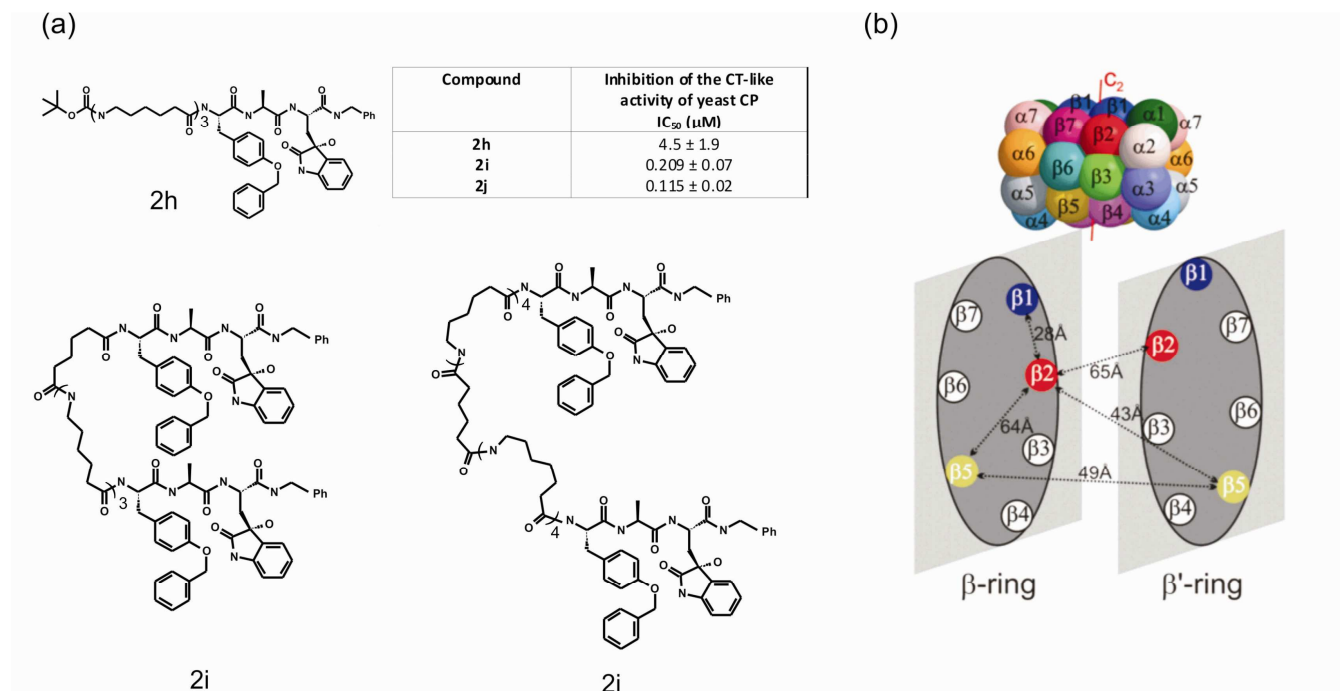


Fig. 15: Bivalent TMC-95A derivatives

(a) Chemical structures of **2h-j** and their IC₅₀ (μM) of the CT-like activity of the yeast CP. (b) Respective distances between the six active sites in the yeast proteasome derived from crystallographic results (Borissenko & Groll, 2007).

The linker added to **2b** was that of an extended aliphatic carbon chain with intermediate peptide bonds to increase solubility in aqueous solutions. Therefore the decarboxylated peptide is either of monovalent (**2h**) or bivalent nature (**2i** and **2j**).

Whereas the monovalent compound **2h** showed an increase in the IC₅₀ from the 1.5 μM of **2b** to 4.5 μM the bivalent inhibitors **2i** and **2j** resulted in a significant decrease in the IC₅₀ values ranging in the nanomolar scale (**2i**: 209 nM and **2j**: 115 nM). In order to further clarify this change in activity a crystallographic analysis of these compounds was performed. Full data sets were collected of **2h**, **2i** and **2j** at 3.1, 2.9 and 2.8 Å with an R_{free} = 0.223, 0.2205 and 0.235 respectively (**Table 7**).

Data collection and refinements of CP:2h					
<u>Crystal parameters</u>		<u>Data collection</u>		<u>Refinement (REFMAC5)</u>	
Space group	P2 ₁	Beamline	X06SA, SLS	Resolution range (Å)	15-3.1
Cell constants (one molecule / AU ^a)	a=135.7 Å;	Wavelength (Å)	1.0	No of atoms	51011
	b=301.4 Å;			Protein	49548
	c=144.6 Å;	Resolution range (Å) ^b	15-3.1 (3.1- 3.0)	Water	1342
	β=112.8 °			R _{work} /R _{free} (%) ^e	21.6 / 22.3
		No. observations	724229	rmsd bond deviations bond length (Å) (°) ^f	0.005/0.874
		No. unique reflections ^c	192530	Average B-factor (Å ²)	66.412
		Completeness (%) ^b	99.6 (98.5)	Ramachandran Plot (%) ^g	6077 (96.3%)
		R _{merge} (%) ^{b, d}	11.3 (49.6)		195 (3.1%)
		I/s (I) ^b	10.38 (2.71)		40 (0.6%)

Data collection and refinements of CP:2i					
<u>Crystal parameters</u>		<u>Data collection</u>		<u>Refinement (REFMAC5)</u>	
Space group	P2 ₁	Beamline	X06SA, SLS	Resolution range (Å)	15-2.9
Cell constants (one molecule / AU ^a)	a=135.4 Å;	Wavelength (Å)	1.0	No of atoms	51128
	b=299.2 Å;			Protein	49548
	c=144.7 Å;	Resolution range (Å) ^b	15-2.9 (2.9-2.8)	Water	1342
	β=113.0 °			R _{work} /R _{free} (%) ^e	22.0 / 22.7
		No. observations	789038	rmsd bond deviations bond length (Å) (°) ^f	0.004/0.856
		No. unique reflections ^c	231143	Average B-factor (Å ²)	67.796
		Completeness (%) ^b	98.9 (97.4)	Ramachandran Plot (%) ^g	6122 (97.0%)
		R _{merge} (%) ^{b, d}	8.4 (46.0)		162 (2.6%)
		I/s (I) ^b	11.58 (2.02)		28 (0.4%)

Data collection and refinements of CP:2h					
<u>Crystal parameters</u>		<u>Data collection</u>		<u>Refinement (REFMAC5)</u>	
Space group	P2 ₁	Beamline	X06SA, SLS	Resolution range (Å)	15-2.8
Cell constants (one molecule / AU ^a)	a=135.8 Å;	Wavelength (Å)	1.0	No of atoms	51021
	b=300.2 Å;			Protein	49548
	c=144.3 Å;	Resolution	20-2.8	Water	1342
	β=112.9 °	range (Å) ^b	(2.8-2.7)	R _{work} /R _{free} (%) ^e	23.5 / 24.1
		No. observations	870042	rmsd bond deviations bond	0.004/0.823
		No. unique reflections ^c	257968	length (Å) (°) ^f	
		Completeness (%) ^b	99.0 (98.8)	Average B-factor (Å ²)	73.961
		R _{merge} (%) ^{b,d}	7.0 (58.1)	Ramachandran Plot	6135 (97.2%)
		I/s (I) ^b	16.93 (2.88)	(%) ^g	149 (2.4%)
					28 (0.4%)

Table 7 Data collection and refinement statistics 2h-j in complex with yeast CP

a-g according to **Table 3**.

Calculated $2F_o - F_c$ revealed clear electron densities of all three compounds. As expected, the inhibitors exhibit similar positioning of the tripeptide scaffold maintaining each side chain in the appropriate specificity pocket similar as described for the CP:**2b** crystal structure. However, due to the high flexibility of the linker sequence the datasets lack defined density for the linker part of the inhibitor (**Fig. 16**).

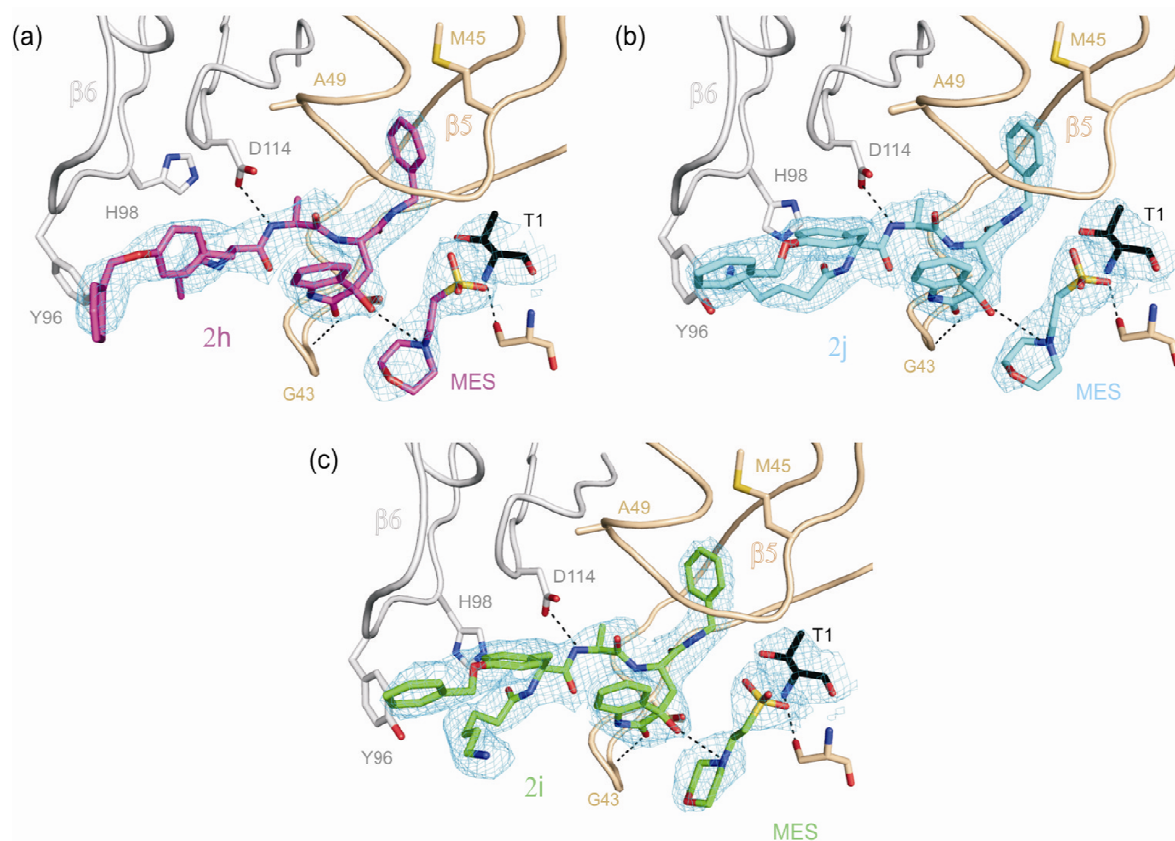


Fig. 16: Complex structure of CP: 2h-2j

Yeast proteasome complexed with ligand (a) **2h** (b) **2j** and (c) **2i** depicted in purple, blue and green respectively. $\beta 5$ and $\beta 6$ are shown in cartoon representation depicted in wheat and grey colour respectively; the H-bonding network observed in this set of compounds are represented in black dotted lines, important amino acids are shown in stick form.

The superposition of **2i** and **2b** showed no concerted movement of any of the side chains in the active site or in the inhibitor side chains (**Fig. 17**). However, **2h** and **2j** did show a concerted movement of Try96 and His98 hereby performing hydrogen bonds with the first part of the linker.

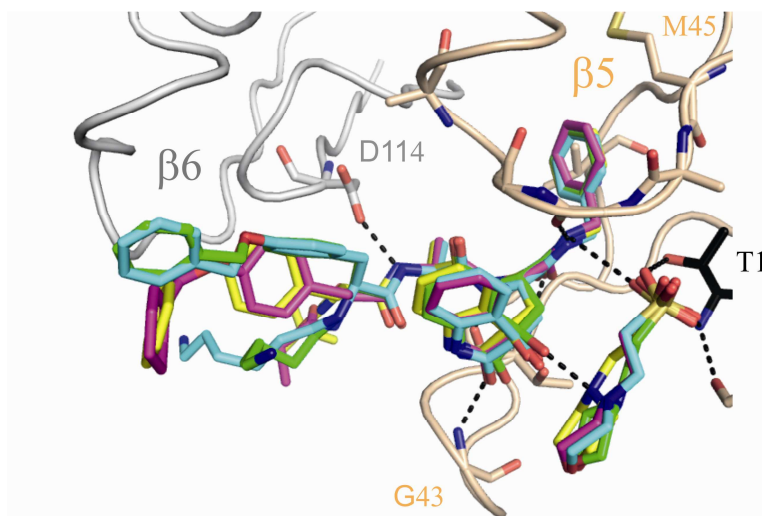


Fig. 17: Structural superposition of bivalent TMC-95A derivatives

Structural superposition of yeast CP in complex with compounds **2h**, **2j**, **2i** and **2b** depicted in purple, blue, green and yellow respectively.

These results prove that it is only the bivalency of this set of inhibitors which give rise to the decreased IC_{50} values by two orders of magnitude. In addition, there was a MES molecule observed in all structures forming a multitude of hydrogen bonding interactions and further stabilising these inhibitors in place as observed for compound **2b**.

5.1.3 Cell accessibility assays

In-vivo experiments of bortezomib revealed that proteasome inhibition produces cellular responses through the alteration of the NF- κ B pathway. NF- κ B is involved in the regulation of the expression of genes involved in cell apoptosis and proliferation and it is over expressed in several tumours. Although NF- κ B is normally dormant and cytosolically bound to $I\kappa$ B α , in response to cell stress, including that induced by cytotoxic agents, radiation or DNA damage, $I\kappa$ B α is phosphorylated, recognised, ubiquitinated and degraded by the 26S proteasome. As a response, NF- κ B is subsequently liberated and translocated into the nucleus whereby this transcription factor up-regulates cell proliferation and angiogenesis, as well as additionally protecting the cell from apoptosis. *In-vivo* experiments using the method described

in section 4.2.14 were performed with **2b** and **2h-j** inhibitors, to see the effect of these inhibitors in the NF- κ B pathway through the assessment of the degradation of I κ B α upon stimulation of this pathway with IL-1 growth factor. Cells were incubated with an inhibitor final concentration of 200 μ M for a period of 8 h and then stimulated with 15 ng of IL-1 for 20 min before harvesting (**Fig. 18**).

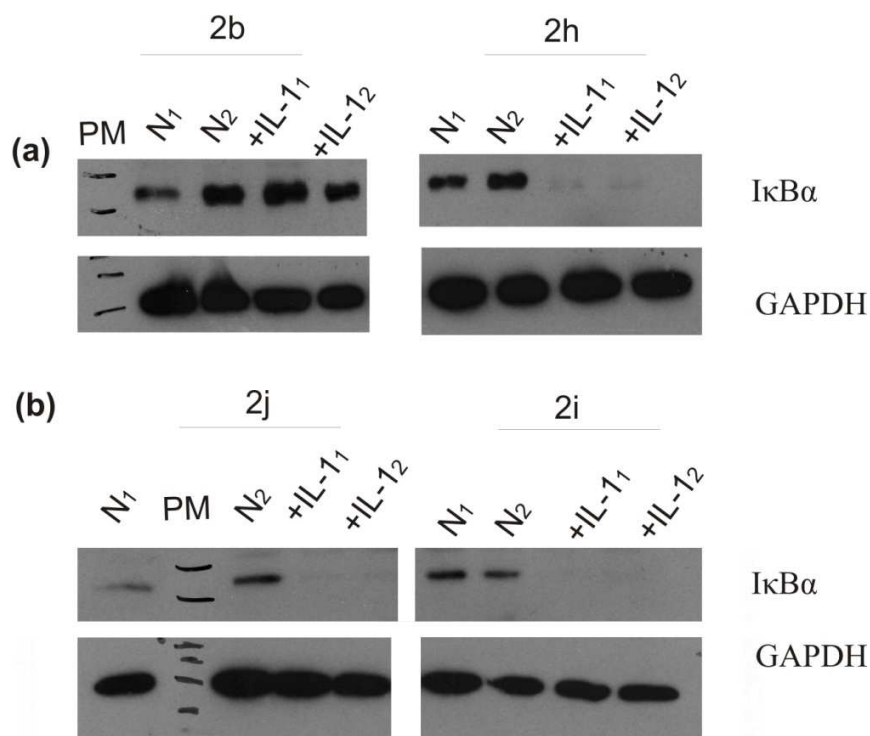


Fig. 18: In-vivo assay of TMC-95A bivalent derivatives

Westernblot analysis of I κ B α upon stimulation of this pathway with IL-1 growth factor and GAPDH housekeeping protein used to quantify amounts of protein loaded on the gels. HeLa cells were incubated with 200 μ M of (a) **2b** and **2h** (b) **2j** and **2i** for 8 h and then stimulated with 15 ng of IL-1 for 20min (Two repetitions were performed indicated here as +IL-1 and +IL-2). As a control two repetitions without IL-1 were also analysed described here as N1 and N2.

As illustrated in **Fig. 8**, cells which have been previously treated with inhibitor **2b** display accumulation of I κ B α upon stimulation of the NF- κ B pathway by addition of IL-1 into the media. Verification of the use of equimolar amounts of protein in the westernblot was performed using GAPDH as a house keeping protein. **Fig. 16** also shows that unlike **2b**, inhibitors **2h-2j** do not show any accumulation of I κ B α upon stimulation of this pathway. These results indicate

that **2h-2j** inhibitors do not disturb the NF- κ B pathway, which is most likely due to their long linkers preventing the entrance of these inhibitors in the cell. However, further investigation concerning the possibility of these inhibitors stimulating or inhibiting different cellular pathways altered by the 20S proteasome are yet to be performed.

5.2 Identification and Modification of a novel 20S proteasome inhibitor: the hydroxyureas

5.2.1 Identification and optimisation of the Hydroxyureas as 20S proteasome inhibitors

Synthesis and chemical characterisation of this section was performed by Philipp Beck and Christian Dubiella and can be found in the supplementary of the following paper (Gallastegui et al., 2012).

A screening using a chemical library from Bayer Crop Science Deutschland GmbH and the β 5 specific fluorogenic tetra-peptide substrates Z-LLY-AMC for the 20S proteasome was performed. The screening results carried out by Dr. Stephan Hillebrand, Bayer Crop Science Deutschland GmbH identified a known 5-lipoxygenase inhibitor (U.S. Pat. No. 5,714,633), **HU1**, as a possible proteasome inhibitor. **HU1** proved to be closely related to ZylfloCR[®] (Zileuton) a worldwide prescribed drug for the treatment of asthma, a fact that could be considered advantageous due to the previously performed clinical phase studies of this class of 5-lipoxygenase inhibitors. Hereby, this could present possible profitable initial characteristics, such as cell accessibility and druggability (Wenzel & Kamada, 1996).

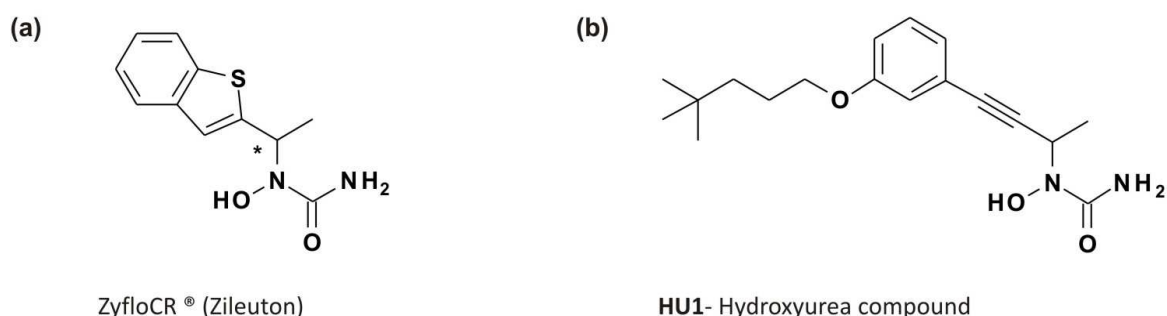


Fig. 19: Hydroxyurea compounds

Chemical structure of: (a) the prescriptive drug, Zileuton (b) the proteasome inhibitor hit from the high through put screening performed with a chemical library from Bayer Crop Science Deutschland GmbH, **HU1**.

The overall scaffold of **HU1** is composed of a hydroxyurea group which is linked to a meta-3,3-dimethylbutoxy-substituted propynyl-benzene moiety (**Fig. 19**). Thus far, these compounds have no chemical structural similarities to any proteasome inhibitor published so far. Furthermore, **HU1** does not possess either a peptide backbone or any known functionally reactive groups thus proposing a novel mode of action once bound to the CP. Subsequent characterisation of the subunit specificity of **HU1**, using purified yeast 20S proteasome and site specific substrates, yielded promising subunit specificity with inhibition only solely in the CT-like active site. Hereby an average of 17.0 % rest activity can be observed with a **HU1** concentration of 500 μM (**Fig. 20**). The IC_{50} of **HU1** against the CT-like activity was determined 230 μM ($K_i=23.1 \mu\text{M}$) (**Fig. 20**).

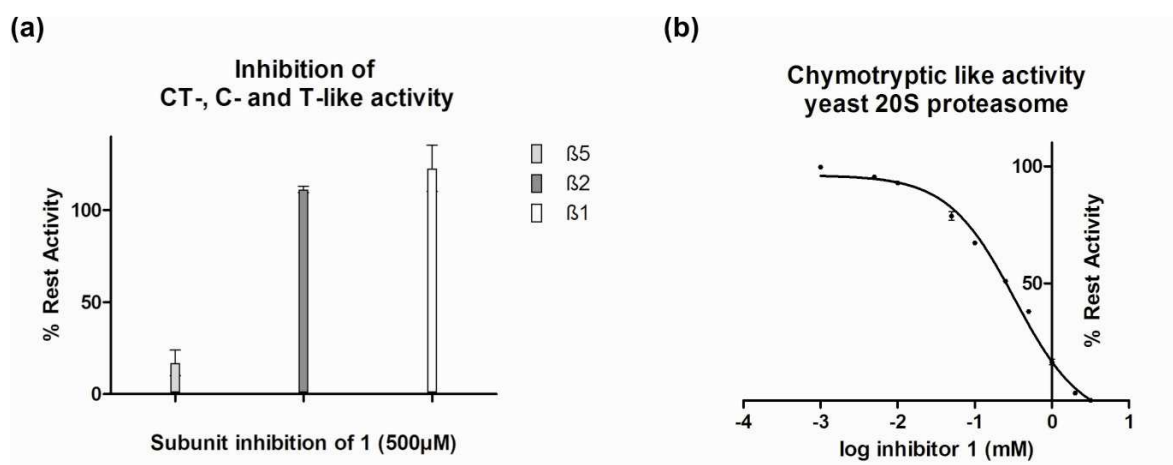


Fig. 20: In-vitro characterisation of HU1

(a) Remaining percentage of CT-, T- and C-like activity after treatment of the CP with 500 μM of **HU1**. **(b)** IC_{50} curve of **HU1** revealing an IC_{50} of 230 μM with $R^2=0.99$. Error bars \pm standard deviation (SD)

Nevertheless, these initial results were followed up by performing a structural evaluation of this inhibitor complexed with the yeast CP. A data set was collected at 2.4 \AA yielding a $R_{\text{free}} = 0.256$ (**Table 9**).

Data collection and refinements of CP:HU1					
<u>Crystal parameters</u>		<u>Data collection</u>		<u>Refinement (CNS)</u>	
Space group	P2 ₁	Beamline	X06SA, SLS	Resolution range (Å)	15-2.4
Cell constants (one molecule / AU ^a)	a=135.6 Å;	Wavelength (Å)	1.0	No. refl. working set	385701
	b=300.5 Å, c=144.6 Å; β=113.0 °				
		Resolution range (Å) ^b	30-2.4 (2.5-2.4)	No. refl. test set	20141
		No. observations	1445475	No. non hydrogen	49458
		No. unique reflections ^c	407507	Solvent water	1339
		Completeness (%) ^b	98.5 (98.0)	Inhibitor (non hydrogen)	44
		R _{merge} (%) ^{b, d}	8.3 (44.3)	R _{work} /R _{free} (%) ^e	23.9 / 25.6
		I/s (I) ^b	10.3 (2.9)	rmsd bond (Å) / (°) ^f	0.007 / 1.4
				Ramachandran Plot (%) ^g	96.2/3.2/ 0.6

Table 8 Data collection and refinement statistics HU-1

a-g according to **Table 3**.

The data set was processed and refined, yielding a 2F_o-F_c electron density map which clearly displayed **HU1** well defined in the proximity of the CT-like active site. Interestingly, **HU1** revealed a completely new mode of binding; i) the hydroxyurea moiety did not interact with the active site β5-Thr10^y nucleophile, as has been previously described for most proteasome inhibitors and ii) due to its lack of peptide backbone this inhibitor did not form the typical antiparallel β-sheet with the 20S yeast proteasome (**Fig. 21**). This structure proved to bind in a unique fashion occupying pockets that had been so far unexplored. The CP:**HU1** structure showed that it is the functional group which exhibits binding interactions analogous to the antiparallel β-sheets, observed normally both in substrates and peptidic inhibitors such as CAL I. Hereby, the hydroxyurea forms a series of hydrogen bonds with β5-Thr21NH/CO and β5-Gly47CO main chain atoms which usually play a key role in the antiparallel β-sheet formation. The methyl group located adjacent to the hydroxyurea moiety proved to hydrophobically interact with the β5 side chains Met45 and Ala46 and the propynyl-benzene group is directed towards a novel sub-pocket of the CT-like active site.

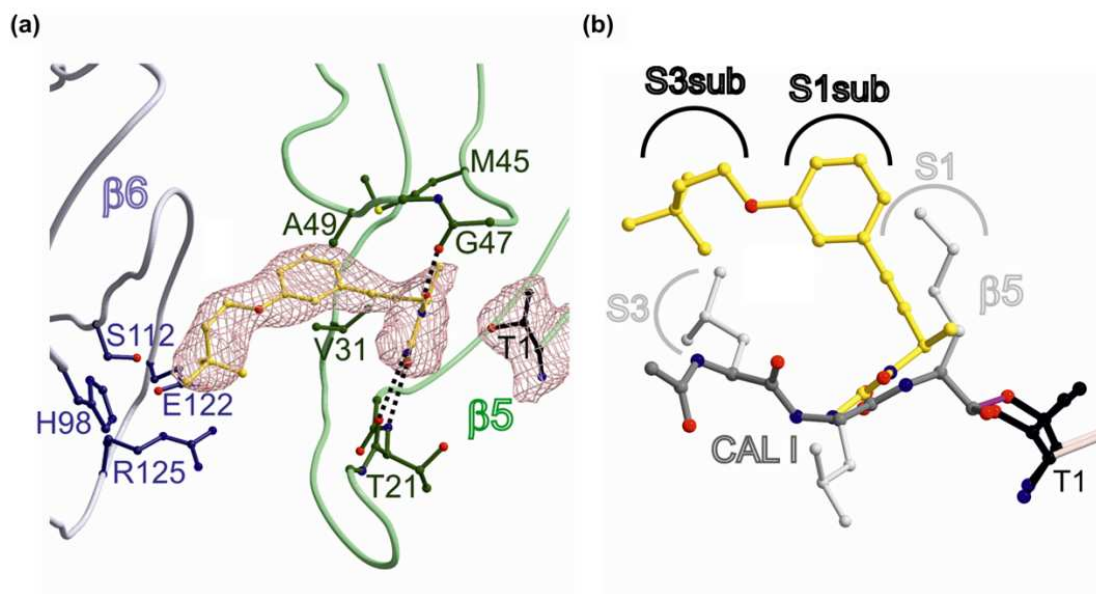


Fig. 21: Crystal structure of CP: HU1

(a) The hydroxyurea group forms a network of H-bonds to $\beta 5$ -Thr21NH/CO and $\beta 5$ -Gly47CO (black dashed lines). Residues forming the *S1-subpocket* are highlighted in green and embrace the rigid propynyl-benzene scaffold, whereas *S3-subpocket* coloured in blue, interact with the long aliphatic chain, 3,3-methylbutoxy. (b) Superposition of CAL-I and HU1, showing the complete new mode of action of HU1 and the novel *sub*-pockets, observed in the crystallographic results.

The first novel specificity pocket was termed *S1-subpocket*, due to its proximity to *S1*-pocket, and it is formed by Ser27, Val31 Met45 and Ala49. Thus, the propyl-benzene group not only performs a multitude of Van-der-Waals interactions with the newly discovered *S1-subpocket* but additionally, through its rigid structure, reduces the entropic penalty upon binding of this inhibitor to the CP. In addition, the long aliphatic 3,3-methylbutoxy side chain protrudes to yet another new *sub*-pocket, termed *S3-subpocket* which is formed by His98, Ser112, Glu112, and Arg125, with all of these residues are located in subunit $\beta 6$ (Fig. 22).

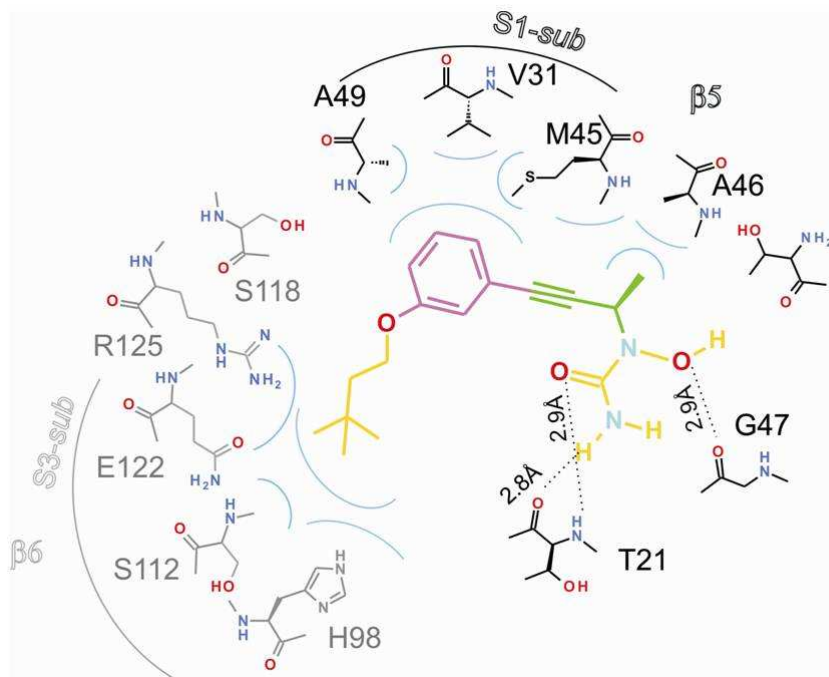


Fig. 22: Schematic overview of CP: HU1

The distinct specificity pockets *S1-sub* and *S3-sub* pockets of the CL-substrate binding channel and their corresponding amino acids are depicted in black and grey, respectively. Black dashes indicate hydrogen bonds and are shown with their corresponding distances, which clearly indicate the hydrogen bond mesh between Gly47, Thr21, and the hydroxyurea moiety. Hydrophobic interactions are depicted with blue lines, showing the interactions that lead to the positioning of the propyl-benzene and 3,3-methylbutoxy groups.

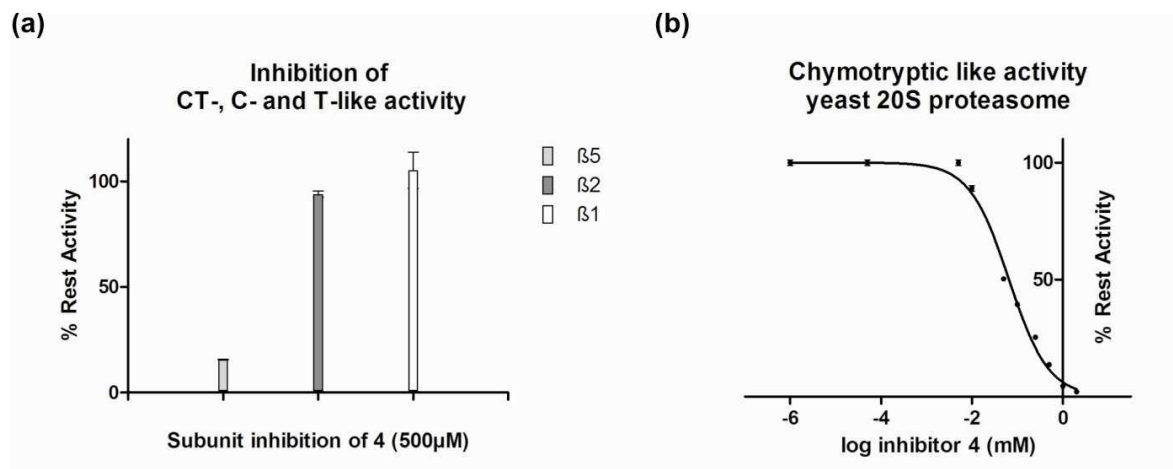
Subsequent optimisation of **HU1** was performed through maintenance of its original propynyl-hydroxyurea-scaffold and optimisation of two obvious side chains; the 3,3-methylbutoxy groups (here on termed the R^1 side chain), and the methyl group encountered straight after the hydroxyurea head group (here on termed the R^2 side chain). It became apparent that the R^1 moiety has a significant effect on CP:**HU** binding as the replacement of the meta-substituent by a hydrogen atom in R^1 (**HU0**) showed no inhibition of the CP. Furthermore, slight changes in R^1 significantly influenced the IC_{50} of these **HU** compounds reiterating previous findings on the decarboxylated peptides.

Compound	R ¹	R ² (C* config.)	IC ₅₀ (μM)
HU0	-	Me (R/S)	No inh
HU2	dibenzofuran	Me (R/S)	>1mM
HU3	pentane	Me(R/S)	>1mM

Table 9 HU1 derivatives

Table showing the **HU** derivatives; **HU0**, **HU2**, and **HU3**, with their corresponding IC₅₀ values and the chemical structure of the **HU** scaffold with the position of R¹ and R² as well as its chiral centre.

Small halogenated and extended aliphatic R¹ side chains resulted in at least 5-fold increase in the IC₅₀ (> 1 mM) compared to **HU1**, as shown for the trifluoromethoxy and n-pentoxy R²-derivatives (**HU2** and **HU3**, respectively) (**Table 9**). Interestingly, a tert-butyl-dimethyl-siloxy moiety in position R¹ (**HU4**) significantly improved the inhibitors affinity to the CT-like active site and resulted in a 5-fold decrease in the IC₅₀ (48 μM, K_i=4.8 μM).

**Fig. 23: In-vitro characterisation of HU4**

(a) Remaining percentage of CT-, T- and C-like activity after treatment of the 20S yeast proteasome with 500 μM of **HU4**. (b) IC₅₀ curve of **HU4** revealing 48 μM with R²= 0.99. Error bars ± SD

Following these promising results yeast CP crystals were soaked with **HU4** and a full data set was collected at 3.2 Å with an R_{free} = 0.228 (**Table 10**).

Data collection and refinements of CP:HU4					
<u>Crystal parameters</u>		<u>Data collection</u>		<u>Refinement (CNS)</u>	
Space group	P2 ₁	Beamline	X06SA, SLS	Resolution range (Å)	15-3.2
Cell constants (one molecule / AU ^a)	a=135.0 Å; b=300.9 Å, c=144.4 Å; β=112.7 °	Wavelength (Å)	1.0	No. refl. working set	163521
		Resolution range (Å) ^b	30-3.2 (3.3-3.2)	No. refl. test set	8624
		No. observations	418904	No. non hydrogen	49458
		No. unique reflections ^c	178396	Solvent water	1339
		Completeness (%) ^b	98.3 (96.1)	Inhibitor (non hydrogen)	46
		R _{merge} (%) ^{b, d}	14.4 (53.7)	R _{work} /R _{free} (%) ^e	20.2 / 22.8
		I/s (I) ^b	7.0 (2.1)	rmsd bond (Å) / (°) ^f	0.007 / 1.3
				Ramachandran Plot (%) ^g	93.8/5.8/0.6

Table 10 Data collection and refinement statistics HU-4

a-g according to **Table 3**.

The crystal structure of **HU4** in complex with the CP showed only a slight movement of the original propynyl-hydroxyurea-scaffold position; however, it illustrated the tight interactions of the tert-butyl-dimethyl-siloxy side chain within the S3-subpocket (**Fig. 22**). Therefore results revealed the importance of a more bulky group in this position.

Based on these crystallographic results, molecular modelling was performed by Marcelino Arciniega, to design more appropriate side chains for R¹. An adamantyloxy group in R¹ was identified to give the highest docking scores (-10.7 in GlideScore scale) among a small derivative library of 50 compounds (**Fig. 22**). It is well known that this docking procedure is highly efficient in discriminating compounds with low activity from those with high affinities for the CT-like binding site, however, some discrepancies may be observed as only the (*R*)-conformers were taken into account when performing molecular modelling (**Fig. 31**).

The hydroxyurea compounds were further derivatised by adding an adamantyloxy group R^1 , **HU8**, and subsequently analysed through enzymatic experiments.

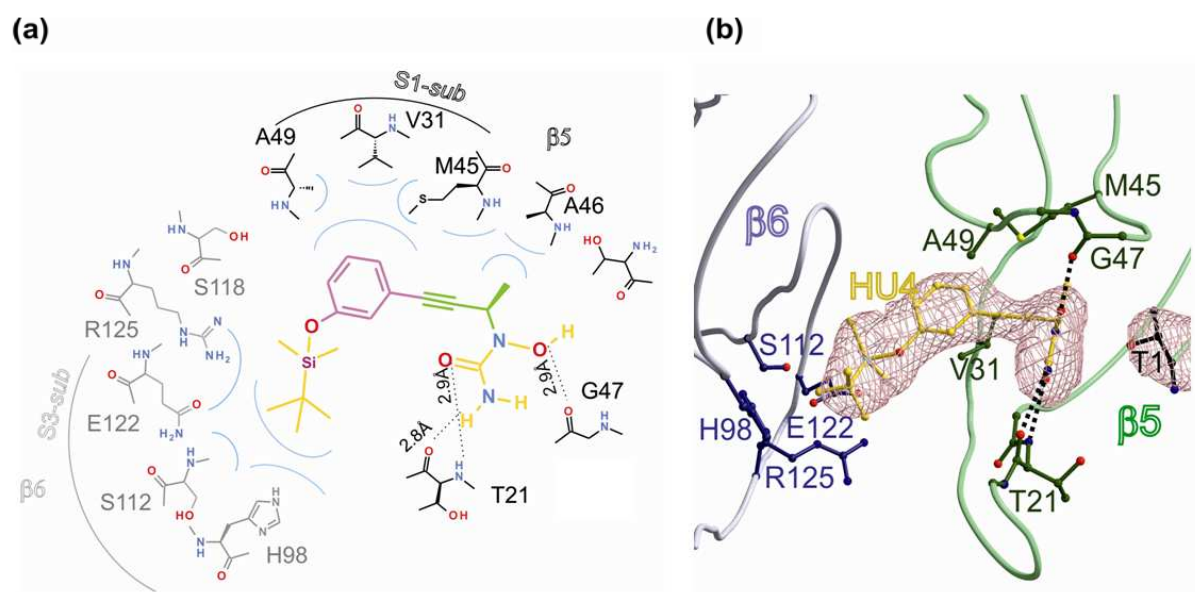


Fig. 24: Crystal complex structure of CP: HU4

(a) Schematic overview of HU4 bound to the CT-active site of the CP. **(b)** Omit electron density of HU4 bound to the CP, revealing concerted movements of the rigid propynyl-benzene scaffold, the hydroxyurea group forms a network of H-bonds to $\beta 5$ -Thr21NH/CO and $\beta 5$ -Gly47CO (black dashed lines). Residues forming the S1-subpocket are highlighted in green; residues forming the S3-subpocket, which predominantly interact with the bulkier tert-butyl-dimethyl-siloxy moiety, are coloured in blue.

Interestingly, **HU8**, improved the inhibitors affinity to the CT-like active site significantly resulting in a 320-fold decrease in the IC_{50} in comparison to that of **HU1**. (IC_{50} of 780 nM, $K_i=78$ nM) (**Fig. 25**). Additionally, a reversibility activity assay confirmed reversible binding of the ligand, a result that is in agreement to the previous crystallographic results from **HUs**. An increase in fluorescence was observed when the tetra-peptide substrate Z-LLY-AMC was added even after 15min incubation with 200 μ M of **HU8** (**Fig. 26**).

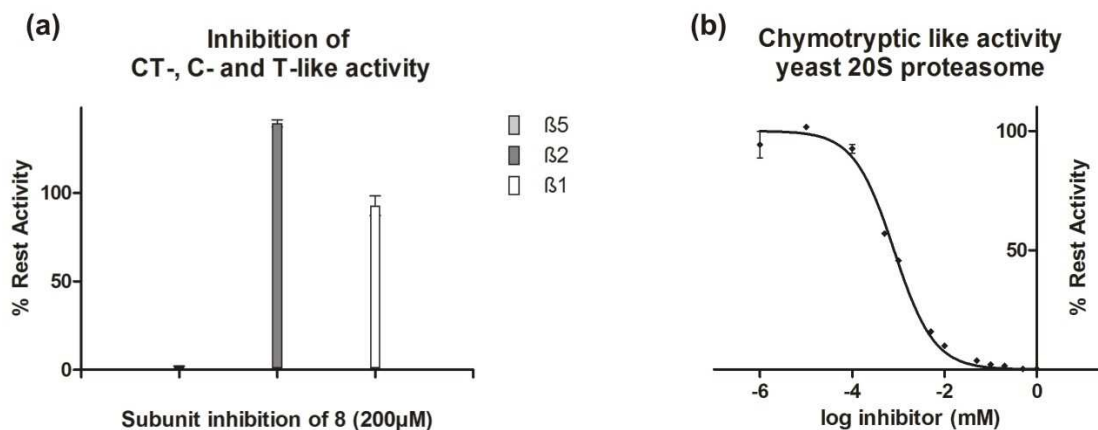


Fig. 25: In-vitro characterisation of HU4

(a) Remaining percentage of CT-, T- and C-like activity after treatment of the yeast CP with 200 μM of **HU8** (b) IC_{50} curve of **HU8** revealing an IC_{50} of 700 nM with $R^2 = 0.99$. Error bars \pm SD.

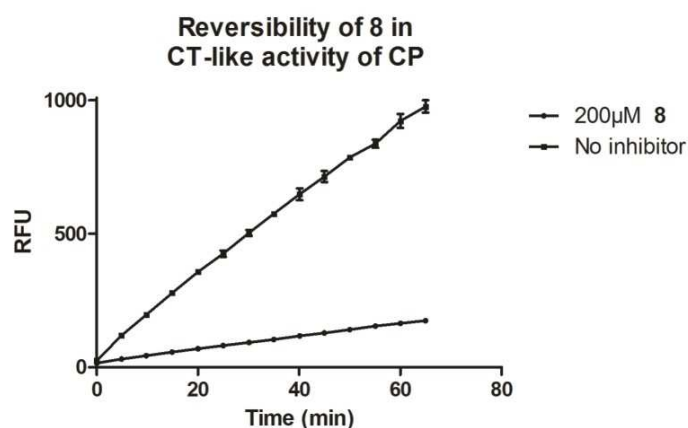


Fig. 26: Reversibility of HU8

Time resolved CT-like activity measurement after 15 min pre-incubation of 200 μM **HU8**, proving reversible binding of **HU8** to the proteolytic active site Error bars \pm SD.

These results were followed by a crystallographic analysis of **HU8** in complex with yeast CP, whereby a 2.9 Å data set was obtained yielding $R_{\text{free}} = 0.238$ (Table 12).

Data collection and refinements of CP:HU8					
<u>Crystal parameters</u>		<u>Data collection</u>		<u>Refinement (CNS)</u>	
Space group	P2 ₁	Beamline	X06SA, SLS	Resolution range (Å)	15-2.9
Cell constants (one molecule / AU ^a)	a=133.7 Å; b=298.2 Å, c=149.6 Å; β=113.1 °	Wavelength (Å)	1.0	No. refl. working set	192177
		Resolution range (Å) ^b	30-2.9 (3.0-2.9)	No. refl. test set	10063
		No. observations	796092	No. non hydrogen	49548
		No. unique reflections ^c	225034	Solvent water	852
		Completeness (%) ^b	99.9 (99.7)	Inhibitor (non hydrogen)	52
		R _{merge} (%) ^{b, d}	10.4 (61.3)	R _{work} /R _{free} (%) ^e	21.0 / 23.8
		I/s (I) ^b	9.1 (2.3)	rmsd bond (Å) / (°) ^f	0.007 / 1.4
				Ramachandran Plot (%) ^g	93.7/5.8/0.5

Table 11 Data collection and refinement statistics HU-8

a-g according to **Table 3**.

The crystal structure confirmed the initial modelling results with a 0.8 Å RMSD between experimental and the modelled ligand structure. Furthermore, the crystal structure of CP:HU8 additionally revealed the importance of Ser118 in this *sub*-pocket which forms a strong hydrogen bond to the ethereal oxygen of HU8 further stabilising the adamantyloxy group (**Fig. 26**). Further optimisation was performed to HU8 through the study of different derivatives of the R² side chain. Total removal of R² side chain, yielding HU5, increased the IC₅₀ by approximately 17-fold to an IC₅₀ of 12 μM (K_i=1.2 μM) (compared to HU8). Additionally, an introduction of sterically more demanding side chains in R², such as ethyl (HU6) or isopropyl (HU7), increased the IC₅₀ by 15-fold, that resulted in an IC₅₀ of 1 μM and 10 μM respectively (K_i=0.11 and 1.1 μM respectively), thus indicating that the Me group in R² is the optimal moiety at this position.

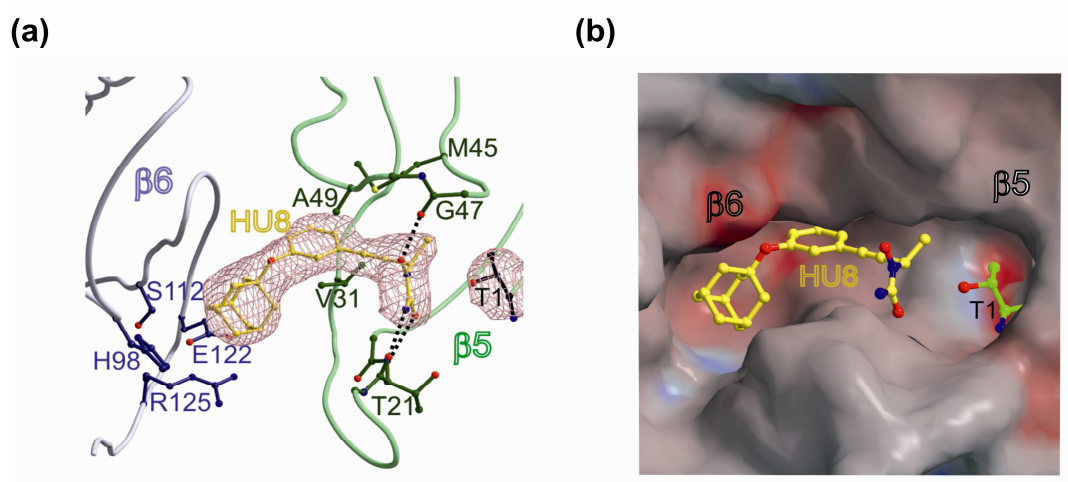


Fig. 27: Complex structure of CP: HU8

Crystal structure of CP:HU8. **(a)** The hydroxyurea group forms a network of H-bonds to $\beta 5$ -Thr21NH/CO and $\beta 5$ -Gly47CO (black dashed lines). Residues forming the S1-subpocket are highlighted in dark green and embrace the rigid propynyl-benzene scaffold, whereas S3-subpocket coloured in blue, interact with the long aliphatic chain, 3,3-methylbutoxy, **(b)** surface representation of HU8 bound to the CT-like-active site.

These enzymatic data are in agreement with experimental crystallographic and modelling predictions (**Fig. 31**) which clearly indicated a clash of larger moieties with the peptide backbone of $\beta 5$ -subunit and the importance of small hydrophobic R² groups for stabilisation of the ligand with the protein backbone.

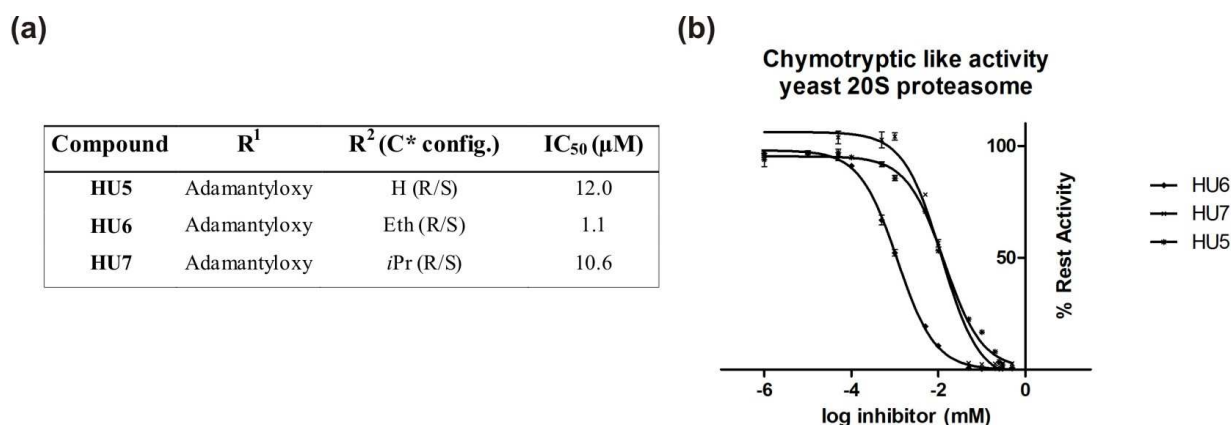


Fig. 28: In-vitro of compound HU5-7

(a) Table indicating the different R1 and R2 groups and the IC₅₀ obtained. **(b)** IC₅₀ curves. Error bars \pm SD.

Further optimisation of these **HU** compounds was conducted in respect to the stereochemistry of the R² group. Soaking proteasome crystals with a racemic mixture of all **HU** compounds yielded solely the (*R*)-conformer indicating a strong enantiomeric selectivity. Thus, both enantiomers of **HU8**, the (*S*)-conformer **HU9** and the (*R*)-conformer **HU10** were characterised *in-vitro*. Unlike **HU10** that revealed an IC₅₀ of 300 nM (K_i=30 nM), more than a 2-fold decrease compared to the racemic mixture (**HU8**), **HU9** yielded approximately an 80-fold increase in IC₅₀ thus yielding an IC₅₀ of 56 μM (K_i=5.8 μM). Crystallographic analysis of both compounds HU9-10 was therefore performed. Complex structures **HU9** and **HU10** with yeast CP were obtained whereby data set were collected at 3.1 Å (R_{free} = 0.231) and 2.8 Å (R_{free} = 0.262) respectively (**Table 12**).

Data collection and refinements of CP:HU9					
<u>Crystal parameters</u>		<u>Data collection</u>		<u>Refinement (CNS)</u>	
Space group	P2 ₁	Beamline	X06SA, SLS	Resolution range (Å)	15.03.200 0
Cell constants (one molecule / AU ^a)	a=137.4Å; b=300.8 Å, c=145.2 Å; β=113.4 °	Wavelength (Å)	1	No. refl. working set	183286
			30.03.2001	No. refl. test set	9619
		Resolution range (Å) ^b	(3.2-3.1)	No. non hydrogen	49548
		No. observations	712277	Solvent water	1025
		No. unique reflections ^c	194601	Inhibitor (non hydrogen)	76
		Completeness (%) ^b	99.7 (99.8)	R _{work} /R _{free} (%) ^e	19.8 / 23.1
		R _{merge} (%) ^{b, d}	16.1 (63.3)	rmsd bond (Å) / (°) ^f	0.007 / 1.3
		I/s (I) ^b	9.3 (2.3)	Ramachandran Plot (%) ^g	94.2/5.4/ 0.4

Data collection and refinements of CP:HU9					
<u>Crystal parameters</u>		<u>Crystal parameters</u>		<u>Crystal parameters</u>	
Space group	P2 ₁	Beamline	X06SA, SLS	Resolution range (Å)	15.02.2008
Cell constants (one molecule / AU ^a)	a=134.1 Å; b=300.6 Å, c=144.1 Å; β=112.8 °	Wavelength (Å)	1	No. refl. working set	223049
		Resolution range (Å) ^b	30-2.8 (2.9-2.8)	No. refl. test set	11684
		No. observations	639098	No. non hydrogen	49548
		No. unique reflections ^c	236186	Solvent water	1281
		Completeness (%) ^b	91.7 (90.2)	Inhibitor (non hydrogen)	76
		R _{merge} (%) ^{b, d}	8.9 (50.8)	R _{work} /R _{free} (%) ^e	23.4 / 26.2
		I/s (I) ^b	9.4 (2.0)	rmsd bond (Å) / (°) ^f	0.007 / 1.3
				Ramachandran Plot (%) ^g	93.8/5.7/0.5

Table 12 Data collection and refinement statistics of HU9 and HU10 a-g according to Table 3.

The structural results of CP:HU9 showed that only the orientation of R² in the (*S*)-conformer is responsible for this decrease in binding affinity, most likely due to disfavoured interactions with protein main chain atoms and its methyl group. Furthermore, structural superposition of HU9 and HU10 revealed that both (*R*)- and the less active (*S*)-conformer aligned almost identically regarding the hydroxyurea moiety and the adamantyloxybenzene. Therefore considering the non-covalent binding mode of these compounds, this observation underlines both the strength of other binding motifs, which still keep the inhibitor in place despite the disfavoured orientation of the Me group in R², and the importance of its orientation. Optimisation of HU1 to HU10 showed the strength of the combination of crystallographic analysis, molecular modelling, chemical synthesis and kinetics.

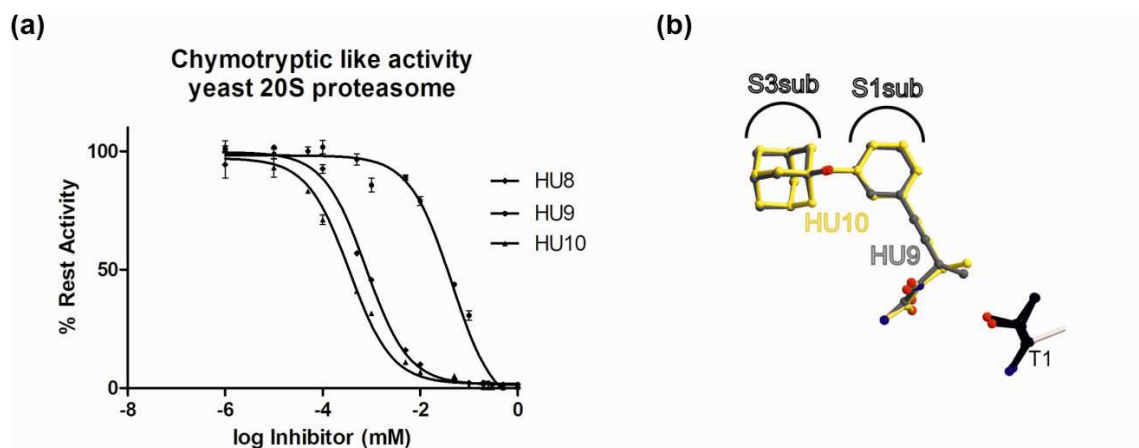


Fig. 29: Compound HU9 and HU10

(a) IC₅₀ curve revealing 700 nM for **HU8**, 56 μM for **HU9** and 300 nM for **HU10** with $R^2 = 0.99$ for all three compounds. (b) The structure superposition of **HU9** and **HU10** reveals identical positioning of the hydroxyurea and the adamantyloxybenzene moiety except the methyl group in R^2 . Error bars \pm SD.

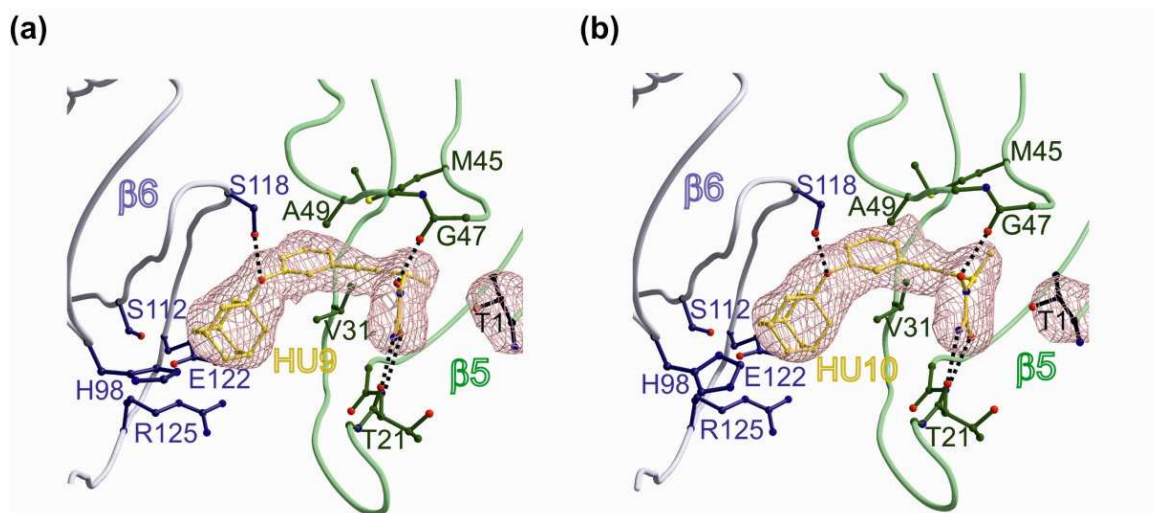


Fig. 30: Complex structure of CP: HU9-10

Crystal structure of yeast CP complexed with (a) **HU9** (b) **HU10**. The CT- active site is depicted in green and blue colour for $\beta 5$ and $\beta 6$ respectively. The inhibitors are shown in stick form and coloured in yellow with their original electron density map.

Furthermore, due to the unique reversible mode of action of this set of inhibitors, **HU10** can be considered both a drug like compound and a suitable fragment for CP inhibitor development. In addition, the crystallographic results revealed a MES molecule derived from

the crystallization buffer. This MES molecule as described for the TMC-95A derivatives can be further utilised as fragment in rational drug design for improved proteasomal inhibition.

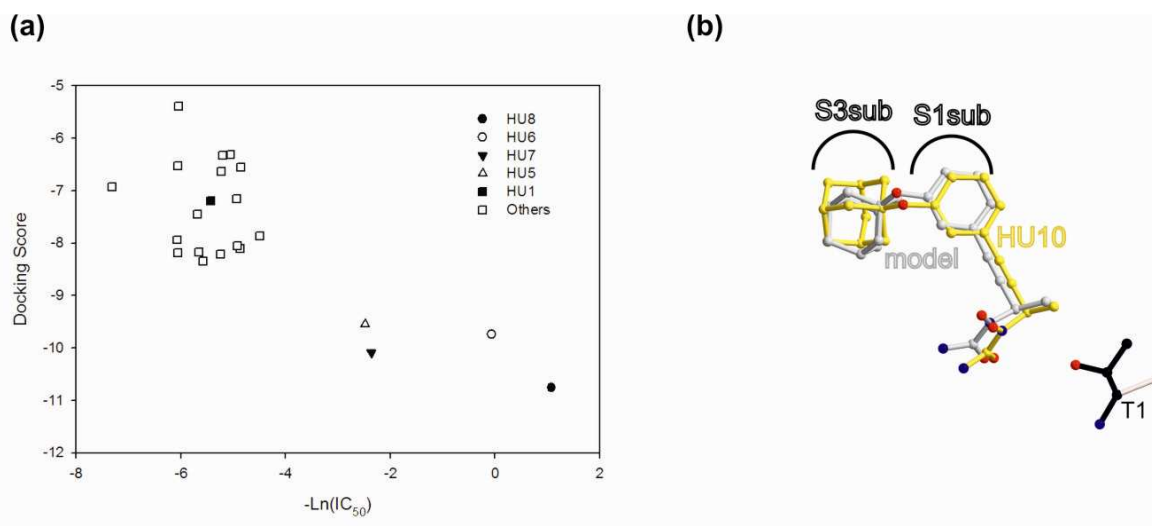


Fig. 31: Molecular modelling with HU

Molecular modelling predictions (performed by Marcelino Arciniega) compared to experimental IC_{50} data: **(a)** Graph demonstrating the correlation between the experimental IC_{50} (μM) in a logarithmic scale and the predicted binding affinity as docking scores (GlideScore scale), **(b)** Superposition of modelled **HU10** compared to the experimental data of CP:**HU10** crystal structure.

As observed in the crystal structures of the CP with the decarboxylated peptides, the MES molecule interacts with $\beta 5\text{-Gly}47\text{N}$ and occupies the oxyanion hole (**Fig. 32**). As described for the TMC-95A derivatives, *in-vitro* studies performed with both MES and TRIS buffers did not show any effect in these compounds' affinities towards the yeast CP and therefore is required to be covalently bridged in order to produce a detectable effect. Thus, it presents an interesting option for further fragment based drug design opening a new window into the possible moieties that can be used for the occupation of the oxyanion whole.

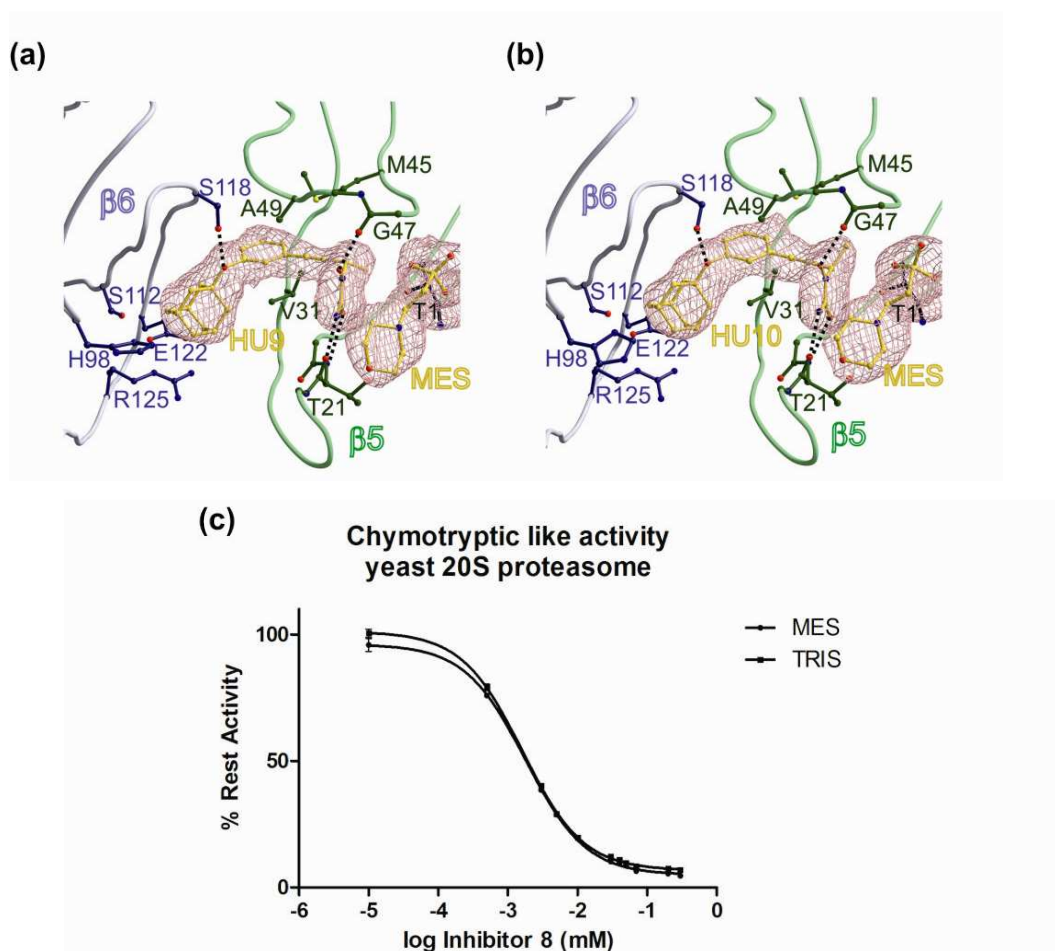


Fig. 32: Effect of MES molecule in HU binding

(a) Crystal structure of CP:HU9 showing the location of the additional MES molecule. The CT- active site is depicted in green and blue colour for $\beta 5$ and $\beta 6$ respectively. The inhibitors are shown in stick form and coloured in yellow with their original electron density map. (b) Crystal structure of CP:HU10 showing the location of the additional MES molecule. (c) IC_{50} of compound HU8 with MES and TRIS as assay buffers. Error bars \pm SD.

5.2.2 Differences between Human and Yeast 20S proteasome inhibition

Comparison of the primary sequences between yeast and human (using the program LALIGN), found a sequence identity of 66.8 % in $\beta 5$ and 27.6 % in $\beta 6$. In order to further optimise the hydroxyureas, differences between the amino acids found in the active sites of the CP of these two organisms were taken into account and *in-vitro* analysis using human constitutive CP was performed. Interestingly HU8-10 demonstrated significant differences in

their respective IC_{50} . As shown in **Fig. 32** all IC_{50} of these compounds increased when tested against human constitutive proteasome (ENZO life science, Germany). **HU8** resulted in an IC_{50} of 64 μM , approximately 90 times higher, and both **HU9** and **HU10** revealed a similar enhancement with an IC_{50} of 360 μM and 70 μM , respectively. Superposition of **HU10** into the bovine constitutive CP, an organism that has 95.8% sequence identity with human in $\beta 5$ and 98.0% in $\beta 6$, led to a plausible explanation.

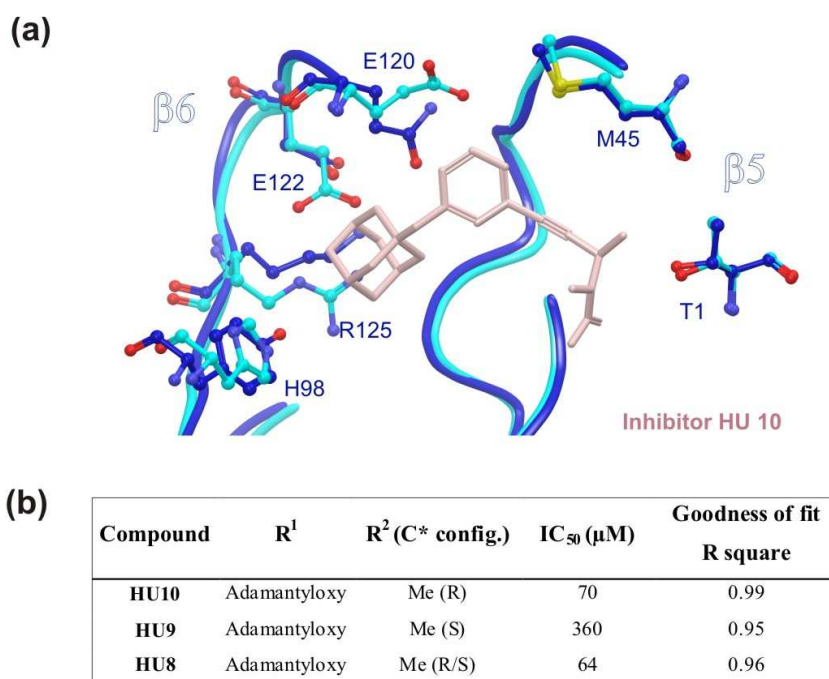


Fig. 33: Human 20S proteasome and HU8-10

(a) Structural superposition of **HU10** in $\beta 5$ of the CP from *S. cerevisiae* and *B. taurus*. The CT- active site is depicted in light and dark blue colour for bovine and yeast CP respectively. The inhibitors are shown in stick form and coloured in yellow with their original electron density map. (b) IC_{50} of **HU8-10** with human constitutive CP.

The S3-subpocket of the CT-like active site of bovine 20S proteasome was found to possess a more spacious binding site, whereby crucial amino acids involved in the stabilisation of the adamantyloxy moiety such as Glu120, Glu122, Arg125 and His98 are changed to Gln120, Asp122, Lys125 and Try98, respectively. These changes lead to a more spacious pocket with a lower affinity for the adamantyl. However, the demand of a complex structure of these

inhibitor type with constitutive and possibly the immuno 20S proteasome, a prerequisite for further optimisation of hydroxyurea compounds in order to direct its affinity to defined proteasome types and organisms, a currently ongoing work.

5.2.3 Cell accessibility assays

As described for the TMC-95A derivatives, *in-vivo* experiments were performed for cell accessibility of HU-compound by using the I κ B α degradation assay. Cells were exposed to a final concentration of 200 μ M of **HU10** for 6 hours before IL-1 induction was carried out, followed by westernblot analysis against I κ B α . Despite observed cell detachment, the westernblot analysis indicated that there was no I κ B α accumulation detected.

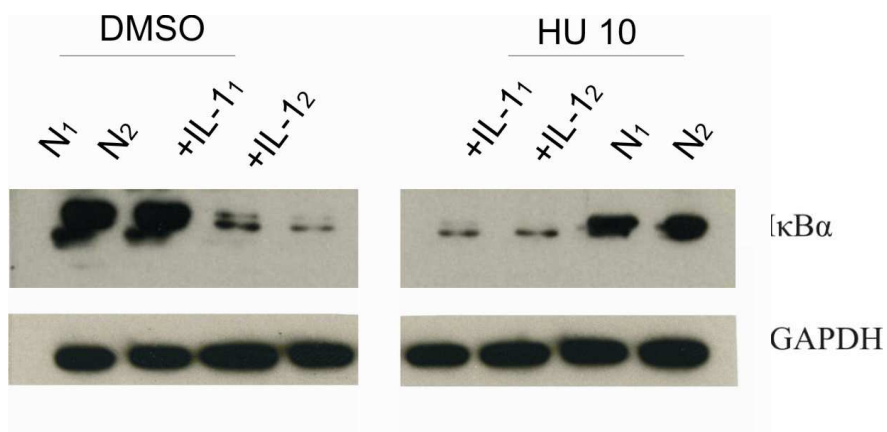


Fig. 34: *In-vivo* analysis of HU10

Westernblot of I κ B α from HeLa cells exposed with 200 μ M **HU10** for 6h showing normal degradation of I κ B α . Two repetitions were performed with IL-1 addition (+IL-1 and +IL-2) and as a control two repetitions without IL-1 (N1 and N2).

These results clearly show that even through the addition of MG132 does increase I κ B α cellular content, addition of **HU10** showed normal I κ B α degradation. Further experiments performed in a together in collaboration with Dr. Henry Zall, (Technische Universität München, Department of immunology), proved through Fluorescence Activated Cell Sorting (FACS) analysis that our inhibitor produced high propidium iodide uptake in HeLa cells with a low activation of caspase 3; thus demonstrating that cell death was completely unspecific and did

not occur through controlled apoptosis. However, to prove that cell detachment of **HU10** was not due to a simple detergent effect caused by the hydrophobic adamantyloxy moiety and the highly hydrophilic hydroxyurea moiety an additional derivative was synthesised. **HU12**, containing an additional OH group attached to the adamantyl was synthesised in anticipation to an increase in its solubility in aqueous solutions and an avoidance of a plausible detergent effect on the HeLa cells.

In vitro analysis of **HU12** yielded an IC₅₀ of 11 µM, an approximate 36 time decrease in potency compared to **HU10**. Nevertheless, a crystallographic analysis of **HU12** in complex with yeast CP was elucidated at 2.9 Å ($R_{\text{free}} = 0.245$) (**Table 13**).

Data collection and refinements of CP:HU12					
<u>Crystal parameters</u>		<u>Data collection</u>		<u>Refinement (CNS)</u>	
Space group	P2 ₁	Beamline	SLS, PX06SA	Resolution range (Å)	15-2.9
Cell constants (one molecule / AU ^a)	a=134.3 Å; b=300.5 Å, c=144.1 Å; β=112.8 °	Wavelength (Å)	1.0	No. refl. working set	195879
		Resolution range (Å) ^b	10-2.9 (3.0-2.9)	No. refl. test set	10266
		No. observations	800653	No. non hydrogen	49650
		No. unique reflections ^c	229665	Solvent water	1342
		Completeness (%) ^b	98.9 (96.3)	Inhibitor (non hydrogen)	54
		R _{merge} (%) ^{b, d}	11.2 (65.5)	R _{work} /R _{free} (%) ^e	21.0/24.5
		I/s (I) ^b	9.93 (1.52)	rmsd bond (Å) / (°) ^f	0.0120/1.621 5849 (92.7 %)
				Ramachandran Plot (%) ^g	396 (6.3 %) 67 (1.1%)

Table 13 Data collection and refinement statistics HU12

a-g according to **Table 3**.

The crystal structure of CP:**HU12** displayed the introduced OH group in the adamantyl side chain forming hydrogen bonds with His98 and Glu122 of subunit β6. Additionally, two MES

molecules were observed in the structure in the vicinity of **HU12**, forming a hydrogen bonding network with Gly127 and His98. However, the interesting decrease in potency could only be explained by the increase in size of the adamantyl moiety compared to **HU10** (Fig. 35). *In-vivo* experiments using the established NF- κ B assay were performed, however resulting in normal I κ B α degradation even after a 12 h exposure at 1 mM **HU12** concentration (Fig. 35).

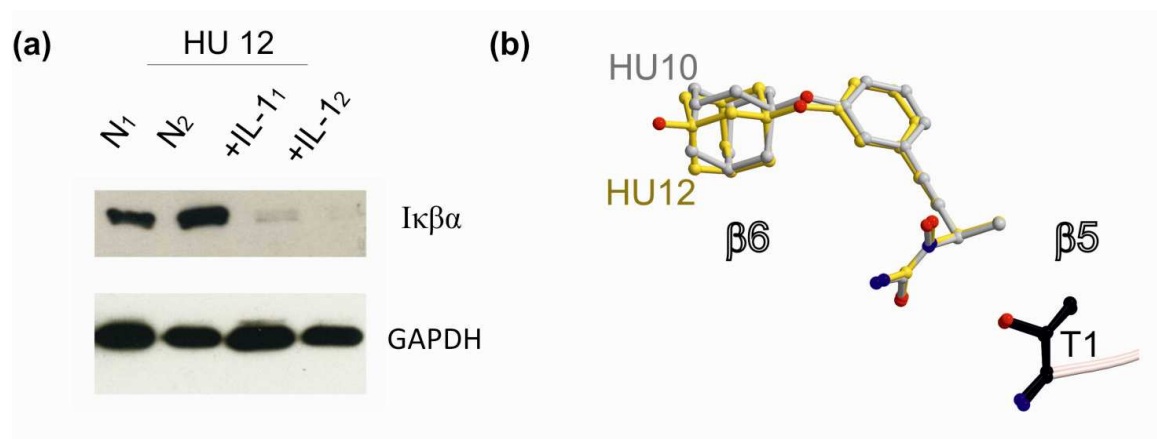


Fig. 35: *In-vivo* analysis of HU12

(a) Westernblot of I κ B α from HeLa cells exposed to 200 μ M **HU12** for 6 hours showing normal degradation of I κ B α . (b) structural superposition of the CP:**HU10** and CP:**HU12** crystal structure. Two repetitions were performed with IL-1 addition (+IL-1 and +IL-2) and as a control two repetitions without IL-1 (N1 and N2).

5.2.4 Hydroxyurea compounds and 5-lipoxygenase

Owing to the closely related chemical structure of the **HUs** to ZyfloCR[®], a class of 5-lipoxygenase (5-LOX) inhibitors, a 5-LOX assay was performed in order to further characterise this inhibitor. 5-LOX is a member of the lipoxygenase family and is involved in formation of leukotrienes through catalysing the oxidation set of arachidonic acid into hydroperoxyeicosatetraenoic acid (Dixon et al., 1990). A 5-LOX assay was performed with **HU0**, known lipoxygenase inhibitor and our hydroxyurea **HU8** using human 5-LOX. Interestingly, **HU8** showed a high affinity for 5-LOX leading to a 976 nM (**HU0**) and 595 nM (**HU8**) IC₅₀ respectively

(Fig. 35) However, collective inhibition of the 20S proteasome and 5-lipoxygenase has not been yet characterised *in-vivo* to verify if this may lead to a beneficial synergistic effect. A possibility due to the role of 5-LOX in some inflammatory problems or even some types of cancer. Therefore, the complex structure of these inhibitors with 5-LOX is essential. Recently the crystal structure of 5-LOX has been determined (Gilbert et al., 2011), thus complex structures of HUs with 5-LOX are now achievable and open a therapeutical window towards the understanding of possible drugs synergistic effects between the proteasome and 5-LOX.

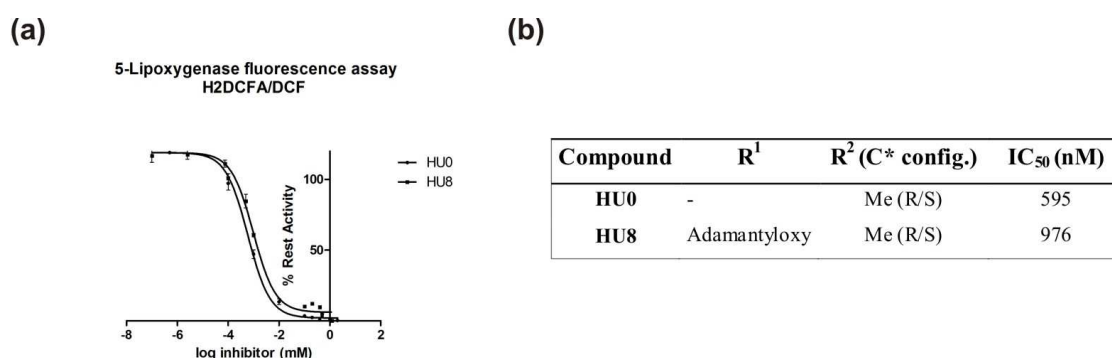


Fig. 36: *In-vitro* characterisation of 5-LOX of both HU0 and HU8

(a) IC₅₀ curves against 5-LOX. (b) Table showing IC₅₀ of 5-LOX and R₁ and R₂ moieties of HU compounds. Error bars ± SD.

In conclusion, the class of hydroxyurea-derivatives currently represent the smallest, reversible, non-covalently bound and active site specific inhibitors observed to date for the CP. Therefore these compounds present an interesting option for further fragment based drug design of proteasome inhibition by exploiting a previously unobserved mode of action once bound to the proteasome.

5.2.5 Structural characterisation of site specific epoxyketone and vinyl sulfone based inhibitors for the 20S proteasome

Synthesis and chemical characterisation of this section was performed by the group of Prof. Overkleeft (Faculty of Science, Leiden Institute of Chemistry, Holland) and *in-vivo* assays were performed by Prof. Kisselev's group (Pharmacology & Toxicology, Dartmouth Medical School, USA). The chemical characterisation of these ligands can be found in the following papers (Mirabella et al., 2011) and (van der Linden et al.).

Even though the 20S proteasome contains 3 different active sites, the CT-like activity has long been considered the only suitable targets for antineoplastic drugs. However, the recent work published by our collaborators Prof. Overkleeft and Prof. Kisselev indicate the importance of T-like sites as co-targets for anticancer drugs. These results reiterate the significance of site specific inhibitors of the 20S proteasome, not only for their commercial use, but also for enhancing the understanding of the CP's proteolytic mechanism. Thus, structural and *in-vitro* characterisation of CT- and T- like specific inhibitors in complex with the yeast 20S proteasome was performed in order to ascertain a possible explanation for the higher subunit specificity found in yeast and human constitutive 20S proteasome.

5.2.6 CT-like active site specific epoxyketone based inhibitors

Inactivation of the CT-like active site causes severe retardation of growth, increase in stress sensitivity and accumulation of proteasome substrates. Thus, it can be expected that $\beta 5$ plays a pivotal role in protein breakdown by the proteasome. Furthermore, the S1 hydrophobic pocket makes this subunit a suitable target for hydrophobic peptides in P1 which are well known for their cell accessibility, making this active site a promising target for drug development. Our collaborators have synthesised common peptide based inhibitors with high affinity to CT-like active site, such as **E-3c (Fig. 37)**. Furthermore, the additionally synthesised peptide combined with the ureido structural element present in a potent type of inhibitor, the

syringolins. Hereby, yielding a focused library of potent new ureido containing epoxyketone proteasome inhibitors. In order to characterise all these ligands and the importance of the distance of the ureido linkage with respect to the electrophilic trap and its influence in potency, an *in-vitro* point measurement of all these inhibitors was performed with the yeast CP.

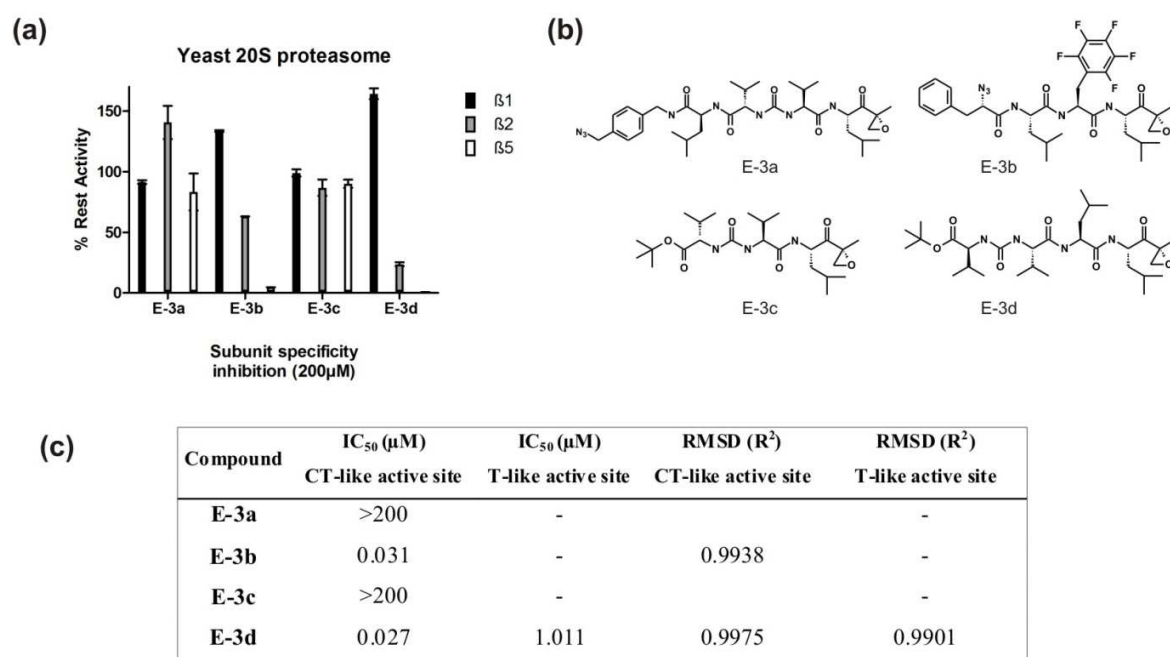


Fig. 37: *In-vitro* characterisation of inhibitors E-3a-d

(a) Point measurements with the distinct active sites. Error bars \pm SD. (b) chemical structure of **E-3a-d**. (c) IC₅₀ of these inhibitors against CT- and T-like activities.

As it can be observed in **Fig. 37**, all the inhibitors presented in this subsection were solely specific for CT-like active site up to 200 μ M concentration, except for **E-3d**. This compound proved to be the most potent inhibitor of this set of ureido containing inhibitors, however, it displayed additional activity for T-like active site. Further *in-vitro* characterisation revealed an IC₅₀ of 27.4 nM for CT and 1 μ M for the T-like active site. Compounds **E-3a** and **E-3c**,

on the other hand showed an $IC_{50} > 200 \mu\text{M}$. Whilst, **E-3b**, a non-ureido based inhibitor, yielded an IC_{50} of 31.6 nM but showed partial inhibition of the T-like active site at 200 μM .

These initial results were followed up by performing a structural evaluation of these inhibitors complexed with the yeast CP. Data sets were collected at 2.6, 3.0, 2.7 and 2.7 Å with an $R_{\text{free}} = 0.242, 0.237, 0.249$ and 0.246 for **E-3a-d** respectively (**Table 14**).

Data collection and refinements of CP:E-3a					
<u>Crystal parameters</u>		<u>Data collection</u>		<u>Refinement (REFMAC5)</u>	
Space group	P2 ₁	Beamline	ID-14 ESRF	Resolution range (Å)	15-2.6
Cell constants (one molecule / AU ^a)	a=135.7Å; b=300.4Å, c=144.1Å; β=113.5 °	Wavelength (Å)	1.0	No of atoms	50981
		Resolution range (Å) ^b	15-2.6 (2.7-2.6)	Protein	49534
		No. observations	312780	Water	1342
		No. unique reflections ^c	920118	$R_{\text{work}}/R_{\text{free}}$ (%) ^e	23.6 / 24.2
		Completeness (%) ^b	96.7 (97.3)	rmsd bond deviations	0.004/0.84
		R_{merge} (%) ^{b, d}	8.1 (52.3)	bond length (Å) (°) ^f	3
		I/s (I) ^b	8.71 (2.04)	Average B-factor (Å ²)	65.343
				Ramachandran Plot (%) ^g	6127 (97.1%) 157 (2.5%) 26 (0.4%)

Data collection and refinements of CP:E-3b					
<u>Crystal parameters</u>		<u>Data collection</u>		<u>Refinement (REFMAC5)</u>	
Space group	P2 ₁	Beamline	ID-14 ESRF	Resolution range (Å)	15-3.0
Cell constants (one molecule / AU ^a)	a=134.6 Å;	Wavelength (Å)	1.0	No of atoms	51008
	b=300.5 Å, c=143.4 Å; β=112.7 °			Protein	49534
		Resolution range (Å) ^b	15-3.0 (3.1- 3.0)	Water	1342
		No. observations	502932	R _{work} /R _{free} (%) ^e	22.6 / 23.7
		No. unique reflections ^c	190229	rmsd bond deviations	0.004/0.82
		Completeness (%) ^b	90.8 (90.1)	bond length (Å) (°) ^f	0
		R _{merge} (%) ^{b, d}	11.5 (49.3)	Average B-factor (Å ²)	61.212
		I/s (I) ^b	6.22 (1.89)	Ramachandran Plot (%) ^g	174 (2.8%) 26 (0.4%)

Data collection and refinements of CP:E-3c					
<u>Crystal parameters</u>		<u>Data collection</u>		<u>Refinement (REFMAC5)</u>	
Space group	P2 ₁	Beamline	ID-14 ESRF	Resolution range (Å)	15-2.7
Cell constants (one molecule / AU ^a)	a=135.9 Å;	Wavelength (Å)	1.0	No of atoms	50975
	b=300.2 Å, c=143.8 Å; β=113.4 °			Protein	49534
		Resolution range (Å) ^b	15-2.7 (2.8-2.7)	Water	1342
		No. observations	819816	R _{work} /R _{free} (%) ^e	23.7 / 24.9
		No. unique reflections ^c	276521	rmsd bond deviations	0.004/0.81
		Completeness (%) ^b	95.7 (94.6)	bond length (Å) (°) ^f	4
		R _{merge} (%) ^{b, d}	10.4 (48.4)	Average B-factor (Å ²)	50.754
		I/s (I) ^b	6.83 (1.99)	Ramachandran Plot (%) ^g	6114 (96.9%) 174 (2.8%) 22 (0.3%)

Data collection and refinements of CP:E-3d					
<u>Crystal parameters</u>		<u>Data collection</u>		<u>Refinement (REFMAC5)</u>	
Space group	P2 ₁	Beamline	ID-14 ESRF	Resolution range (Å)	15-2.7
Cell constants (one molecule / AU ^a)	a=135.7 Å;	Wavelength (Å)	1.0	No of atoms	51151
	b=300.7 Å;			Protein	49506
	c=143.8 Å;			Water	1342
	β=113.0 °			R _{work} /R _{free} (%) ^e	23.4 / 24.6
		Resolution range (Å) ^b	15-2.7 (2.8-2.7)	rmsd bond deviations	0.004/0.82
		No. observations	990868	bond length (Å) (°) ^f	9
		No. unique reflections ^c	289759	Average B-factor (Å ²)	53.728
		Completeness (%) ^b	99.1 (99.1)	Ramachandran Plot (%) ^g	6120 (97.1%)
		R _{merge} (%) ^{b, d}	6.0 (57.2)		164 (2.6%)
		I/s (I) ^b	14.42 (2.81)		22 (0.3%)

Table 14 Data collection and refinement statistics E-3a-da-g according to **Table 3**

All crystal structures revealed a clear electron density for the ligands, whereby the epoxyketone formed the customary N-morpholino ring upon binding to the Thr1 and the peptide backbone adopts the formation of an antiparallel β-sheet in the substrate binding channel. **E-3a-d** exhibits a leucine moiety in P1 position which protrudes into the S1 pocket and induces a uniform concerted structural rearrangement of the Met45 residue. This residue therefore adapts to the size of this moiety and forms perfect Van-der-Waals interactions with the ligand, thus highlighting the preference of these compounds for the CT-like active site. The dissimilarities on the binding of these inhibitors therefore involve uniquely the specificity pockets S3-S5, due to the lack of the S2 pocket found in the 20S proteasome, as well as the ureido group for compounds **E-3a-c**.

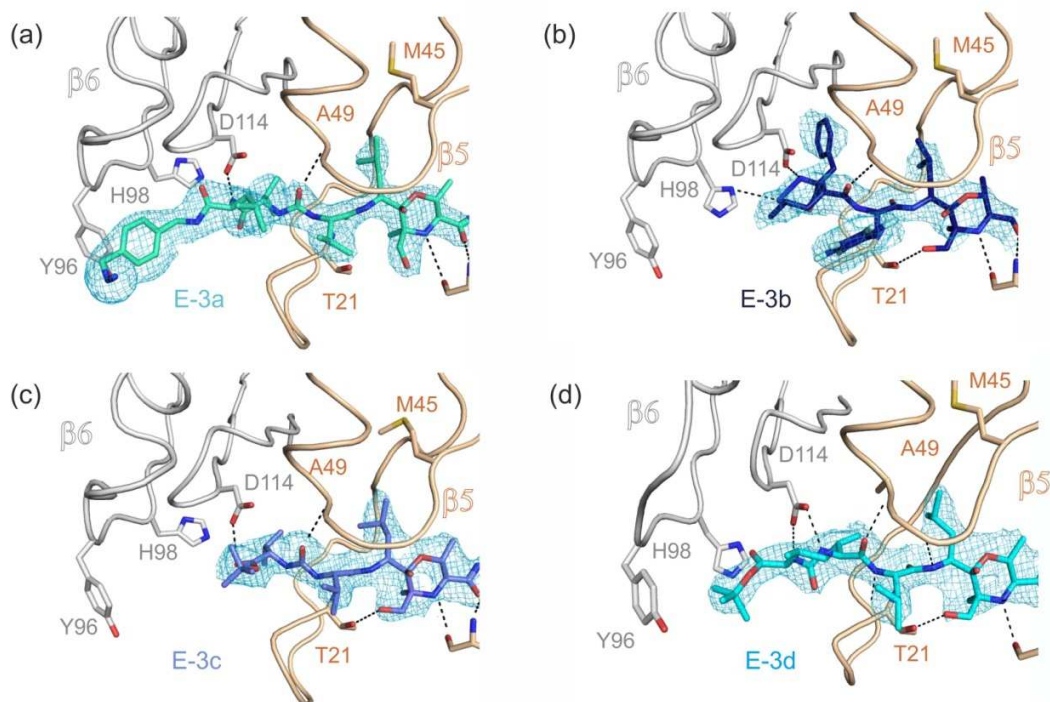


Fig. 38: Complex structures of the CT-like active site with E-3a-d

(a) E-3a (b) E-3b (c) E-3c and **(d) E-3d** respectively. Main interactions between the ligand and the different side chains of the CT-like active site formed by subunits $\beta 5$ and $\beta 6$ are coloured in wheat and grey respectively.

The ureido containing compounds **E-3a** and **E-3c** both possess a small Val groups in positioned in S2 and S3, these Vals barely interact with any groups in the active site. The ureido moiety of these compounds is positioned after the P2 side chain, leading to a slightly shifted P4 group, (leucine and BOC group respectively) which cannot protrude into the S4 site and therefore displays impaired Van-der-Waals interactions with the side chains of this pocket. The shift observed in the P4 site chain is most prominent in compound **E-3c** whereby, the P4 BOC group shifts apart from the S4 specificity pocket toward the S5-site. Hereby, a concerted movement of both residues His98 and Tyr96 of subunit $\beta 6$ is additionally observed leading to a high energy penalty for a poorly positioned small BOC group. In the case of **E-3a** the bulky benzamidine group positioned in P5 causes this concerted movement of both residues His98

and Tyr96 upon binding. Yet again, this structural rearrangement enlarges this specificity pocket and prevents the adequate fit of this moiety to this pocket (**Fig. 38**).

Interestingly, the complex structure of **E-3d**, whereby the ureido position is located after P3, displayed the ureido moiety tightly bound to Asp114 in $\beta 6$. This tight binding further reinforces the positioning of the peptide backbone and consequently the antiparallel β -sheet formation. Furthermore, the side chains from P4-P5 are consequently adequately positioned in the S4-S5 proteasome binding pockets.

These results demonstrate that the positioning of the ureido group can severely affect the binding affinity of these compounds, leading to a decrease in the IC_{50} from $>200 \mu M$ to the low nanomolar range, 27.4 nM. Compound **E-3d** showed that if the ureido is placed in P3 position, the P4 and P5 do place themselves in the S4 and S5 subunit sites without undertaking any conformational changes. Therefore, the ureido moiety in P3 supports fixation of the peptide backbone and the correct positioning of the individual side chains of the ligand (**Fig. 39**). Furthermore, the superposition of **E-3a**, **E-3c** and **E-3d** showed that, P1 and P2 fit almost identically, whereas the P3-P5 moieties differ greatly in their orientation depending on the ureido positioning.

In the case of compound **E-3b**, the P1 together with P3 side chain are involved in a plenitude of Van-der-Waals interactions that stabilise the antiparallel β -sheet formation of the peptide backbone. This inhibitor does not contain an ureido moiety; however it is the benzyl ring in P3 which aids in the correct positioning of the inhibitor. In addition, both Asp114 and His98 interact through hydrogen bonding with the N_3 group in P4 adding extra stability to this inhibitor bound to the CP. Remarkably, **E-3b** and **E-3d** revealed similar IC_{50} values, 31.6 and 27.4 nM respectively, for the CT-like active site. The overlay of both structures proved that both inhibitors adopt identical positioning of the backbone and both P3 side chain are positioned adequately in the S3 pocket. Furthermore, both the ureido and the N_3 moiety, in **E-3d** and **E-3b** respectively, interact with the Asp114 aiding in the peptide backbone positioning (**Fig. 39**).

Moreover, compared to **E-3b** which was only bound to the CT-like active site, **E-3d** was rather unspecific and located in all active sites. The kinetic data revealed an IC_{50} of 1.0 μM for the T-like activity and no inhibition in the C-like active site at 200 μM . The complex structure of **E-3d** and yeast CP led to a rational explanation for the un-specificity of this compound.

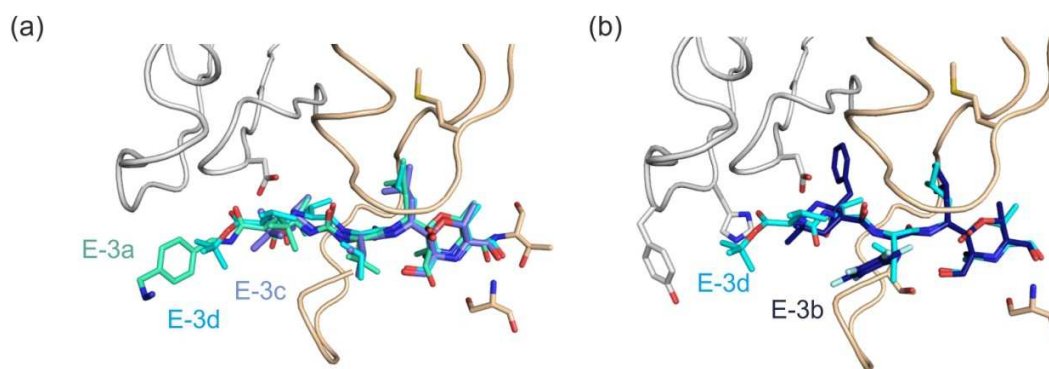


Fig. 39: Structural superposition of CT-like active site with E-3a-d

(a) E-3a, E-3c and E-3d, containing the ureido moiety. **(b)** the most potent CT-like active site inhibitors E-3b and E-3d.

As it can be observed in **Fig. 40**, compound **E-3d** showed that the epoxyketone war head was bound to the Thr1 through N-morpholino ring formation and the peptide backbone forms an antiparallel β -sheet formation in all active sites. The Leu moiety located in P1 position protrudes clearly in the S1 pocket and in the case of the CT-like active site it induces a uniform concerted structural rearrangement of Met45 residues and fits well in this hydrophobic like binding site. However, this Leu side chain does not accommodate itself as comfortably in both the T- and C-like active site due to the hydrophilic nature of the S1 pockets in these two active sites. The P2 side chain is in all active sites solvent exposed and does not play a role in the inhibitor stability. However, the ureido moiety is well positioned by the Asp114 as well in the T-like active site further stabilising the peptide backbone in this active site.

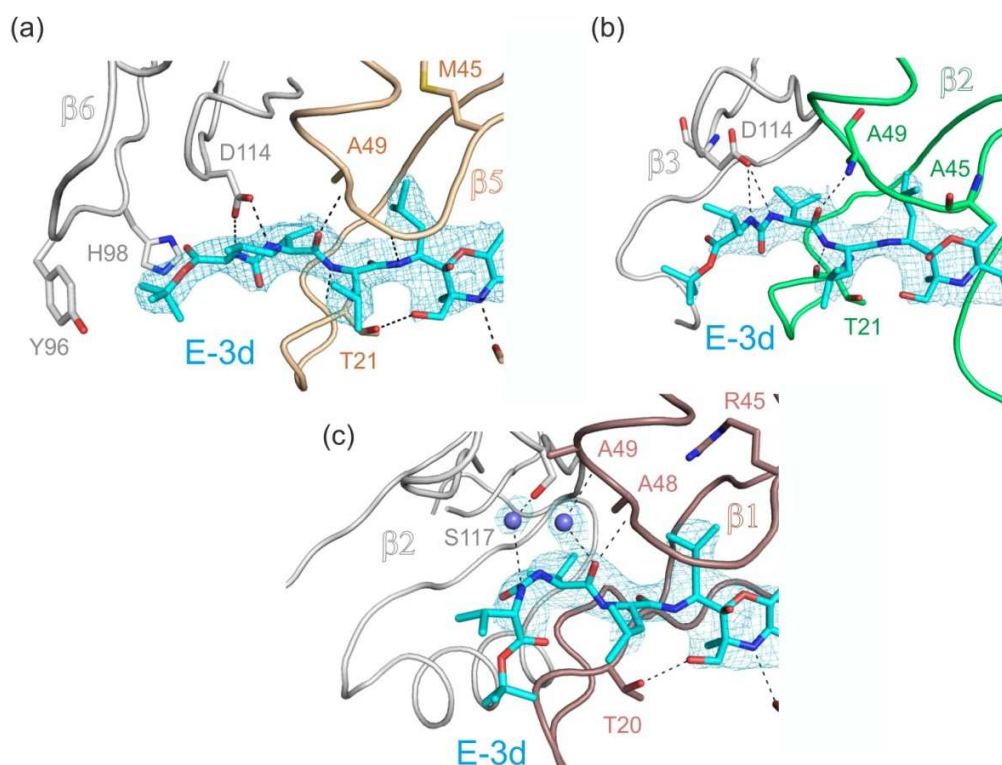


Fig. 40: Complex structure of E3d with yeast proteasome

Complexed structure of E-3d in **(a)** CT-like active site **(b)** T-like active site and **(c)** C-like active site. Hereby, all active sites are represented in cartoon loop form under a wheat, green and magenta colour for $\beta 5$, $\beta 2$ and $\beta 1$ and inactive subunits $\beta 6$, $\beta 3$ and $\beta 2$ are depicted in grey. The inhibitor **E-3d** is represented in stick form and in colour blue with the appropriate omit map of each active site.

In the C-like active site it could clearly be observe that the ureido moiety does not hydrogen bond to any residue in the active site explaining the decrease in affinity of this inhibitor towards this site. Furthermore, P4 and P5 side chains play a crucial role in the increase in affinity for this inhibitor towards the CT-like active site in comparison to the T-like active site. Hereby, the more spacious CT-like active site embraces the BOC protecting group further fixing this inhibitor in-place while the electron density map of this inhibitor is weak in the T- and C-like active site which indicates the exposure of this side chain towards an empty solvent rich area.

We therefore can determine that although the ureido site positioning after P3 increases the inhibitor's affinity for CT-like active by more than 8000 fold it does also decrease this

inhibitor's subunit specificity. This information combined with some of the positive characteristics of **E-3b**, described through its complex structure elucidation, may however aid in forming a more potent yet CT-like specific inhibitor using this ureido moiety.

5.2.7 T-like active site specific vinyl sulfone based inhibitors

Our collaborators have proven that epoxyketone containing inhibitors possess a more potent inhibitory profile than their vinyl sulfone counterparts. However, epoxyketones have additionally shown to be less subunit selective. Consequently to obtain a highly T-like subunit specific inhibitor, our collaborators synthesised a group of peptide vinyl sulfone based inhibitors maintaining a hydrophilic P1 group and varying the different P2-P4 side chains. In order to initially characterise these inhibitors an *in-vitro* point measurement of all these inhibitors was performed with yeast CP (**Fig. 41**).

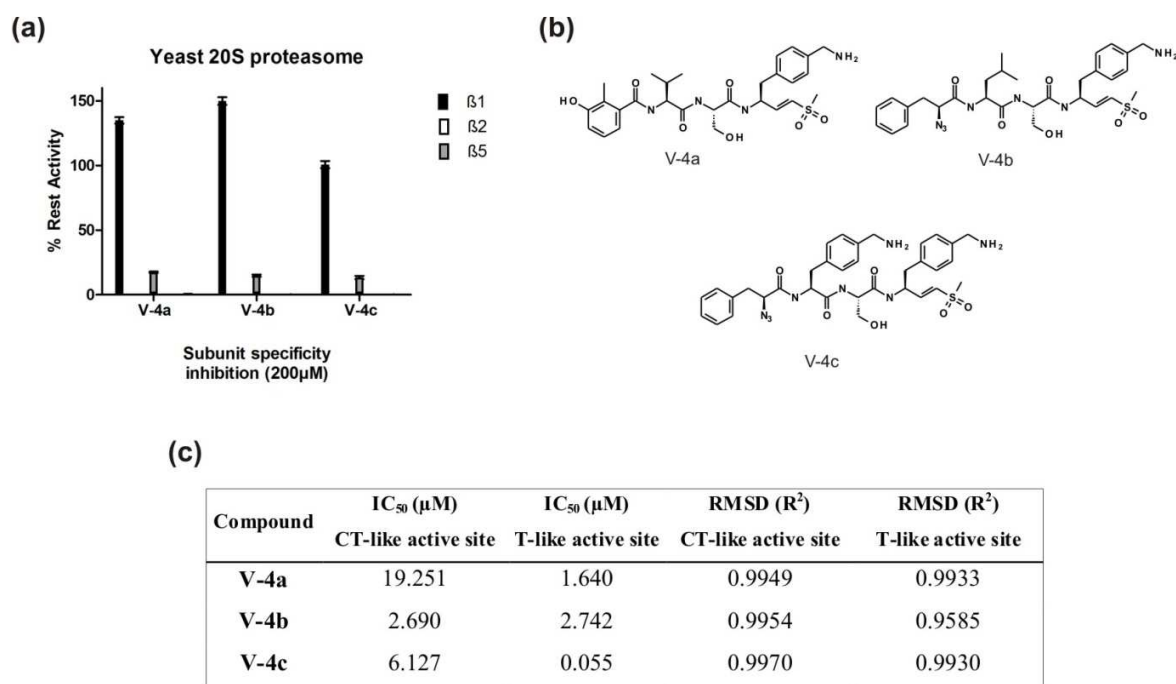


Fig. 41: *In-vitro* characterisation of inhibitors V-4a-c

(a) Point measurements with all three different subunit specificity sites. (b) Chemical structure of compounds V-4a-c. (c) Table containing IC₅₀ values both against T- and CT-like active site.

Inhibitors **V-4a-c** showed, at 200 μM concentrations, activities towards both the T-like and the CT-like active site but not that of C-like active site. Further *in-vitro* characterisation of these inhibitors revealed **V-4a** to have an IC_{50} against T-like active site of 1.6 μM and a ten fold lower affinity towards the CT-like active site ($\text{IC}_{50} = 19.3 \mu\text{M}$). On the other hand, compound **V-4b** revealed an equal affinity for both active sites with IC_{50} s of 2.6 μM against the T-activity and 2.7 μM against CT-activity. The compound with highest affinity for the T-like active site turned out to be **V-4c** which revealed an IC_{50} of 55.0 nM and 6.1 μM , for the T- and CT-like active site respectively, a hundred fold increase in the IC_{50} , towards the CT-like active site.

Following these promising results a structural evaluation was performed of these inhibitors in complex with the yeast CP and full data sets were collected at 2.9, 2.7, 3.1 \AA with an $R_{\text{free}} = 0.230, 0.231, 0.238$ respectively in ID-14 at the European Synchrotron Radiation Facility, Grenoble, France (**Table 15**).

Data collection and refinements of CP:V-4a					
Crystal parameters		Data collection		Refinement (REFMAC5)	
Space group	P2 ₁	Beamline	ID-14 ESRF	Resolution range (\AA)	15-2.9
Cell constants (one molecule / AU ^a)	a=137.0 \AA ; b=299.5 \AA ; c=145.0 \AA ; β =113.2 $^{\circ}$	Wavelength h (\AA)	1.0	No of atoms	51043
		Resolution range (\AA) ^b	15-2.9 (3.0-2.9)	Protein	49548
		No. observations	811451	Water	1342
		No. unique reflections ^c	233547	$R_{\text{work}}/R_{\text{free}}$ (%) ^e	22.1 / 23.0
		Completeness (%) ^b	98.6 (99.5)	rmsd bond deviations bond length (\AA) ($^{\circ}$) ^f	0.004/0.83 0
		R_{merge} (%) ^{b, d}	6.6 (48.3)	Average B-factor (\AA^2)	50.483
		I/s (I) ^b	16.88 (3.91)	Ramachandran Plot (%) ^g	6117 (96.9%) 172 (2.7%) 23 (0.4%)

Data collection and refinements of CP:V-4b					
<u>Crystal parameters</u>		<u>Data collection</u>		<u>Refinement (REFMAC5)</u>	
Space group	P2 ₁	Beamline	ID-14 ESRF	Resolution range (Å)	15-2.7
Cell constants (one molecule / AU ^a)	a=136.3Å; b=301.1 Å, c=144.3 Å; β=113.1 °	Wavelength (Å)	1.0	No of atoms	51072
		Resolution range (Å) ^b	15-2.7 (2.8-2.7)	Protein	49548
		No. observations	989813	Water	1342
		No. unique reflections ^c	287367	R _{work} /R _{free} (%) ^e	22.2 / 23.1
		Completeness (%) ^b	98.4 (90.0)	rmsd bond deviations bond length (Å) (°) ^f	0.004/0.8 08
		R _{merge} (%) ^{b, d}	4.9 (47.3)	Average B-factor (Å ²)	57.346
		I/s (I) ^b	17.98 (2.52)	Ramachandran Plot (%) ^g	6133 (97.2%) 160 (2.5%) 19 (0.3%)

Data collection and refinements of CP:V-4c					
<u>Crystal parameters</u>		<u>Data collection</u>		<u>Refinement (REFMAC5)</u>	
Space group	P2 ₁	Beamline	ID-14 ESRF	Resolution range (Å)	15-3.1
Cell constants (one molecule / AU ^a)	a=136.3Å; b=301.0 Å, c=144.3 Å; β=112.5 °	Wavelength (Å)	1.0	No of atoms	51088
		Resolution range (Å) ^b	15-3.1 (3.2-3.1)	Protein	49548
		No. observations	547474	Water	1342
		No. unique reflections ^c	176097	R _{work} /R _{free} (%) ^e	21.2 / 23.8
		Completeness (%) ^b	92.2 (94.9)	rmsd bond deviations bond length (Å) (°) ^f	0.004/0.8 06
		R _{merge} (%) ^{b, d}	6.3 (46.9)	Average B-factor (Å ²)	58.455
		I/s (I) ^b	16.52 (3.70)	Ramachandran Plot (%) ^g	6101 (96.7%) 189 (3.0%) 22 (0.3%)

Table 15 Data collection and refinement statistics V-4a-c

a-g are described in **Table 3**.

The refined crystal structures revealed clear electron densities of all three compounds in the CT- and T-like proteasomal active site. As expected the vinyl sulfone was bound to the Thr1 through its usual 1,4-Michael addition reaction and the peptide backbone adopts an antiparallel β -sheet. In case of the T-like active site the benzamidine group in P1 protrudes into the spacious and hydrophilic S1 pocket and is further stabilised by hydrogen bonding of the amine to Glu53. Additionally, the P2 groups were shown to be solvent exposed due to their orientation towards the inexistent S2 site chain. Furthermore, a 50 fold decrease in the IC_{50} was observed between **V-4b** and **V-4c**, which differ from each other only in their P3 position. The crystallographic results reflect the impact of this side chain on the IC_{50} .

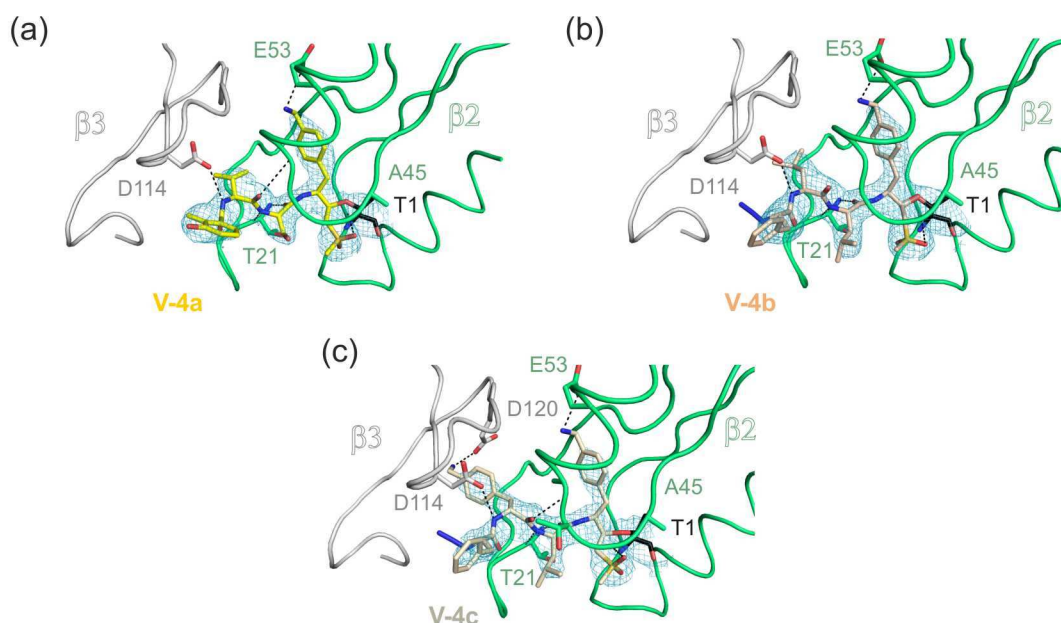


Fig. 42: T-like active site of the complex structure of yeast 20S proteasome with V-4a-c

(a) V-4a (b) V-4b and (c) V-4c The different subunits are shown in cartoon loops, subunits $\beta 2$ and $\beta 3$, are depicted in green and grey, respectively. The inhibitors are shown in stick form and coloured in yellow, salmon and grey, for V-4a-c respectively, with their original electron density map. H-bonds are hereby depicted in dotted black lines.

The P3 benzamidine group forms a tight hydrogen bond interaction with Asp120 and accommodates the aromatic group perfectly in the S3 pocket through a series of Van-der-Waals

interactions which further stabilising this moiety. Additionally, the aromatic group of **V-4a** and the azide and benzene group in **V-4b** and **V-4c** located in P4 both protrude nicely into the S4 pocket (**Fig. 42**). These residues are stabilised by Van-der-Waals interactions with Leu115 and Ile116 which hereby form a defined S4-pocket. The N₃ group found in compounds **V-4b** and **V-4c** is not clearly defined in the electron density, though weak hydrogen bonds with Gln22 in $\beta 2$ and Asp114 in $\beta 3$ can further stabilise this moiety (**Fig. 42**). As shown in **Fig. 43** the overlay of all compounds in the T-like active site it was shown that the main chain atoms of all inhibitors adopt, the formation of an antiparallel β -sheet, identically, thus it is only the side chains that cause an effect in the binding affinity.

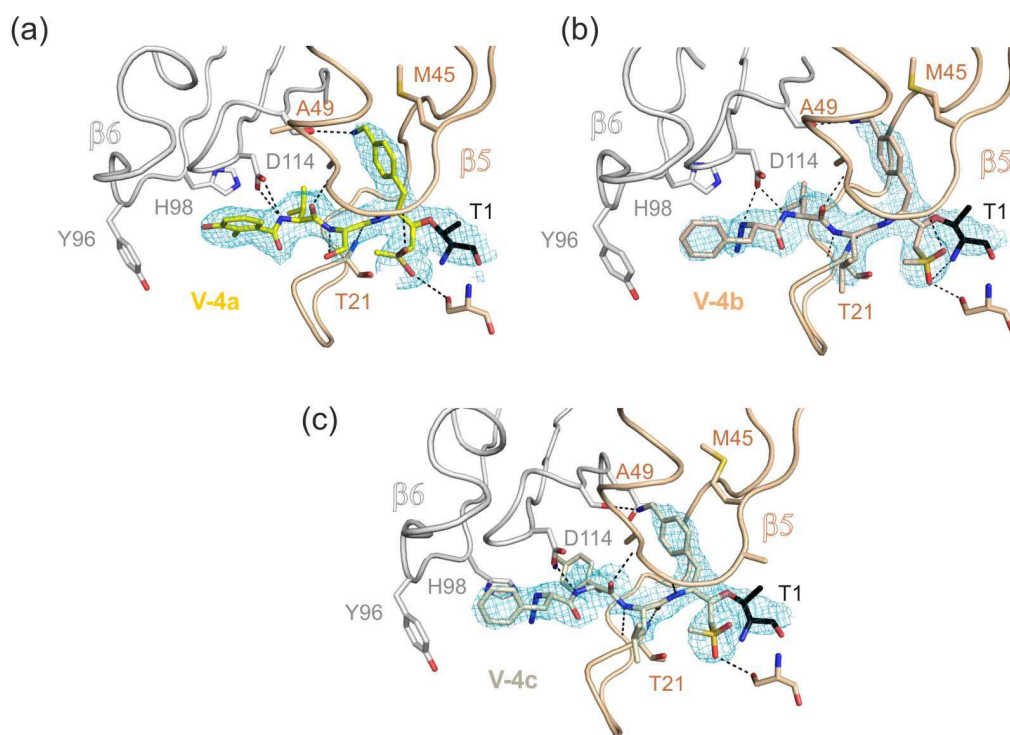


Fig. 43: CT-like active site of the yeast 20S proteasome complex structure with V-4a-c

(a) **V-4a** (b) **V-4b** and (c) **V-4c** The different subunits are shown in coils, subunits $\beta 5$ and $\beta 6$, are depicted in wheat and grey colour, respectively.. The inhibitors colour coding is shown as above.

The side chains of compounds **V-4a** and **V-4b** (**Fig. 44**) proved to bind practically in an identical position, which explains the similar IC₅₀ values of both compounds. However, in the

case of **V-4c** the side chain P3 protrudes deeper in the S3 pocket and form a series of hydrogen bonds and Van-der-Waals interactions that have a profound effect in the inhibition of the T-like active site.

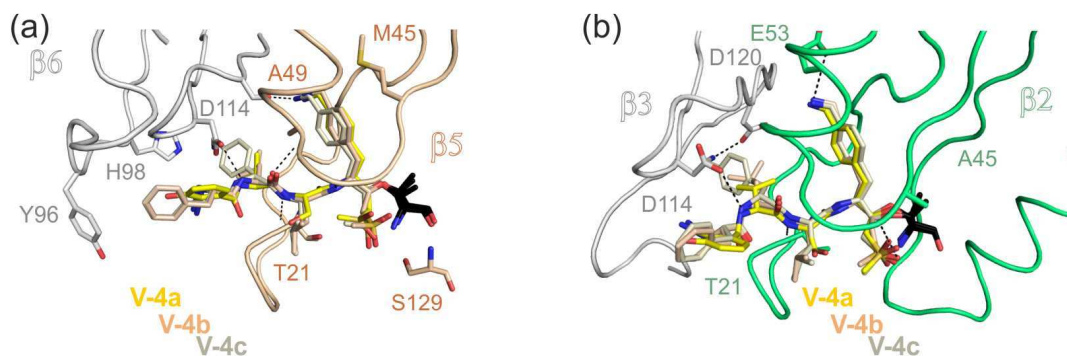


Fig. 44: Overlay of complex structures of 20S proteasome with compounds V-4a-c

Superposition of **V-4a-c:CP**, located in both (a) CT- and (b) T-like active site. $\beta 5$, $\beta 2$ are depicted in cartoon form in wheat and green colour. $\beta 3$ and $\beta 6$ are shown in cartoon form and colour grey

In the case of the CT-like active site, as for T-like active site, the benzamidine group in P1 of this set of inhibitors, protrudes into the hydrophobic S1 pocket and is stabilised by hydrogen bonding to Glu132 located in $\beta 6$ subunit. In agreement to the T-like active centre, the P2 side chain of the ligands is pointing to a solvent space and therefore has no effect in the binding. The S3 pocket in CT-like active site is large and so has enough space to accommodate the Val, Leu and benzamidine groups in **V-4a-c** respectively. Nevertheless these groups are not tightly bound and do not form any positive interactions. This effect adds to the substrate preference of this inhibitor towards the T-like active site and gives a structural explanation for the similarities and dissimilarities between the IC_{50} 's of both **V-4b** and **V-4c** in the CT- and T-like active site respectively. Furthermore, the N_3 group in the case of **V-4b** and **V-4c** is well defined in the electron density and forms strong hydrogen bonds with Asp114 further stabilising this inhibitors. Moreover, the larger benzyl group of **V-4b** and **V-4c** protrudes into the S4 pocket and performs more Van-der-Waals interactions than the P4 side chain of **V-4a** (Fig. 44).

A competition assay of compounds **V-4c** in HEK293T cell lysate, **Fig. 46**, clearly indicated that this inhibitor is highly specific to only the T-like active site in human proteasome.



Fig. 45: Competition assay of compound V-4c in HEK293T cell lysate

Cell lysates were treated with 0-50 μM concentration of inhibitor for 1 hr. at 37°C. Residual proteasome activity was labelled with MVB003 and can be seen for both $\beta 5$ and $\beta 1$. $\beta 2$ does not show any residual activity past 0.5 μM concentration, proving the specificity of this inhibitor towards the T-like active site in human proteasome (Experiments performed by Wouter van-der-Linden, group of Prof. Overkleeft, Leiden University, Holland).

Therefore, a superposition of bovine proteasome and the CP:**V-4c** complex structure was performed to clarify this specificity difference between both organisms. Bovine proteasome structure was used due to the high degree of similarity to human proteasome whereby $\beta 2$ is 100 % and $\beta 3$ is 99 % identical (sequence comparison percentages performed with program LALIGN). This similarity is much higher than the CP from yeast and human which only shows a sequence similarity of 54 % in $\beta 2$ and 62 % in $\beta 3$ (Huber et al., 2012; Unno et al., 2002).

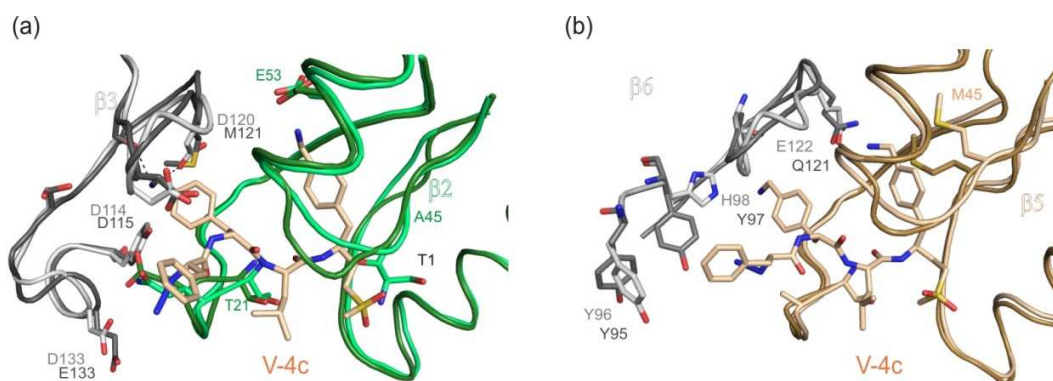


Fig. 46: Structural superposition of bovine and yeast 20S proteasome with V-4c

Located in **(a)** T-like active site whereby yeast and human $\beta 2$ and $\beta 3$ are depicted in light and dark green and grey colours respectively **(b)** CT-like active site whereby yeast and human $\beta 5$ and $\beta 6$ are depicted in light and dark wheat and grey colours respectively.

The superposition of both yeast CP complexed with **V-4c** and bovine CP, showed that side chains P1, P2 and P4 accommodated nearly identical in the S1, S2 and S4 pockets in T-like active site of the bovine CP.

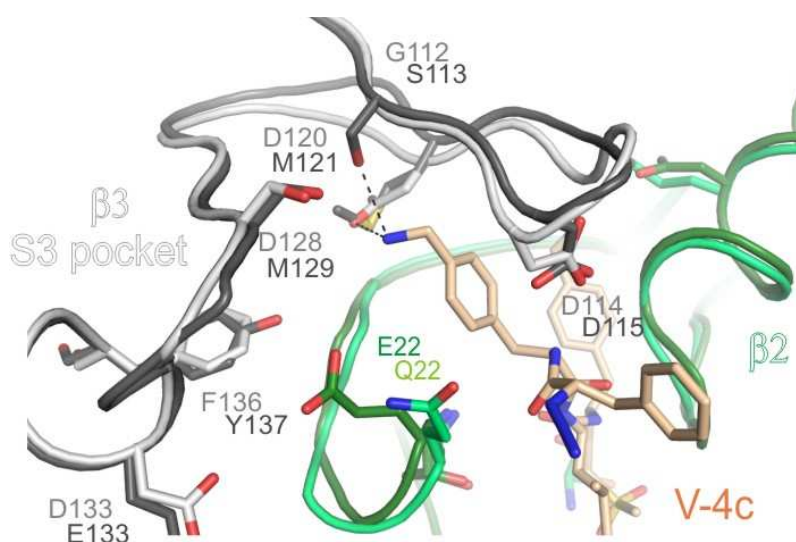


Fig. 47: Structural superposition of bovine and yeast 20S proteasome with V-4c

T-like active site shows the differences in residues in the S3 pocket, hereby, yeast and human $\beta 2$ and $\beta 3$ are depicted in light and dark green and grey colours respectively.

However, our structural explanation for the importance of the P3 side chain in the T-like potency is not suitable. The hydrogen bonding that stabilise P3 side chain group in the yeast CP:**V-4c** cannot be performed, as Ala120 that stabilises this side chain in yeast is not present in human β 3, (Met121 takes its place) (**Fig. 47**).

Nevertheless, although Asp120 is not present in the S3 pocket of bovine T-like active site, other hydrophilic residues are in close proximity to the P3 side chain such as Ser113, Glu96 and Tyr137 in β 3. These key residues, which are hydrophobic in yeast, are equivalent to Gly113, Gly96 and Phe146 respectively and aid in the further stabilisation of this moiety. Specially, Ser113 which forms a hydrogen bond with the amine group, of the benzamidine moiety, in the P3 side chain. (**Fig. 47**). Additionally, as it can be observed in **Fig. 47**, the Gln22 in the yeast CP β 2 is changed to a Glu22 in bovine CP, stabilising the inhibitor further in the bovine CP. Furthermore, superposition of the CT-like active site of bovine and yeast CPs revealed additional insights into the high subunit specificity towards T-like active site of this inhibitor towards human proteasome. As shown in **Fig. 45**, the benzamidine group which protrudes into the S1 pocket forms a hydrogen bond with the Glu122. However, this residue is replaced by Gln121 which doesn't form such a tight bond to the amine group of the benzamidine. P2 and P3 groups show identical binding in both species, however, the N₃ and benzene ring proved to have a big effect in the binding of this inhibitor. This P4 side chain fits adequately to the pocket formed by His98 and Tyr96 in yeast; however, in the bovine CP the H98 in β 6 is replaced by a Tyr97 in β 6. Tyr97 residue possesses a bulkier group that repels the benzyl group and doesn't allow its correct positioning.

We therefore can determine that the P1 site is important for subunit specificity binding as well as the P3 site. The benzamidine moiety in position P3 interacts with a multitude of hydrophilic residues in the S3 pocket and aids in the subunit specificity towards the T-like active site. This rational explanation combined with modelling techniques could lead to alternative moieties in this position with a much higher affinity to the T-like active site. However, *in-vivo* tests by our collaboration partners indicated that, unlike compound **V-4b**, compound **V-4c** does

not seem to cross the cell membrane. This result could be due to the high PKa value of this inhibitor. Yet again, the information here described could be taken further through modelling techniques in order to combine modelling, chemical synthesis, crystallography and *in-vivo* and *in-vitro* techniques to design a fully specific T-like active site inhibitor. Work that is currently ongoing.

6 Conclusion

In this work a series of reversible and irreversible proteasome inhibitors were presented which have been successfully characterised using a combination between *in-vitro*, *in-vivo* assays and complexed structures with the CP. These techniques have been hereby combined for the analysis and characterisation of different types of 20S proteasome inhibitors, ranging from novel binding mode inhibitors to complete CP subunit specific inhibitors. Therefore, in combination these results provide an overview of 20S proteasome inhibition and deliver new insights into this scientifically demanding research field. Additionally, the importance of structural elucidation of inhibitors in complex with their target has proven to be a technique that is vital for drug design. Nevertheless, for a full characterisation an additional study into the thermodynamic of binding to the 20S proteasome is imperative, as it is hitherto not well understood. However, limitations of techniques such as isothermal titration calorimetry, due to the excessive batch size required, make this study difficult and a challenging, yet necessary, research area in the future of proteasome inhibition.

Nevertheless, the information here described is of crucial value into the proteasome inhibition field. Hereby, a strong inhibitory binding profile of novel proteasome ligands, the **Hus**, was identified in defined specificity pockets that have hitherto not been explored for proteasomal drug design. Additionally, a series of different reversible and irreversible peptides with important site specific characteristics have been characterised. Therefore, this research work could, in the future, be combined with molecular modelling techniques, for prospect subunit specific as well as type specific CP drug design.

7 References

Adams, J., Behnke, M., Chen, S., Cruickshank, A. A., Dick, L. R., Grenier, L., et al. (1998). Potent and selective inhibitors of the proteasome: dipeptidyl boronic acids. *Bioorg Med Chem Lett*, 8(4), 333-338.

Adams, J., Palombella, V. J., Sausville, E. A., Johnson, J., Destree, A., Lazarus, D. D., et al. (1999). Proteasome inhibitors: a novel class of potent and effective antitumor agents. *Cancer Res*, 59(11), 2615-2622.

Armstrong, A., & Scutt, J. N. (2004). Total synthesis of (+)-belactosin A. *Chem Commun (Camb)*(5), 510-511.

Asai, A., Hasegawa, A., Ochiai, K., Yamashita, Y., & Mizukami, T. (2000). Belactosin A, a novel antitumor antibiotic acting on cyclin/CDK mediated cell cycle regulation, produced by *Streptomyces* sp. *J Antibiot (Tokyo)*, 53(1), 81-83.

Basse, N., Piguel, S., Papapostolou, D., Ferrier-Berthelot, A., Richy, N., Pagano, M., et al. (2007). Linear TMC-95-based proteasome inhibitors. *J Med Chem*, 50(12), 2842-2850.

Boccardo, M., Morgan, G., & Cavenagh, J. (2005). Preclinical evaluation of the proteasome inhibitor bortezomib in cancer therapy. *Cancer Cell Int*, 5(1), 18.

Bochtler, M., Ditzel, L., Groll, M., & Huber, R. (1997). Crystal structure of heat shock locus V (HslV) from *Escherichia coli*. *Proc Natl Acad Sci U S A*, 94(12), 6070-6074.

Bogyo, M., McMaster, J. S., Gaczynska, M., Tortorella, D., Goldberg, A. L., & Ploegh, H. (1997). Covalent modification of the active site threonine of proteasomal beta subunits and the *Escherichia coli* homolog HslV by a new class of inhibitors. *Proc Natl Acad Sci U S A*, 94(13), 6629-6634.

Bond, G. L., Hu, W., Bond, E. E., Robins, H., Lutzker, S. G., Arva, N. C., et al. (2004). A single nucleotide polymorphism in the MDM2 promoter attenuates the p53 tumor suppressor pathway and accelerates tumor formation in humans. *Cell*, 119(5), 591-602.

Borissenko, L., & Groll, M. (2007). 20S proteasome and its inhibitors: crystallographic knowledge for drug development. *Chem Rev*, 107(3), 687-717.

Brünger, A. (1992). X-PLOR version 3.1. A system for X-ray crystallography and NMR. *Yale University Press*, New Haven.

- Brünger, A., Adams, P., Clore, G., DeLano, W., Gros, P., Grosse-Kunstleve, R., et al. (1998). Crystallography & NMR system: A new software suite for macromolecular structure determination. *Acta Crystallogr D Biol Crystallogr.*, 1(54), 905-921.
- Burger, A. M., & Seth, A. K. (2004). The ubiquitin-mediated protein degradation pathway in cancer: therapeutic implications. *Eur J Cancer*, 40(15), 2217-2229.
- Chauhan, D., Hideshima, T., & Anderson, K. C. (2006). A novel proteasome inhibitor NPI-0052 as an anticancer therapy. *Br J Cancer*, 95(8), 961-965.
- Chen, D., Frezza, M., Schmitt, S., Kanwar, J., & Dou, Q. P. (2011). Bortezomib as the first proteasome inhibitor anticancer drug: current status and future perspectives. *Curr Cancer Drug Targets*, 11(3), 239-253.
- Corey, E. J., & Li, W. D. (1999). Total synthesis and biological activity of lactacystin, omuralide and analogs. *Chem Pharm Bull (Tokyo)*, 47(1), 1-10.
- Dahlmann, B., Kopp, F., Kuehn, L., Reinauer, H., & Schwenen, M. (1986). Studies on the multicatalytic proteinase from rat skeletal muscle. *Biomed Biochim Acta*, 45(11-12), 1493-1501.
- DeLano, W. L. (2002). The PyMOL Molecular Graphics System. *DeLano Scientific, San Carlos(CA), USA*.
- Dick, L. R., Cruikshank, A. A., Grenier, L., Melandri, F. D., Nunes, S. L., & Stein, R. L. (1996). Mechanistic studies on the inactivation of the proteasome by lactacystin: a central role for clasto-lactacystin beta-lactone. *J Biol Chem*, 271(13), 7273-7276.
- Dixon, R. A., Diehl, R. E., Opas, E., Rands, E., Vickers, P. J., Evans, J. F., et al. (1990). Requirement of a 5-lipoxygenase-activating protein for leukotriene synthesis. *Nature*, 343(6255), 282-284.
- Emsley, P., Lohkamp, B., Scott, W. G., & Cowtan, K. (2010). Features and development of Coot. *Acta Crystallogr D Biol Crystallogr*, 66(Pt 4), 486-501.
- Escherich, A., Ditzel, L., Musiol, H. J., Groll, M., Huber, R., & Moroder, L. (1997). Synthesis, kinetic characterization and X-ray analysis of peptide aldehydes as inhibitors of the 20S proteasomes from *Thermoplasma acidophilum* and *Saccharomyces cerevisiae*. *Biol Chem*, 378(8), 893-898.
- Esnouf, R. (1997). An extensively modified version of MolScript that includes greatly enhanced coloring capabilities. *J Mol Graph Model*, 15(2), 112-113; 132-114.
- Gallastegui, N., Beck, P., Arciniega, M., Huber, R., Hillebrand, S., & Groll, M. (2012). Hydroxyureas as noncovalent proteasome inhibitors. *Angew Chem Int Ed Engl*, 51(1), 247-249.

- Gallastegui, N., & Groll, M. (2010). The 26S proteasome: assembly and function of a destructive machine. *Trends Biochem Sci*, 35(11), 634-642.
- Gallastegui, N., & Groll, M. (2012). Analysing properties of proteasome inhibitors using kinetic and x-ray crystallographic studies. *Methods Mol Biol*, 832, 373-390.
- Gilbert, N. C., Bartlett, S. G., Waight, M. T., Neau, D. B., Boeglin, W. E., Brash, A. R., et al. (2011). The structure of human 5-lipoxygenase. *Science*, 331(6014), 217-219.
- Groll, M., Balskus, E. P., & Jacobsen, E. N. (2008). Structural analysis of spiro beta-lactone proteasome inhibitors. *J Am Chem Soc*, 130(45), 14981-14983.
- Groll, M., Berkers, C. R., Ploegh, H. L., & Ovaas, H. (2006). Crystal structure of the boronic acid-based proteasome inhibitor bortezomib in complex with the yeast 20S proteasome. *Structure*, 14(3), 451-456.
- Groll, M., Bochtler, M., Brandstetter, H., Clausen, T., & Huber, R. (2005). Molecular machines for protein degradation. *ChemBiochem*, 6(2), 222-256.
- Groll, M., Ditzel, L., Lowe, J., Stock, D., Bochtler, M., Bartunik, H. D., et al. (1997). Structure of 20S proteasome from yeast at 2.4 Å resolution. *Nature*, 386(6624), 463-471.
- Groll, M., Gallastegui, N., Marechal, X., Le Ravalec, V., Basse, N., Richy, N., et al. (2010). 20S proteasome inhibition: designing noncovalent linear peptide mimics of the natural product TMC-95A. *ChemMedChem*, 5(10), 1701-1705.
- Groll, M., Gotz, M., Kaiser, M., Weyher, E., & Moroder, L. (2006). TMC-95-based inhibitor design provides evidence for the catalytic versatility of the proteasome. *Chem Biol*, 13(6), 607-614.
- Groll, M., Heinemeyer, W., Jager, S., Ullrich, T., Bochtler, M., Wolf, D. H., et al. (1999). The catalytic sites of 20S proteasomes and their role in subunit maturation: a mutational and crystallographic study. *Proc Natl Acad Sci U S A*, 96(20), 10976-10983.
- Groll, M., & Huber, R. (2004). Inhibitors of the eukaryotic 20S proteasome core particle: a structural approach. *Biochim Biophys Acta*, 1695(1-3), 33-44.
- Groll, M., Huber, R., & Potts, B. C. (2006). Crystal Structures of Salinosporamide A (NPI-0052) and B (NPI-0047) in Complex with the 20S Proteasome Reveal Important Consequences of beta-Lactone Ring Opening and a Mechanism for Irreversible Binding. *J Am Chem Soc*, 128(15), 5136-5141.
- Groll, M., Kim, K. B., Kairies, N., Huber, R., & Crews, C. M. (2000). Crystal structure of epoxomicin : 20S proteasome reveals a molecular basis for selectivity of alpha 'beta '-

- epoxyketone proteasome inhibitors. *Journal of the American Chemical Society*, 122(6), 1237-1238.
- Groll, M., Koguchi, Y., Huber, R., & Kohno, J. (2001). Crystal structure of the 20 S proteasome:TMC-95A complex: a non-covalent proteasome inhibitor. *J Mol Biol*, 311(3), 543-548.
- Groll, M., Larionov, O. V., Huber, R., & de Meijere, A. (2006). Inhibitor-binding mode of homobelactosin C to proteasomes: new insights into class I MHC ligand generation. *Proc Natl Acad Sci U S A*, 103(12), 4576-4579.
- Groll, M., Nazif, T., Huber, R., & Bogoy, M. (2002). Probing structural determinants distal to the site of hydrolysis that control substrate specificity of the 20S proteasome. *Chem Biol*, 9(5), 655-662.
- Hanada, M., Sugawara, K., Kaneta, K., Toda, S., Nishiyama, Y., Tomita, K., et al. (1992). Epoxomicin, a new antitumor agent of microbial origin. *J Antibiot (Tokyo)*, 45(11), 1746-1752.
- Hershko, A., & Ciechanover, A. (1998). The ubiquitin system. *Annu Rev Biochem*, 67(10), 425-479.
- Homer, R. W., Swanson, J., Jilek, R. J., Hurst, T., & Clark, R. D. (2008). SYBYL line notation (SLN): a single notation to represent chemical structures, queries, reactions, and virtual libraries. *J Chem Inf Model*, 48(12), 2294-2307.
- Huber, E. M., Basler, M., Schwab, R., Heinemeyer, W., Kirk, C. J., Groettrup, M., et al. (2012). Immuno- and constitutive proteasome crystal structures reveal differences in substrate and inhibitor specificity. *Cell*, 148(4), 727-738.
- Ihlenfeldt, W. D., Bolton, E. E., & Bryant, S. H. (2009). The PubChem chemical structure sketcher. *J Cheminform*, 1(1), 20.
- Kabsch, W. (1993). Automatic processing of rotation diffraction data from crystals of initially unknown symmetry and cell constants. *J. Appl. Cryst.*, 26, 795-800.
- Khan, M. L., & Stewart, A. K. (2011). Carfilzomib: a novel second-generation proteasome inhibitor. *Future Oncol*, 7(5), 607-612.
- Kim, K. B., Myung, J., Sin, N., & Crews, C. M. (1999). Proteasome inhibition by the natural products epoxomicin and dihydroeponemycin: insights into specificity and potency. *Bioorg Med Chem Lett*, 9(23), 3335-3340.

Kisselev, A. F., van der Linden, W. A., & Overkleeft, H. S. (2012). Proteasome inhibitors: an expanding army attacking a unique target. *Chem Biol*, *19*(1), 99-115.

Koguchi, Y., Kohno, J., Nishio, M., Takahashi, K., Okuda, T., Ohnuki, T., et al. (2000). TMC-95A, B, C, and D, novel proteasome inhibitors produced by *Apiospora montagnei* Sacc. TC 1093. Taxonomy, production, isolation, and biological activities. *J Antibiot (Tokyo)*, *53*(2), 105-109.

Kohno, J., Koguchi, Y., Nishio, M., Nakao, K., Kuroda, M., Shimizu, R., et al. (2000). Structures of TMC-95A-D: novel proteasome inhibitors from *Apiospora montagnei* sacc. TC 1093. *J Org Chem*, *65*(4), 990-995.

Kraulis, P. J., & (1991). MOLSCRIPT: A Program to Produce Both Detailed and Schematic Plots of Protein Structures.

. *Journal of Applied Crystallography*, *24*, 946-950.

Kuhn, D. J., Chen, Q., Voorhees, P. M., Strader, J. S., Shenk, K. D., Sun, C. M., et al. (2007). Potent activity of carfilzomib, a novel, irreversible inhibitor of the ubiquitin-proteasome pathway, against preclinical models of multiple myeloma. *Blood*, *110*(9), 3281-3290.

Loidl, G., Groll, M., Musiol, H. J., Huber, R., & Moroder, L. (1999). Bivalency as a principle for proteasome inhibition. *Proc Natl Acad Sci U S A*, *96*(10), 5418-5422.

Löwe, J., Stock, D., Jap, B., Zwickl, P., Baumeister, W., & Huber, R. (1995). Crystal structure of the 20S proteasome from the archaeon *T. acidophilum* at 3.4 Å resolution. *Science*, *268*(5210), 533-539.

Mirabella, A. C., Pletnev, A. A., Downey, S. L., Florea, B. I., Shabaneh, T. B., Britton, M., et al. (2011). Specific cell-permeable inhibitor of proteasome trypsin-like sites selectively sensitizes myeloma cells to bortezomib and carfilzomib. *Chem Biol*, *18*(5), 608-618.

Mitsiades, C. S., Mitsiades, N., Hideshima, T., Richardson, P. G., & Anderson, K. C. (2005). Proteasome inhibitors as therapeutics. *Essays Biochem*, *41*, 205-218.

Murata, S., Sasaki, K., Kishimoto, T., Niwa, S., Hayashi, H., Takahama, Y., et al. (2007). Regulation of CD8+ T cell development by thymus-specific proteasomes. *Science*, *316*(5829), 1349-1353.

Nazif, T., & Bogyo, M. (2001). Global analysis of proteasomal substrate specificity using positional-scanning libraries of covalent inhibitors. *Proc Natl Acad Sci U S A*, *98*(6), 2967-2972.

Nemeth, Z. H., Wong, H. R., Odoms, K., Deitch, E. A., Szabo, C., Vizi, E. S., et al. (2004). Proteasome inhibitors induce inhibitory kappa B (I kappa B) kinase activation, I kappa B alpha

degradation, and nuclear factor kappa B activation in HT-29 cells. *Mol Pharmacol*, 65(2), 342-349.

Oikawa, T., Hasegawa, M., Shimamura, M., Ashino, H., Murota, S., & Morita, I. (1991). Eponemycin, a novel antibiotic, is a highly powerful angiogenesis inhibitor. *Biochem Biophys Res Commun*, 181(3), 1070-1076.

Orlowski, R. (2004). Bortezomib and its role in the management of patients with multiple myeloma. *Expert Rev Anticancer Ther.* . 4(2), 171-179.

Ostrowska, H. (2008). The ubiquitin-proteasome system: a novel target for anticancer and anti-inflammatory drug research. *Cell Mol Biol Lett*, 13(3), 353-365.

Palmer, J. T., Rasnick, D., Klaus, J. L., & Bromme, D. (1995). Vinyl sulfones as mechanism-based cysteine protease inhibitors. *J Med Chem*, 38(17), 3193-3196.

Pickart, C. M. (2001). Mechanisms underlying ubiquitination. *Annu Rev Biochem*, 70, 503-533.

Pufahl, R. A., Kasten, T. P., Hills, R., Gierse, J. K., Reitz, B. A., Weinberg, R. A., et al. (2007). Development of a fluorescence-based enzyme assay of human 5-lipoxygenase. *Anal Biochem*, 364(2), 204-212.

Richardson, P. G., & Mitsiades, C. (2005). Bortezomib: proteasome inhibition as an effective anticancer therapy. *Future Oncol*, 1(2), 161-171.

Ruschak, A. M., Slassi, M., Kay, L. E., & Schimmer, A. D. (2011). Novel proteasome inhibitors to overcome bortezomib resistance. *J Natl Cancer Inst*, 103(13), 1007-1017.

Seemüller, E., Lupas, A., Stock, D., Löwe, J., Huber, R., & Baumeister, W. (1995). Proteasome from *Thermoplasma acidophilum*: a threonine protease. *Science*, 268(5210), 579-582.

Sugawara, K., Hatori, M., Nishiyama, Y., Tomita, K., Kamei, H., Konishi, M., et al. (1990). Eponemycin, a new antibiotic active against B16 melanoma. I. Production, isolation, structure and biological activity. *J Antibiot (Tokyo)*, 43(1), 8-18.

Tedesco, D., Zhang, J., Trinh, L., Lalehzadeh, G., Meisner, R., Yamaguchi, K. D., et al. (2007). The ubiquitin-conjugating enzyme E2-EPF is overexpressed in primary breast cancer and modulates sensitivity to topoisomerase II inhibition. *Neoplasia*, 9(7), 601-613.

Tsubuki, S., Saito, Y., Tomioka, M., Ito, H., & Kawashima, S. (1996). Differential inhibition of calpain and proteasome activities by peptidyl aldehydes of di-leucine and tri-leucine. *J Biochem (Tokyo)*, 119(3), 572-576.

- Turk, D. (1992). Improvement of a program for molecular graphics and manipulation of electron densities and its application for protein structure determination. *Thesis*, Technische Universitaet Muenchen.
- Unno, M., Mizushima, T., Morimoto, Y., Tomisugi, Y., Tanaka, K., Yasuoka, N., et al. (2002). The Structure of the Mammalian 20S Proteasome at 2.75 Å Resolution. *Structure*, *10*(5), 609-618.
- Vagin, A. A., Steiner, R. A., Lebedev, A. A., Potterton, L., McNicholas, S., Long, F., et al. (2004). REFMAC5 dictionary: organization of prior chemical knowledge and guidelines for its use. *Acta Crystallogr D Biol Crystallogr*, *60*(Pt 12 Pt 1), 2184-2195.
- Vaguine, A. A., Richelle, J., & Wodak, S. J. (1999). SFCHECK: a unified set of procedures for evaluating the quality of macromolecular structure-factor data and their agreement with the atomic model. *Acta Crystallogr D Biol Crystallogr*, *55*(Pt 1), 191-205.
- van der Linden, W. A., Willems, L. I., Shabaneh, T. B., Li, N., Ruben, M., Florea, B. I., et al. Discovery of a potent and highly beta1 specific proteasome inhibitor from a focused library of urea-containing peptide vinyl sulfones and peptide epoxyketones. *Org Biomol Chem*, *10*(1), 181-194.
- Verdoes, M., Florea, B. I., Menendez-Benito, V., Maynard, C. J., Witte, M. D., van der Linden, W. A., et al. (2006). A fluorescent broad-spectrum proteasome inhibitor for labeling proteasomes in vitro and in vivo. *Chem Biol*, *13*(11), 1217-1226.
- Verdoes, M., Willems, L. I., van der Linden, W. A., Duivenvoorden, B. A., van der Marel, G. A., Florea, B. I., et al. (2010). A panel of subunit-selective activity-based proteasome probes. *Org Biomol Chem*, *8*(12), 2719-2727.
- Vinitsky, A., Cardozo, C., Sepp-Lorenzino, L., Michaud, C., & Orłowski, M. (1994). Inhibition of the proteolytic activity of the multicatalytic proteinase complex (proteasome) by substrate-related peptidyl aldehydes. *J Biol Chem*, *269*(47), 29860-29866.
- Vinitsky, A., Michaud, C., Powers, J. C., & Orłowski, M. (1992). Inhibition of the chymotrypsin-like activity of the pituitary multicatalytic proteinase complex. *Biochemistry*, *31*(39), 9421-9428.
- Wenzel, S. E., & Kamada, A. K. (1996). Zileuton: the first 5-lipoxygenase inhibitor for the treatment of asthma. *Ann Pharmacother*, *30*(7-8), 858-864.
- Wiberg, K., Carlson, K., Aleskog, A., Larsson, R., Nygren, P., & Lindhagen, E. (2009). In vitro activity of bortezomib in cultures of patient tumour cells--potential utility in haematological malignancies. *Med Oncol*, *26*(2), 193-201.

Yang, Y., Kitagaki, J., Dai, R. M., Tsai, Y. C., Lorick, K. L., Ludwig, R. L., et al. (2007). Inhibitors of ubiquitin-activating enzyme (E1), a new class of potential cancer therapeutics. *Cancer Res*, 67(19), 9472-9481.

List of Figures

Fig. 1: The main degradation pathway in eukaryotic cells, the UPS.....	6
Fig. 2: Structure of proteasome	9
Fig. 3: Cleavage mechanism of the CP	11
Fig. 4: CP inhibition	13
Fig. 5: Bortezomib	14
Fig. 6: Crystal structures of 5 different inhibitors in complex with the CT-like active site.....	16
Fig. 7: Chemical structure of β -lactones	22
Fig. 8: Natural product TMC-95A	24
Fig. 9: 20S proteasome structure complexed to the biphenyl-ether based inhibitors BIA 1a and 2a.....	25
Fig. 10: Chemical structure of TMC-95A and the scaffold used for optimisation of TMC-95 derivative	46
Fig. 11: Complexed structure of CP:2a.....	48
Fig. 12: Complex structure of CP with (a) 2b and (b) 2c	51
Fig. 13: TMC-95A derivatives	55
Fig. 14: MES molecule observed in CP:TMC-95A derivatives	56
Fig. 15: Bivalent TMC-95A derivatives	58
Fig. 16: Complex structure of CP: 2h-2j	61
Fig. 17: Structural superposition of bivalent TMC-95A derivatives.....	62
Fig. 18: In-vivo assay of TMC-95A bivalent derivatives.....	63
Fig. 19: Hydroxyurea compounds	65
Fig. 20: In-vitro characterisation of HU1.....	66
Fig. 21: Crystal structure of CP: HU1.....	68
Fig. 22: Schematic overview of CP: HU1	69
Fig. 23: In-vitro characterisation of HU4.....	70
Fig. 24: Crystal complex structure of CP: HU4	72

Fig. 25: In-vitro characterisation of HU4.....	73
Fig. 26: Reversibility of HU8	73
Fig. 27: Complex structure of CP: HU8.....	75
Fig. 28: <i>In-vitro</i> of compound HU5-7	75
Fig. 29: Compound HU9 and HU10	78
Fig. 30: Complex structure of CP: HU9-10	78
Fig. 31: Molecular modelling with HU	79
Fig. 32: Effect of MES molecule in HU binding.....	80
Fig. 33: Human 20S proteasome and HU8-10	81
Fig. 34: <i>In-vivo</i> analysis of HU10	82
Fig. 35: <i>In-vivo</i> analysis of HU12	84
Fig. 36: <i>In-vitro</i> characterisation of 5-LOX of both HU0 and HU8	85
Fig. 37: <i>In-vitro</i> characterisation of inhibitors E-3a-d	87
Fig. 38: Complex structures of the CT-like active site with E-3a-d	91
Fig. 39: Structural superposition of CT-like active site with E-3a-d	93
Fig. 40: Complex structure of E3d with yeast proteasome.....	94
Fig. 41: <i>In-vitro</i> characterisation of inhibitors V-4a-c	95
Fig. 42: T-like active site of the complex structure of yeast 20S proteasome with V-4a-c	98
Fig. 43: CT-like active site of the yeast 20S proteasome complex structure with V-4a-c	99
Fig. 44: Overlay of complex structures of 20S proteasome with compounds V-4a-c	100
Fig. 45: Competition assay of compound V-4c in HEK293T cell lysate	101
Fig. 46: Structural superposition of bovine and yeast 20S proteasome with V-4c	102
Fig. 47: Structural superposition of bovine and yeast 20S proteasome with V-4c	102

List of Tables

Table 1 Mixture for 12% SDS –PAGE electrophoresis.....	38
Table 2 Mixture for 15% SDS –PAGE electrophoresis.....	38
Table 3 Data collection and refinement statistics for yeast CP:2a	47
Table 4 Data collection and refinement statistics 2b and 2c.....	50
Table 5 Data collection and refinement statistics 2d	53
Table 6 Data collection and refinement statistics 2d	54
Table 7 Data collection and refinement statistics 2h-j in complexes with yeast CP	60
Table 8 Data collection and refinement statistics HU-1	67
Table 9 HU1 derivatives	70
Table 10 Data collection and refinement statistics HU-4	71
Table 11 Data collection and refinement statistics HU-8	74
Table 12 Data collection and refinement statistics of HU9 and HU10	77
Table 13 Data collection and refinement statistics HU12	83
Table 14 Data collection and refinement statistics E-3a-d	90
Table 15 Data collection and refinement statistics V-4a-c	97

Abbreviations

5-LOX	5-lipoxygenase
AMC	7-amino-4-methylcoumarin
AAA-ATPase	ATPases Associated with a variety of cellular Activities
BCIP	5-Bromo-4-chloro-3-indoylphosphate
BIA	Biphenyl-Ether-Based compounds
BSA	Bovine Serum Albumin
BrAAP	branched-chain amino acid
CIP	Cahn–Ingold–Prelog
CAL I	Calpain inhibitor I
C-	Caspase-
CP	20S proteasome core particle
CT-	Chymotrypsin-
DUBs	de-ubiquitinating enzymes
H2DCF	dichlorodihydrofluorescein diacetate
DMSO	Dimethyl sulfoxide
BOC	Di-tert-butyl dicarbonate
DMEM	Dulbecco's Modified Eagle Medium
EDTA	Ethylenediaminetetraacetic acid
ESRF	European Synchrotron Radiation Facility
FBS	Fetal bovine Serum
GAPDH	glyceraldehyde-3-phosphate dehydrogenase
IC50	half maximal inhibitory concentration
HU	Hydroxyureas
IL-1	Interleukin-1
IP	intraperitoneal
LPS	lipopolysaccharide

MM	Multiple myeloma
MES	N-morpholino-ethane sulfonic acid molecule
MPD	2-methyl-2,4- pentanediol
NMR	Nuclear magnetic resonance
NUK	nucleophilic water molecule
PBS	Phosphate Buffer Saline
PEG	polyethylene glycol (4[4-(5-nitro-furan-2-ylmethylene)-3,5-dioxo-pyrazolidin-1-yl]-
PYR 41	benzoic acid ethyl ester)
PVDF	polyvinylidene fluoride
KP	Potassium phosphate
M-PER	protein extraction reagent
RPN	Regulatory Particle Non-ATPase proteins
SNAAP	small neutral amino acid
SDS	Sodium Dodecyl Sulfate polyacrylamide
SLS	Swiss Light Source
TEMED	Tetramethylethylenediamine
TLS	Translation/Libration/Screw
TBS	Tris Buffer Saline
TRIS	Tris(hydroxymethyl)-aminomethane
T-	Trypsin-
FDA	U.S. Food and Drug Administration
UB	Ubiquitin
UPS	Ubiquitin Proteasome System
DCF	Xuorescent 2,7-dichloro-Xuorescein

Acknowledgements

First I would like to thank my whole group for their day to day help and Prof. Michael Groll for giving me the opportunity to carry out my PhD in his department. I want to thank my collaboration partners in Germany Prof. Huber from the MPI and Dr. Hillebrand from Bayer Crop Science and international collaborators Prof. Reboud-Ravaux, from *l'université* Pierre et Marie Curie, France, Prof. Overkleeft from Leiden Universiteit, Holand and Prof. Kisselev, from Dortmund Universtity, USA and their groups for the fantastic and successful work we have done together. I would also like to show my gratitude to Richard Feicht and Astrid König which have helped me deeply through my whole PhD and taught me not only science and German but also Bayerisch. *Dankschea!* I am indebted to my colleagues in the lab, which have now become friends; Anja List, Veronika Flügel, Stephe Grubmüller, Nadine Gillmaier and Ingrid Span, for their support, their laughs and the really nice times that we have spent together throughout these last years. Of course, not to forget thanking, fellow PhD students which whom I have developed a wonderful friendship and were there for me in the good and the bad times; Valentina Villa, Natalia Sarmientos and Marcelino Arciniega. I also owe my deepest gratitude to my students Martina Müller, Susanne Mayer and Jochen Früh which have worked side by side with me and have not only learned from me but taught me a lot.

This thesis would not have been possible without the moral support of Liz Hogan and Susan Lauw and all my friends which are far away, my family and my boyfriend's family for which they have my deepest gratitude. Especially my mother, father, sister and grandmother without whom I would have never achieved what I have accomplished personally and academically. Last but not least, I want to give the biggest thank you to the one person that has picked me up when I have been down and made me laugh every day since we are together and whom I love with all my heart, Jonny Mackinnon.

Danksagung

Zunächst möchte ich meiner ganzen Arbeitsgruppe für die tagtägliche Unterstützung danken, und Prof. Michael Groll dafür, mir die Möglichkeit gegeben zu haben, meine Doktorarbeit an seinem Lehrstuhl durchführen zu können. Ich möchte meinen Kollaborationspartnern in Deutschland danken, Prof. Huber vom MPI und Dr. Hillebrand von Bayer Crop Science, und den internationalen Partnern Prof. Reboud-Ravaux, der l'*université* Pierre et Marie Curie, Frankreich Prof. Overkleeft, von der Leiden Universiteit, Niederlande, und Prof. Kisselev der Dortmund University, USA und ihren Gruppen, für die erfolgreiche Zusammenarbeit. Des Weiteren möchte ich Richard Feicht und Astrid König meinen Dank aussprechen, die mir während meiner gesamten Doktorarbeit sehr geholfen haben, und mir nicht nur Wissenschaftliches und Deutsch beigebracht haben, sondern auch Bayrisch. *Dankschea!* Ich bin meinen Laborkollegen zu Dank verpflichtet, die inzwischen zu Freunden geworden sind: Anja List, Veronika Flügel, Stephie Grubmüller, Nadine Gillmaier und Ingrid Span, für ihre Unterstützung, ihr Lachen und die wirklich schönen Zeiten, die wir während diesen letzten Jahren zusammen verbracht haben. Natürlich nicht zu vergessen sind weitere Doktoranden, zu denen ich eine wundervolle Freundschaft entwickelt habe und die in guten, wie in schlechten Zeiten für mich da waren: Valentina Villa, Natalia Sarmientos und Marcelino Arciniega. Zu tiefstem Dank verpflichtet bin ich auch meinen Studenten Martina Müller, Susanne Mayer und Jochen Früh, die mit mir Seite an Seite gearbeitet haben und die nicht nur von mir gelernt haben, sondern von denen ich auch viel lernen konnte.

Diese Arbeit wäre nicht möglich gewesen ohne die moralische Unterstützung von Liz Hogan und Susan Lauw und all meinen Freunde, die weit weg sind, meiner Familie und der Familie meines Freundes, wofür ich ihnen sehr danke. Insbesondere meine Mutter, Vater, Schwester und Großmutter, ohne die ich nie erreicht hätte, was ich persönlich und akademisch erlangt habe. Zu guter Letzt will ich das größte „Danke“ an die eine Person geben, die mich aufgehoben hat, wenn ich unten war und mich jeden Tag seit wir zusammen sind zum Lachen gebracht hat und die ich von ganzem Herzen liebe, Jonny Mackinnon.

Agradecimientos

Primero de todo me gustaría dar las gracias a todo mi grupo por el día a día y al Prof. Michael Groll por darme la oportunidad de llevar a cabo mi doctorado en su laboratorio. Me gustaría agradecer el apoyo y trabajo llevado a cabo conjuntamente con mis colaboradores Alemanes y sus grupos, Prof. Huber del MPI y Dr. Hillebrand de Bayer Crop Science, e internacionales Prof. Reboud-Ravaux de l'*université* Pierre et Marie Curie, France, Prof. Overkleeft de Leiden Universiteit, Holanda y Prof. Kisselev, de Dortmund University, USA. También me gustaría dar mi agradecimiento a Richard Feicht y Astrid König que no solo me han ayudado durante todo mi doctorado, pero también me han enseñado desde ciencia a alemán y por supuesto Bávoro, *Dankschea!* Estoy completamente en deuda con aquellas colegas de laboratorio que se han convertido en buenas amigas: Anja List, Veronika Flügel, Stephie Grubmüller, Nadine Gillmaier y Ingrid Span, por su apoyo, sus risas y los buenos tiempos que hemos pasado juntas durante estos últimos cuatro años. Por supuesto no podría olvidarme de, mis compañeros de doctorado, con los cuales he sembrado una muy buena amistad y siempre han estado ahí, en los ratos buenos y malos: Valentina Villa, Natalia Sarmientos, y Marcelino Arciniega. Debo, también, mi eterna gratitud a mis estudiantes Martina Müller, Susanne Mayer y Jochen Früh que han trabajado día a día a mi lado y que no solo han aprendido de mí, sino que yo también he aprendido mucho de ellos. Indudablemente, no habría sido posible hacer esta tesis sin el soporte moral de Liz Hogan y Susan Lauw y todos aquellos amigos que tengo lejos, mi familia y la familia de mi novio, a quien les doy las gracias de todo corazón. Sobre todo, a mi madre, mi padre, mi hermana y mi abuela, sin los cuales no habría llegado donde he llegado académicamente y personalmente. Por último, quiero darle mi mayor agradecimiento a la persona que ha estado siempre a mi lado, que me ha hecho reír cada día que hemos pasado juntos y a quien quiero con todo mi corazón, Jonny Mackinnon.

Declaration

I, Nerea Gallastegui, hereby declare that I independently prepared the present thesis, using only the references and resources stated. This work has not been submitted to any examination board yet. Parts of this work have been or will be published in scientific journals.

Hiermit erkläre ich, Nerea Gallastegui, dass ich die vorliegende Arbeit selbständig verfasst und keine anderen als die angegebenen Quellen und Hilfsmittel verwendet habe. Die Arbeit wurde noch keiner Prüfungskommission vorgelegt. Teile dieser Arbeit wurden bzw. werden in wissenschaftlichen Journalen veröffentlicht.

Nerea Gallastegui

München, 25.04.2012